88th ARFTG Microwave Measurement Conference

Power Amplifiers and Systems Design for Wireless Application

December 8th-9th 2016
Hilton Austin
Austin, Texas

IEEE Catalog Number: CFP16ARG-USB
ISBN: 978-1-5090-4513-6

88th ARFTG Conference Organizers

General Chair	**Jon Martens**
Technical Program Co-Chair	**Mitch Wallis**
Local Host	**Abhay Samant**

88th ARFTG Technical Program Committee

Peter Aaen, *University of Surrey*

Joe Gering, *Qorvo, Inc.*

Ron Ginley, *NIST*

Karel Hoffmann, *Czech Technical University*

Masahiro Horibe, *AIST*

Dan Kuester, *NIST*

Mauro Marchetti, *Maury Microwave*

Jon Martens, *Anritsu Corporation*

Basim Noori, *Apple*

Apolinar Reynoso-Hernandez, *CICESE*

Nick Ridler, *NPL*

Patrick Roblin, *The Ohio State University*

Andrej Rumianstev, *MPI Corporation*

Mohamed Sayed, *MMS*

Dominique Schreurs, *KU Leuven*

Damir Senic, *NIST*

Kubilay Sertel, *The Ohio State University*

Frans Verbeyst, *National Instruments*

Mitch Wallis, *NIST*

The 2016 ARFTG Executive Committee (ExCom)

President and Publicity	**Jon Martens,** Anritsu
Vice President and Nominations	**Dominique Schreurs**, KU Leuven
Secretary	**Joe Gering**, Qorvo, Inc.
Treasurer and Standards	**Ronald Ginley**, NIST
Electronic Communications	**Jean-Pierre Teyssier**, Keysight Technologies
Exhibits	**Joel Dunsmore**, Keysight Technologies
Workshops	**Patrick Roblin**, The Ohio State University
Publications	**David Blackham**, Keysight Technologies
Sponsorship	**Mohamed Sayed**, MMS
Education and Short Course	**John Wood,** Obsidian Microwave LLC
Membership	**Rusty Myers**, Keysight Technologies
Publicity	**Andrej Rumiantsev**, MPI Corporation
Publicity	**Gayle Collins**, Intel
Electronic Publicity	**Peter Aaen**, University of Surrey
MTT-S Liaison and Awards	**Leonard Hayden**, Qorvo Inc.

Ex-Officio

Executive Secretary	**John Cable**

Session A: Design and Measurement for Wireless Applications

Chair: Jon Martens, Anritsu

Bringing Envelope Tracking to the Market: A Product and Metrology Development Perspective (Invited)

P. Draxler, H. Masaracioglu, Qualcomm, San Diego, United States

Measurement of Dynamic Power Dissipation and Estimation of Effective Dynamic Efficiencies in an LTE Chireix PA

J. A. Galaviz-Aguilar[1,2], H. Chang[1], F. J. Martinez-Rodriguez[3,1], P. Roblin[1], J. C. Nunez Perez[2], [1]The Ohio State University, Columbus, United States, [2]Instituto Politecnico Nacional, IPN-CITEDI, Tijuana, Mexico, [3]National University of Mexico, Ciudad de México, United States

Radiated Power Based on Wave Parameters at Millimeter-wave Frequencies for Integrated Wireless Devices

D. Senic[1], K. A. Remley[1], D. F. Williams[1], D. C. Ribeiro[2], C. Wang[1], C. L. Holloway[1], [1]National Institute of Standards and Technology, Boulder, United States, [2]University of Aveiro, Aveiro, Portugal

Session B: On-wafer Measurements

Chair: Jeff Jargon, NIST

Development of a Reference Wafer for On-Wafer Testing of Extreme Impedance Devices

H. Votsi[1,3], I. Roch-Jeune[2], K. Haddadi[2], C. Li[3], G. Dambrine[2], P. Aaen[1], N. Ridler[3], [1]University of Surrey, Guildford, United Kingdom, [2]University of Lille, Lille, France, [3]National Physical Laboratory, Teddington, United Kingdom

The Impact of ENR and Coaxial Calibration in Accurate On-Wafer Noise Parameter Testing for Ultra-Low Noise Devices

K. C. Kellogg[1], L. Dunleavy[1], S. Skidmore[1], G. Simpson[2], [1]Modelithics, Inc., Tampa, United States, [2]Maury Microwave Corporation, Ontario, United States

Fused Silica based RSOL calibration substrate for improved probe-level calibration accuracy

L. Galatro, M. Spirito, Delft University of Technology, Delft, Netherlands

Session C: Frontiers of Microwave Measurements

Chair: Mohamed Sayed, Microwave & Millimeter Wave Solutions

Multiphysics Characterization – More Than Just Microwaves (Invited)

P. Aaen, U. of Surrey, Surrey, United Kingdom

Kicking the Tires of the NIST Microwave Uncertainty Framework Part 1

R. A. Ginley, National Institute of Standards and Technology, Boulder, United States

Session D: mm-Wave and Terahertz Measurements

Chair: Dave Blackham, Keysight Technologies

Power Level Control of mm-Wave Test Benches for Accurate Small and Large-signal DUT Measurements

C. De Martino, Z. Hu, L. Galatro, G. Sarris, M. Spirito, Delft University of Technology, Delft, Netherlands

Spectral Characterization of Linear Isotropic and Anisotropic Dielectric Materials Using Terahertz Measurement Systems

J. M. Seligman[1,1], C. C. Green[2,2], B. K. Sternberg[1,1], C. K. Walker[1,1], [1]University of Arizona, Tuscon, United States, [2]Rogers Corporation, Chandler, United States

Performance Evaluations of Dielectric Waveguide for Millimeter-wave On-Wafer Measurements

M. Horibe, R. Sakamaki, Y. Kato, National Institute of Advanced Industrial Science and Technology, Tsukuba, Japan

Interactive Forum

Chair: Ron Ginley, NIST

Lumped modeling of integrated MIM capacitors for RF applications

F. Korndörfer[1], V. Mühlhaus[2], [1]IHP GmbH, Frankfurt (Oder), Germany, [2]Dr. Mühlhaus Consulting & Software GmbH, Witten, Germany

Design of WR-6 (110GHz ~ 170GHz) Waveguide Microcalorimeter

W. Yuan, C. Ma, X. Cui, Y. Li, National Institute of Metrology, Beijing, China

CAD-Assisted Microwave Characterization of Ink-Jet Printed CPW on PET Substrates

A. Sahu[1], V. Devabhaktuni[1], A. Lewandowski[2], T. M. Wallis[3], P. H. Aaen[4], [1]University of Toledo, Toledo, United States, [2]Warsaw University of Technology, Warsaw, Poland, [3]National Institute of Standards and Technology, Boulder, United States, [4]Unversity of Surrey, Surrey, United Kingdom

Digitally Assisted Analog Predistortion Technique for Power Amplifier

K. Gumber, P. Jaraut, M. Rawat, Indian Institute of Technology Roorkee, Roorkee, India

Wideband Impedance-varying N-way Wilkinson Power Divider/Combiner for RF Power Amplifiers

O. I. Hussein[1], K. A. Al shamaileh[2], V. K. Devabhaktuni[1], P. H. Aaen[3], [1]University of Toledo, Toledo, United States, [2]Purdue University Northwest, Hammond, United States, [3]University of Surrey, Guildford, United Kingdom

Session E: Power Amplifiers

Chair: Peter Aaen, U. of Surrey

Supply modulation for power amplifier efficiency enhancement (Invited)

Z. Popovic, U. of Colorado, Boulder, Boulder, United States

Cross-correlation measurement method of Error Vector Magnitude and application to power amplifier non-linearity performances

J. Sombrin[1,2], [1]TESA Laboratory, Toulouse, France, [2]Labex Sigma-Lim, Limoges, France

Session F: Transmission Lines and Nonlinear Measurements

Chair: Mitch Wallis, NIST

A Simple Method for Transmission Lines Quality Control

A. A. Savin[1,2], V. G. Guba[2], O. N. Bykova[2], A. Rumiantsev[3], [1]Tomsk State University of Control Systems and Radioelectronics, Tomsk, Russian Federation, [2]NPK Tair, Tomsk, Russian Federation, [3]MPI Corporation, Chu-Pei, Taiwan

Uncertainty of Parameter Estimation in Equivalent Circuit Model of Gallium Nitride Diode for Rectifier Design at 5.8 GHz

R. Kishikawa[1,2], M. Horibe[1], S. Kawasaki[3,2], [1]National Institute of Advanced Industrial Science and Technology, Tsukuba, Japan, [2]The Graduate University for Advanced Studies, Sagamihara, Japan, [3]Japan Aerospace Exploration Agency, Sagamihara, Japan

Linearity characterization of RF circuits through an Unequally Spaced Multi Tone signal

S. Laurent[1], T. Jean Pierre[2], R. Quéré[1], J. Sombrin[3], M. Prigent[1], [1]XLIM, Brive La Gaillarde, France, [2]Keysight, Santa Rosa, United States, [3]XLIM, Limoges, France

Measurement of Dynamic Power Dissipation and Estimation of Effective Dynamic Efficiencies in an LTE Chireix PA

José Alejandro Galaviz-Aguilar*†, Hsiu-Chen Chang*, Francisco Martinez-Rodriguez*‡, Patrick Roblin*
José Cruz Núñez-Pérez†
*Department of Electrical and Computer Engineering, The Ohio State University, (OSU), Columbus, Ohio 43210, USA
†Instituto Politécnico Nacional, (IPN-CITEDI), Tijuana, B.C. 22435, México
‡Facultad de Ingeniería, Universidad Nacional Autónoma de México, (UNAM), Ciudad de México 04510, México

***Abstract*—A testbed is reported for the measurement of the instantaneous power dissipation of a dual input Chireix power amplifier (PA) driven by an LTE signal. An FPGA system is used to dynamically control the phase difference and respective incident power level of the two signals injected at the dual-inputs of the Chireix PA under test. The dynamic drain currents of the power amplifier are measured using two Hall effect current probes placed inside and outside the PA biasing network. The synchronized acquisition of the biasing current, biasing voltage, and RF output power of the PA is then performed for 1 MHz and 10 MHz bandwidth LTE signals. As expected, the power spectra of the biasing currents exhibit twice the bandwidth of the LTE signals. After some signal processing and calibration, an estimation of the dynamic efficiency is obtained from the measured dynamic biasing current and RF output power. It is further verified that the insights obtained from the modeling of the dynamic power dissipation and its memory effects can assist with the optimization of the Chireix phase control required to maximize the average power efficiency of the Chireix PA.**

***Index Terms*—Chireix Power Amplifier, GaN HEMTs, Long Term Evolution Advanced (LTE-A), PA Efficiency, Outphasing.**

I. Introduction

Modern communication transmitter systems require power-efficient and linear RF amplifiers to handle the wideband or multiband signals resulting from carrier aggregation, such as in long term evolution advanced (LTE-A) standards [1]. Such communication signals are known to exhibit high peak to average power ratio (PAPR) and special PA architectures such as the Doherty [2], [3] and envelope tracking PAs [4] are used in basestations in order to achieve a high power-efficiency at both peak and backoff power levels while maintaining a reasonably linearity. Digital predistortion (DPD) can then be used to achieve a highly linear operation.

Recently, linear amplification using nonlinear components (LINC) has also been the object of renewed interests [5]. The Chireix amplifier implementation relies on the concept of outphasing to control the output power to obtain a high efficiency between the peak and backoff power levels. In this study a Chireix PA realized with two GaN HEMTs is considered. Under CW operation, one can determine the optimal outphasing phase and input power of the signals exicting a dual-input Chireix PA resulting in an optimal efficency operation at each output power level. However such amplifiers are intended to be used with modulated signals for which the PA mostly operates at lower average power with infrequent operation at peak power. Under such conditions, self-heating and trapping in the GaN HEMTs will be reduced and the optimal phase and input power control may benefit from being modified. Any insight we may gain on the instantaneous power dissipation under time-varying output power signals can then facilitate the optimization of the PA controls.

With such motivations in mind, we present in this paper a testbed for simultaneously measuring the instantaneous power dissipation and the output RF power of a dual input Chireix PA when driven by an LTE signal. For this purpose a FPGA testbed was developed for the synchronized acquisition of the biasing current, biasing voltage and RF output power of the Chireix PA. This testbed is presented in Section II and the measurement results reported in Section III. The results obtained are summarized in Section IV and further applications and investigations are proposed.

II. Experimental Testbed for Chireix Measurements

The testbed used for the measurements is shown in the Fig. 1. The digital environment consists of an ARRIA V FPGA RF board with a dual-channel transmitter and a receiver which shares the same clock. The RF transmitter modulator board from Texas Instruments includes dual 16-bit DACs operating with a synchronization clock set at 307 MHz. In addition, these two DACs use an interpolation factor-by-4 to allow for the use of a digital IF, such that the residual LO leakage of the I/Q modulators can be more readily filtered as needed. The receiver board is based on a TSW1266 I/Q demodulator operated at a sampling rate of 614 MHz. The LTE-advanced digitized signals are directly stored in the FPGA internal memories enabling the system to play and record time-synchronized data directly under Matlab control with the execution of Quartus tcl scripts.

The baseband drain current measurements of the Chireix PA system is performed using an oscilloscope (DPO7104 Tektronix). Two current probes (TCP0030) are used to measure the current waveforms at two different location in the PA drain biasing network. A third channel is used to acquire the envelope waveform of the PA output using a diode detector (HP423B) for the purpose of synchronizing the scope and FPGA measurements. The oscilloscope is controlled through a GPIB-USB-HS interface, and the biasing currents and envelope waveforms data are acquired using a Matlab script. Once the setup system is initialized, the measurements of the current

978-1-5090-4514-3/16/$31.00 ©2016 IEEE

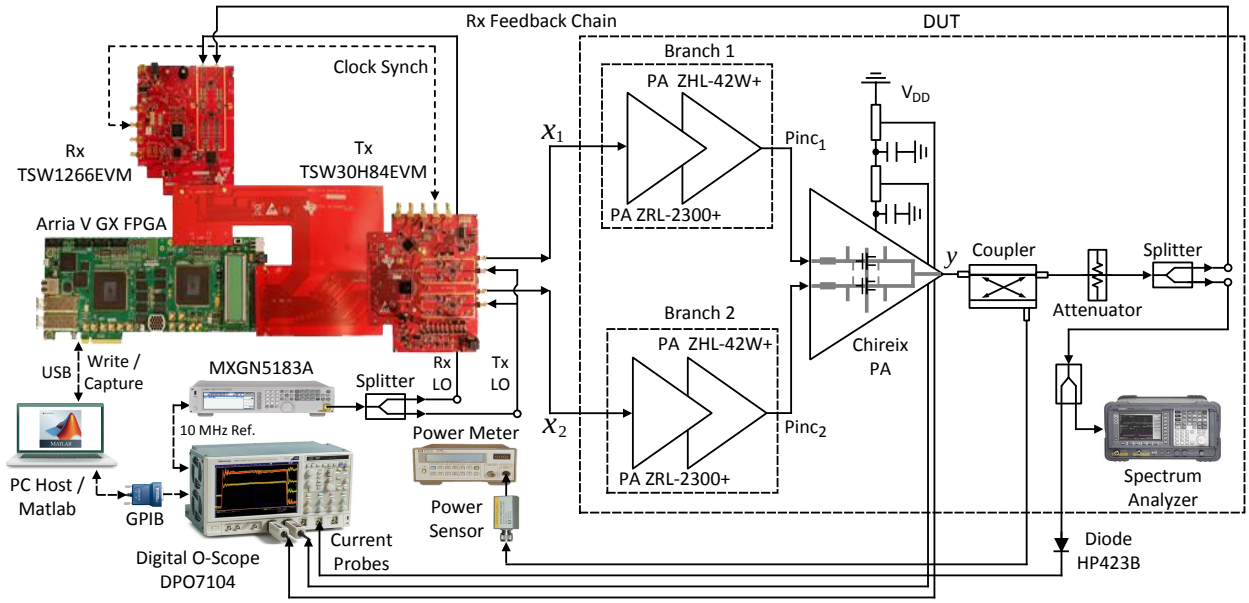

Fig. 1: Overall testbed diagram for measurements.

waveforms and the FPGA data (AM/AM and AM/PM) can be performed at the same time.

The Chireix PA output is connected to a HP 437B power meter via a 24 dB coupler for measuring the PA output power, while the signal collected at the through-port of the coupler, is sent to a power attenuator. The attenuated signal is collected and sent to the receiver board where it is digitized and stored in the FPGA internal memory.

A. Phase and Power Calibration Procedure

In order to amplify an LTE signal represented by $x(n) = I(n)+jQ(n) = |x(n)|\exp\left[j\phi_x(n)\right]$ the dual-input Chireix PA needs to be controlled by two modulated RF signals which can be represented by the following complex outputs $x_1(t)$ and $x_2(t)$:

$$x_1(n) = I_1(n) + jQ_1(n) = |x_1(n)| \cdot e^{j\phi_1(n)} \tag{1}$$

$$x_2(n) = I_2(n) + jQ_2(n) = |x_2(n)| \cdot e^{j\phi_2(n)} \tag{2}$$

with respective phases:

$$\phi_1(n) = \phi_x(n) - \frac{1}{2}\phi_{diff}\left[P_{out}(n)\right] \tag{3}$$

$$\phi_2(n) = \phi_x(n) + \frac{1}{2}\phi_{diff}\left[P_{out}(n)\right], \tag{4}$$

and respective amplitudes:

$$|x_1(n)| = \sqrt{P_{inc,1}\left[P_{out}(n)\right]} \tag{5}$$

$$|x_2(n)| = \sqrt{P_{inc,2}\left[P_{out}(n)\right]}. \tag{6}$$

In the above formula, $\phi_{diff}\left[P_{out}\right]$ is the input-referred out-phasing phase difference $\phi_2 - \phi_1$ and $P_{inc,1}\left[P_{out}\right]$ and $P_{inc,2}\left[P_{out}\right]$ are the incident powers applied at the PA inputs 1 and 2. Their functional dependences on the targeted output power P_{out} have been predetermined during the design and subsequent CW testing of the Chireix PA under test.

Thus for the Chireix PA to work as designed and yield the targeted output power and efficiency, the proper signals x_1 and x_2 must be applied at its inputs in terms of phase and amplitude. It was found that for the tested PA, the power efficiency degraded significantly even for a one degree error in phase.

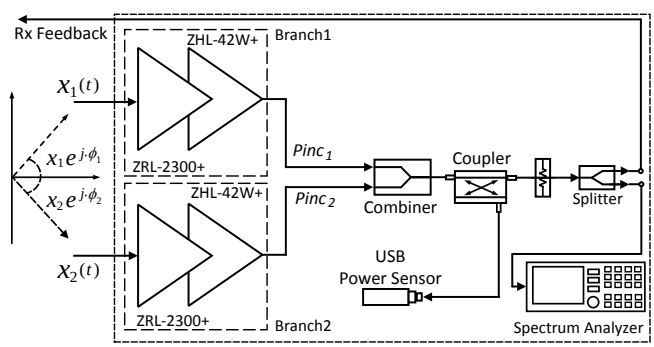

Fig. 2: Conceptual diagram for the phase and power calibration.

In the testbed used, the modulated signals x_1 and x_2 emerging from the FPGA are first frequency shifted by the same digital IF of 76.8 MHz in the ADC, before being upconverted to 2 GHz by the IQ modulators using an LO frequency of 1.9232 GHz. The LO is provided by an Analog Signal Generator (MXGN5183A). The signals x_1 and x_2 emerging from the I/Q modulators are then applied to the dual-input Chireix PA via two similar driver branches. Each driver branch features two high gain PAs (Driver ZRL-2300+, Driver PA ZHL-42W+) beside the two I/Q modulators pre-amps.

Despite the similarity of the two branches, differences in

cable lengths, group phases and gains in the driver PAs result in signals at the output of the driver branches which are strongly mismatched in terms of phase and power. A power and phase calibration is thus required to properly drive the Chireix PA.

Fig. 2 shows a conceptual diagram of the measurement setup used for the phase calibration which is realized by sweeping the phase offset while using a passive power combiner instead of the Chireix PA. To perform the phase calibration, two identical LTE-advanced signals of 10 MHz bandwidth each are applied to the input of the pre-characterized power combiner. This configuration enables us to obtain the required phase difference at the inputs which yields a phase match at the output.

An RF USB power sensor is used for measuring and recording the average power and peak power under a Matlab script control. The optimal phase ϕ_{max} is the phase which yields a peak output power when the two signals add constructively. The anti-phase ϕ_{min} is the phase which yields a minimum output power when the two signals add destructively. These two phases verify $\phi_{max} - \phi_{min} = 180°$. After the phase calibration, the error correction is simply performed using:

$$x_{2,cal} = x_2 e^{(j\phi_{max})} \quad \text{and} \quad x_{1,cal} = x_1 \tag{7}$$

For driving the Chireix PA a power calibration is also required for the driver branches so that the correct incident power levels are applied at both inputs. Note that the two driver branches are operating in their linear range. They provide each about 50 dB gain. For this purpose, a simple scaling factor is applied to x_1 and x_2 in Matlab after calibration. A power level of 20 dBm is approximately targeted for $P_{inc,1}$ and $P_{inc,2}$ to operate the Chireix PA device being tested.

III. Measurement Results

The power spectra obtained for the DC current probes and RF output power for a 1 MHz LTE signal are shown in Fig. 3. As expected, the power spectra of the biasing currents I_{DC} exhibit twice the bandwidth of the LTE signal x since we have:

$$\eta(P_{out}) = \frac{P_{out}}{I_{DC}(P_{out})V_{DD}} \tag{8}$$

with V_{DD} the power supply and $P_{out} = P_{out,max}|x|^2$. Similar results are obtained for the 10 MHz LTE signal in Fig. 4. The current probe placed in the middle of the biasing network measures a current with the widest bandwidth as expected. The voltage fluctuation of the 24 V supply voltage at that point remains itself below 2 mV. A linear filter model is extracted under dynamic operation to characterize the filtering effect of the bias network. The model yields an normalized mean square error (NMSE) of -38.4 dB and -26.5 dB respectively for the current probes 1 and 2. The PAPR measured in the signals LTE 1 MHz and LTE 10 MHz using a preliminary linearization is around of 7.5 dB and 9.6 dB respectively. A nonlinear filter should allow for an improved current modeling accuracy for the 10 MHz LTE case.

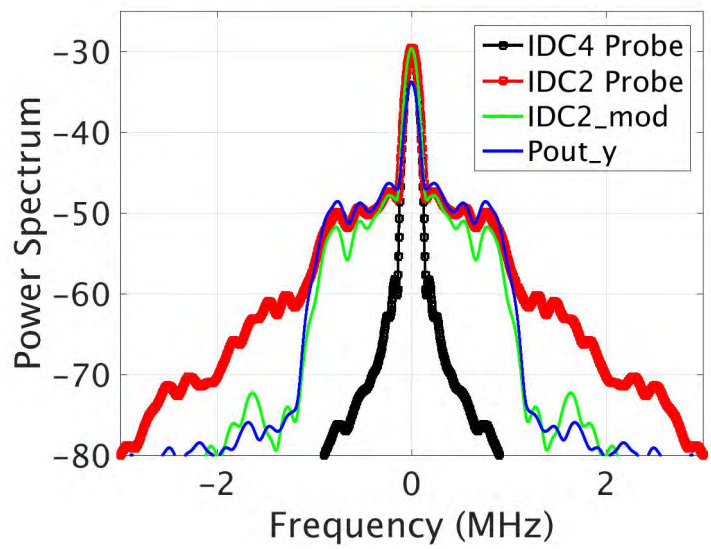

Fig. 3: Power spectra of a) DC current probe 1, b) DC current probe 2, c) filtered DC current probe 2, and d) ouput RF power for a 1 MHz LTE signal.

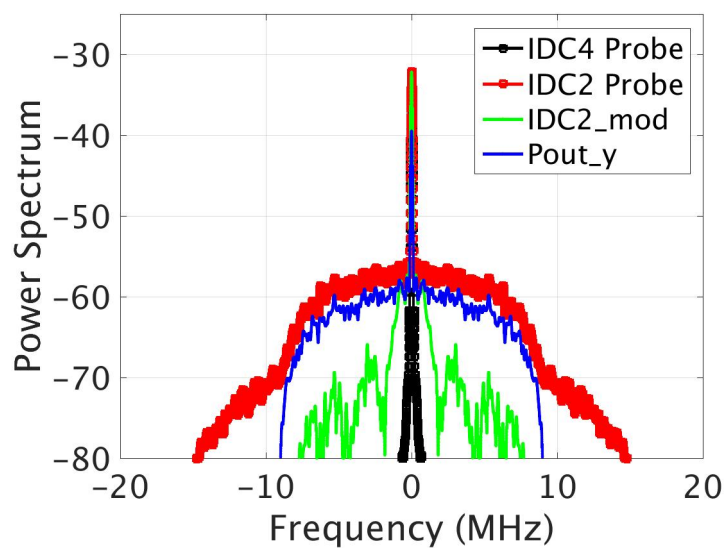

Fig. 4: Power spectra of a) DC current probe 1, b) DC current probe 2, c) filtered DC current probe 2, and d) ouput RF power for 10 MHz LTE signal.

The effective instantaneous efficiency predicted from the dynamic current measurement with the help of the filter is shown in Fig. 5 (blue dots) for the 1 MHz LTE signal and is shown in Fig. 6 (blue dots) for the 10 MHz LTE signal. Keeping the same filter calibration, the effective instantaneous efficiency is observed in Fig. 5 to be reduced once an outphasing error of 1 degree is introduced in the phase calibration. The average efficiency is correspondingly reduced by about 15 percent (green dots). This demonstrates

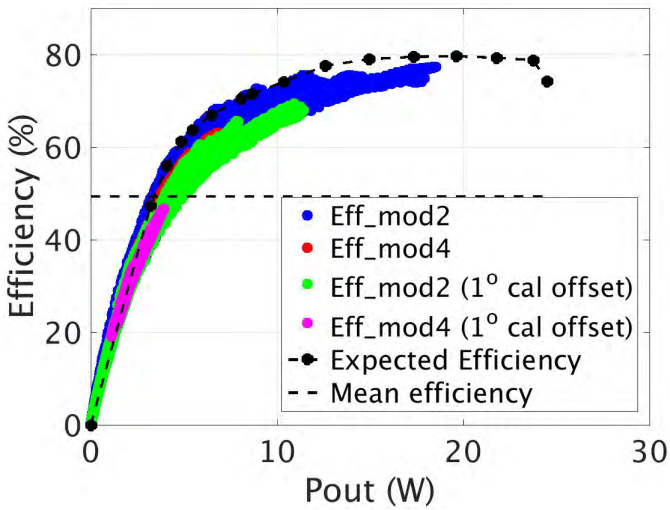

Fig. 5: Instantaneous efficiency versus instantaneous output power for a 1 MHz LTE signal (blue dots), and degradation of the efficiency with 1° outphasing error (green dots).

the capability of the modeling to estimate the variation of the effective instantaneous efficiency to assist the user with the optimization of the average power efficiency.

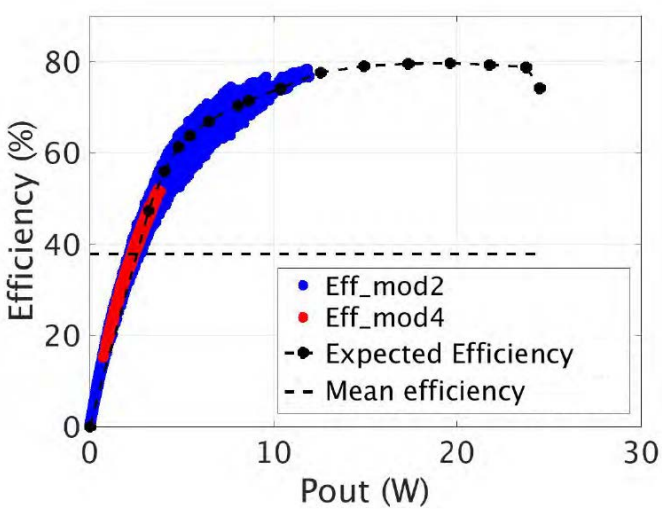

Fig. 6: Instantaneous efficiency versus instantaneous output power for a 10 MHz LTE signal.

IV. Conclusion

The modeling of the supply terminal impedance of PAs has been investigated in the case of envelope tracking PAs [6] to assist with their control. Similarly in this paper, a testbed is reported for the measurement of the dynamic power dissipation of Chireix PAs driven by an LTE signal to assist with their control. More details on the Chireix PA which was designed using an embedding device model [7] will be subsequently reported. A preliminary linear model was developed for the DC current measured in the biasing network.

The measurement of the dynamic biasing current and the estimation of the effective instantaneous efficiency provides useful feedback on the Chireix PA operation which can be used to optimize its controls $\phi_{diff}\left[P_{out}\right]$, $P_{inc,1}\left[P_{out}\right]$ and $P_{inc,2}\left[P_{out}\right]$ for the purpose of increasing its average power efficiency under dynamic operation.

Acknowledgments

The first author would like thank to the Mexican government entity (CONACyT) for the scholarship granted. The author would also like thank to the Non-Linear RF research lab at the Ohio State University.

References

[1] S. A. Bassam, W. Chen, M. Helaoui and F. M. Ghannouchi, "Transmitter Architecture for CA: Carrier Aggregation in LTE-Advanced Systems," *in IEEE Microwave Magazine* vol. 14, no. 5, pp. 78-86, July-Aug. 2013.

[2] S. C. Cripps, "RF Power Amplifier for Wireless Communication," *2nd edition, Artech House Publishers.*, 2006

[3] H. Jang, P. Roblin, C. Quindroit, Y. Lin and R. D. Pond, "Asymmetric Doherty Power Amplifier Designed Using Model-Based Nonlinear Embedding," *in IEEE Transactions on Microwave Theory and Techniques.*, vol. 62, no. 12, pp. 3436-3451, Dec. 2014.

[4] Z. Popovic, "GaN power amplifiers with supply modulation," *2015 IEEE MTT-S International Microwave Symposium.*, Phoenix, AZ, 2015, pp. 1-4.

[5] T. W. Barton, A. S. Jurkov, P. H. Pednekar and D. J. Perreault, "Multi-Way Lossless Outphasing System Based on an All-Transmission-Line Combiner," *in IEEE Transactions on Microwave Theory and Techniques.*, vol. 64, no. 4, pp. 1313-1326, April 2016.

[6] G. P. Gibiino, J. Couvidat, G. Avolio, D. Schreurs and A. Santarelli, "Supply-terminal 40 MHz BW characterization of impedance-like non-linear functions for envelope tracking PAs," *2016 87th ARFTG Microwave Measurement Conference (ARFTG).*, San Francisco, CA, 2016, pp. 1-4.

[7] H. Jang, P. Roblin and C. Quindroit, "Adjustable load-modulation asymmetric Doherty amplifier design using nonlinear embedding," *2014 IEEE MTT-S International Microwave Symposium (IMS2014).*, Tampa, FL, 2014, pp. 1-4.

Radiated Power Based on Wave Parameters at Millimeter-wave Frequencies for Integrated Wireless Devices

Damir Senic[1], Kate A. Remley[1], Dylan F. Williams[1], Diogo C. Ribeiro[2], Chih-Ming Wang[1], Christopher L. Holloway[1]

[1]National Institute of Standards and Technology, Boulder, Colorado, USA,
[2]University of Aveiro, Aveiro, Portugal

***Abstract* — We provide total radiated power measurements at millimeter-wave frequencies using a reverberation chamber and a power-calibrated vector network analyzer capable of measuring wave parameters. We compare total radiated power results obtained from two different approaches. In the first approach, applicable when the terminals of the antenna under test are accessible, the total radiated power is calculated directly from forward and reflected waves. In the second approach, when we cannot access the terminals of the antenna under test, the total radiated power is calculated from measured forward and reflected waves at the receive antenna taking into account chamber loss. The results from the two different approaches have excellent agreement, and are within the measurement uncertainty. The uncertainty in our total radiated power measurements is below 2%.**

***Index Terms* — Antenna measurement, communication systems, internet of things, millimeter-wave wireless, reverberation chamber, radiated power measurement, wave parameters, wireless systems.**

I. Introduction

Modern communications systems rely on the modulation of radio-frequency (RF) signals to exchange information. Different equipment can be used to analyze RF signals, including power meters, spectrum analyzers, oscilloscopes, vector signal analyzers, and vector network analyzers (VNAs). Here, we will focus on use of a VNA for analyzing RF signals in terms of total radiated power (TRP).

Power-calibrated VNAs have been traditionally used for conducted power measurements. While this was feasible for devices with accessible output terminals, modern communication devices have integrated antennas and direct measurement at the antenna terminals is not possible. Consequently, the only available solution is a transition from on-wafer to over-the-air (OTA) measurements. Reverberation-chamber-based test methods are efficient, and standardized approaches are recently available for OTA test [1].

Traditionally, reverberation chambers (RCs) were used for various measurements in electromagnetic compatibility (EMC) [2] and, more recently, wireless communications [1]. An RC is an electrically-large resonator with a high-Q value [3], [4]. Due to that fact, the instantaneous spatial distribution of the electromagnetic fields inside such an environment is not uniform. In order to estimate a quantity of interest from measurements in a reverberation chamber, we need to average over measured randomized field samples. Field randomization, or "mode-stirring" techniques include mechanical paddle stirring, where electrically-large paddle(s) move and change the boundary conditions inside a chamber, and position stirring, where the device under test (DUT) antenna is moved.

In this paper, we study total radiated power based on wave-parameter measurements at millimeter-wave frequencies inside an RC. In the past, radiated-emission tests from different RF sources were performed in anechoic chambers or open area test sites, where the limits referred to the maximum electric field strength at certain distance, defined by *e.g.*, [5]. On the other hand, emissions tests performed inside an RC provide us with compliance in terms of TRP. The advantages of using RCs compared to anechoic chambers or open area test sites are mainly in their low cost, simplicity, and shorter measurement times. Much of the prior work on total power radiated by intentional and unintentional sources can be found in [6]-[11].

Wave parameters have the advantage that a power-calibrated VNA can report the forward and reverse waves' power levels directly. By adding a phase reference [12], we can obtain both magnitude and phase information of each frequency component. Even though this paper focuses on TRP from a CW signal, we plan to use the same setup for periodic modulated signals, where a phase reference is of the utmost importance.

Since millimeter-wave frequencies will most likely be used in the next-generation wireless networks [13], we decided to do our research at this frequency range.

II. Radiated Power

According to [2], the amount of RF power radiated (P_{rad}) by a device under test can be determined by measuring the amount of power received by the receive antenna (P_{rec}). Taking into account chamber loss (G_{ref}), P_{rad} can be expressed as:

$$P_{\mathrm{rad}} = \frac{P_{\mathrm{rec}}}{G_{\mathrm{ref}}} . \tag{1}$$

To determine G_{ref} from measurements, we must remove the effects of efficiency and mismatch at the antennas ports. In this case, G_{ref} can be expressed as:

$$G_{\mathrm{ref}} = \frac{\left\langle \left|S_{21}\right|^2 \right\rangle}{\eta_{\mathrm{TX}}\eta_{\mathrm{RX}}\left(1-\left|\langle S_{11}\rangle\right|^2\right)\left(1-\left|\langle S_{22}\rangle\right|^2\right)} , \tag{2}$$

978-1-5090-4514-3/16/$31.00 ©2016 IEEE

where the brackets denote the ensemble average over the mode-stirring sequence, S_{21} is the forward transmission scattering parameter, and the terms in the denominator represent the free-space radiation efficiency (η_{TX} and η_{RX}) and mismatch for the two antennas. These may be measured in either an anechoic chamber or in an unloaded chamber, such as we have here.

The power at the receive antenna is traditionally measured by a spectrum analyzer, power meter, or base station emulator. In this paper, we will show that power at the receive antenna can be more easily measured by a power-calibrated VNA because all mismatch corrections are performed automatically even while the chamber characteristics are changing. The power will be defined in terms of wave parameters a and b, where a is proportional to the voltage of the incident wave and b is proportional to the voltage of the reflected wave at the measurement reference plane, normalized to the square of the system characteristic impedance [14]. In this study, we can access the DUT's antenna terminals. Thus, we can measure the radiated power at the transmit antenna directly in terms of incident (a_1) and reflected (b_1) waves as:

$$P_{\text{rad,direct}} = \left\langle |a_1|^2 - |b_1|^2 \right\rangle \eta_{TX} \,. \tag{3}$$

On the other hand, to simulate a DUT whose antenna terminals cannot be accessed, we can also assess total radiated power from (1) by measuring chamber loss (2) and the power at the receive antenna:

$$P_{\text{rad,integrated}} = \frac{P_{\text{rec}}}{G_{\text{ref}}} = \frac{\left\langle |b_2|^2 - |a_2|^2 \right\rangle}{G_{\text{ref}}} \,, \tag{4}$$

where a_2 and b_2 are wave parameters measured by the VNA at the receive antenna port.

We next describe the measurement setup that we used. In Section IV, we will give the results from (3) and (4) and compare them in order to verify the VNA's applicability for power measurements of wireless devices with integrated antennas.

III. Measurement Setup and Procedures

We performed total radiated power measurements over a frequency range from 43 GHz to 47 GHz using an RC with a power- and phase-calibrated 50 GHz VNA, as shown in Fig. 1. Power was calibrated by a wideband, diode-based power sensor connected to the power meter. Phase calibration was achieved by use of two comb generators, one connected to port 2 of the VNA during the measurements and the other connected to the transmit calibration plane during the calibration of the VNA. Even though a phase calibration is not necessary for total radiated power measurements, we plan to use this setup as a base for more complex, modulated signals measurements where precise phase information of each frequency component is required.

The chamber was equipped with two mechanical stirrers. The larger one rotated about a horizontal (H) axis within a cylindrical volume of 0.6 m height and 0.2 m diameter, while the smaller one rotated about a vertical (V) axis within a cylindrical volume of 0.5 m height and 0.2 m diameter. The RC's size was 1 m (l) × 0.65 m (w) × 0.55 m (h), which corresponds to an electrical size of approximately 150 λ × 100 λ × 80 λ at the center frequency of 45 GHz.

We used three different transmit antennas that have different radiation patterns (from highly directional to omnidirectional in half-space) to simulate a wide range of real integrated antennas. Measured antennas included a waveguide horn antenna, an open-ended waveguide (OEW), and a microstrip patch antenna. The transmit and receive antennas were oriented away from each other in order to lower the unstirred energy (K factor) between them [15]. The RC's bulkhead was equipped with two feedthroughs, one waveguide that was connected to the VNA's port 3 and the other a 2.4 mm coaxial connected to the VNA's port 1. The waveguide horn receive antenna at port 3 was oriented toward the vertical stirrer (see Fig. 1). The signal from the 2.4 mm feedthrough was brought to the transmit antenna via a coaxial cable for the microstrip patch antenna and a coaxial-to-waveguide transition for OEW and waveguide horn antenna.

The transmit antennas were oriented toward the horizontal stirrer and positioned in the middle of the RC's working volume (see Figs. 1 and 2). Key measurement parameters are summarized in Table I.

Wave parameters were measured for 2500 paddle orientations (50 vertical and 50 horizontal). Calibration standards and DUT measurements were collected as raw data, and calibration was performed afterwards within the NIST Microwave Uncertainty Framework [16], [17].

TABLE I: Measurement Parameters

Parameter		Value
Frequency range		43 GHz – 47 GHz
Number of frequency points		1601
IF bandwidth	Calibration	100 Hz
	Measurements	2 kHz
VNA output power level		-10 dBm
VNA dwell time		10 µs
Paddle step size ($V \times H$)		7.2° × 7.2°
Number of paddle orientations ($V \times H$)		50 × 50

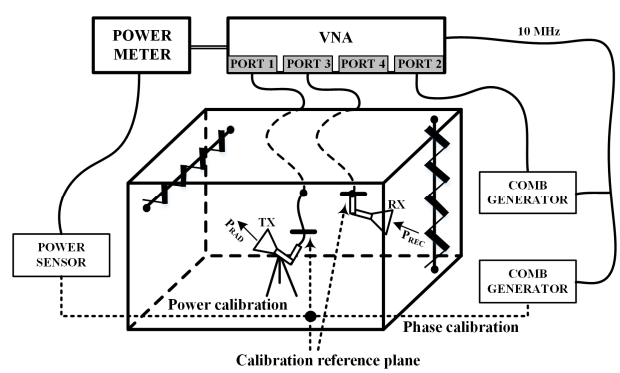

Fig. 1. Schematic layout of measurement setup for total radiated power measurements based on a power- and phase-calibrated VNA.

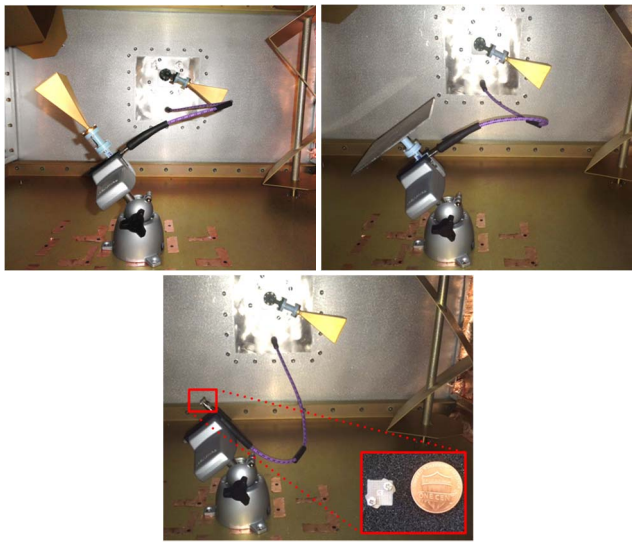

Fig. 2. Three different transmit antennas used for total radiated power measurements; a waveguide horn antenna (top left), an open-ended waveguide (top right), and a microstrip patch antenna (bottom) (compared to a U.S. penny for size).

IV. Results

In this section, we compare total radiated power results measured directly from the wave parameters using (3) to those obtained from scattering-parameters measurements of G_{ref} using (4). We measured G_{ref} with the same pair of antennas we used for our DUT measurements which could artificially lower the uncertainty. Even though these would typically be different pairs of antennas, our focus is on the difference in the approaches from (3) and (4). Note that to calculate the total radiated power by applying (3), we need to have access to the transmit antenna terminals. Common DUTs generally do not have accessible antenna terminals. In that case, we need to use (4). Taking (3) as true value for total radiated power, we will show how good our estimate of total radiated power (4) is based on the received power and chamber loss measurements.

In order to simulate different DUTs, the VNA was connected to various transmit antennas, each with its own radiation pattern and efficiency. The VNA was set to -10 dBm output power. In Fig. 3, we present TRP results for the three different transmit antennas obtained from (3) as solid lines and (4) as dotted lines. The differences in calculated TRP from (3) and (4), given as Δ_{Prad}, are shown in Fig. 4 with error bars as uncertainty values. The mean (over a 4 GHz bandwidth) differences between the two different approaches for the waveguide horn antenna, OEW, and microstrip patch antenna were 0.053 dB, 0.051 dB, and 0.055 dB. Excellent agreement is seen, with differences at or within our measurement uncertainty given in Section V.

Our research indicates that the waveguide horn antenna had the highest average (over 4 GHz bandwidth) TRP of -16.24 dBm. This is due to its high efficiency (low losses and good impedance match). At the same time OEW radiated -16.55 dBm on average, and microstrip patch antenna -17.48 dBm. Note also that the patch TRP drops very fast above 45 GHz. The reason for the drop is poor matching above that frequency. A similar effect was observed in the antenna efficiency study given in [18].

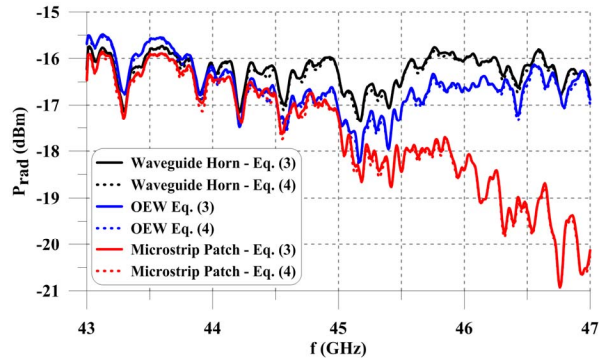

Fig. 3. Total radiated power results calculated from (3) and (4) for three different transmit antennas.

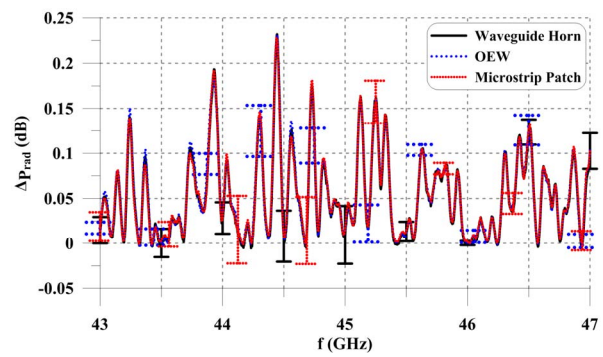

Fig. 4. Differences in TRP results obtained from two different approaches and their associated uncertainties.

V. Measurement Uncertainty

In this section, we provide measurement uncertainty results from the NIST Microwave Uncertainty Framework [16],[17] calculated using both sensitivity and Monte Carlo approaches. The Framework is a NIST-developed software package that allows assignment of uncertainties and probability distributions to error mechanisms in the calibration, and propagates the associated uncertainties to the end result. From repeat measurements, it can also determine random components of measurement uncertainty.

The Framework represents the resulting errors as perturbed measurement vectors that are propagated from one calculation step to the next. This enables uncertainties to be correctly correlated throughout the calculations even when the same uncertainty mechanism is present at different steps of the calculation. The Framework captures and propagates the uncertainties of wave-parameter measurements and finds the correlation between them. By identifying the error mechanisms in the calibration standards, we can determine the correlations between the wave parameters across frequencies, which can then be propagated into the measurement uncertainties.

In [15], [18], we showed that the uncertainty due to the lack of spatial uniformity is not significant for our unloaded chamber. Therefore, we will study only the uncertainty due to the finite number of mode-stirring measurement samples. Regarding future measurements of modulated signals, for which we need to load the chamber to broaden the coherence bandwidth, the uncertainty due to the lack of spatial uniformity should be taken into account.

The uncertainty in the differences between two approaches for the three different simulated DUTs is given in Fig. 4. While the uncertainties for the waveguide horn antenna and the OEW are similar, the higher uncertainty values can be seen for the microstrip patch antenna. The reason for that is caused by the added uncertainty from the de-embedding of a coaxial-to-waveguide adapter. Note that the calibration was performed at the waveguide plane. Maximum uncertainty values from the NIST Microwave Uncertainty Framework for the waveguide horn, OEW, and microstrip patch antennas were 1.75% (0.075 dB), 1.66% (0.071 dB), and 2.41% (0.103 dB).

VI. Conclusion

In this paper, we presented TRP measurement results inside an RC obtained with a power-calibrated VNA at millimeter-wave frequencies. We derived TRP expressions in terms of wave parameters for the two different cases: 1) for accessible DUT antenna terminals, and 2) for integrated DUT antennas. In the first case, the TRP can be easily calculated by measuring power levels of forward and reflected waves. In the second case, besides measuring power levels of forward and reflected waves at the receive antenna, we also need to measure the chamber loss. Results obtained from the two different approaches were compared and showed excellent agreement within our calculated measurement uncertainties.

We performed measurement uncertainty analysis using the Microwave Uncertainty Framework, which assigns uncertainties and probability distributions to error mechanisms in the calibration, and propagates the associated uncertainties to the end result. The uncertainties we obtained agree well with uncertainty calculations in our previous research employing an unloaded RC.

Here, we showed that a power-calibrated VNA extended existing methods for radiated power measurements. Our future work will include TRP measurements of modulated signals at millimeter-wave frequencies based on an RC and power- and phase-calibrated VNA.

Acknowledgement

The authors would like to thank to Michael D. Janezic of the NIST National Advanced Spectrum and Communications Test Network (NASCTN) who provided us with a precision WR22 calibration kit needed for our measurements.

References

[1] CTIA Certification, "Test Plan for Wireless Large-Form-Factor Device Over-the-Air Performance" Sep. 2016.

[2] "IEC 61000-4-21: EMC, Part 4: Testing and Measurement Techniques; Section 21: Reverberation Chamber Test Methods," Int. Electrotech. Comm., Geneva, 2011.

[3] D. A. Hill, "Electromagnetic theory of reverberation chambers," U.S. National Institute of Standards and Technology Technical Note 1506, 1998.

[4] D. Kajfez, *Q factor*, Oxford: MS: Vector Fields, 1994.

[5] "IEC 61000-4-22: EMC, Part 4: Testing and Measurement Techniques; Section 22: Radiated emissions and immunity measurements in fully anechoic rooms (FARs)," *Int. Electrotech. Comm.*, Geneva, 2010.

[6] P. Corona, G. Latmiral, E. Paolini, and L. Piccioli, "Use of reverberating enclosure for measurements of radiated power in the microwave range," *IEEE Trans. Electromagn. Compat.*, vol. 18, no. 2, pp. 54–59, May 1976.

[7] D. A. Hill, D. G. Camell, K. H. Cavcey, and G. H. Koepke, "Radiated emissions and immunity of microstrip transmission lines: theory and reverberation chamber measurements," *IEEE Trans. Electromagn. Compat.*, vol. 38, no. 2, pp. 165–172, May 1996.

[8] M. B. Slocum and M. O. Hatfield, "Evaluation of proposed IEC reverberation chamber methodology for radiated emissions measurements using a reference radiator," in *IEEE Int. Symp. Electromagn. Compat.*, pp. 734–739, Aug. 13–17, 2001.

[9] H. G. Krauthäuser, "On the measurement of total radiated power in uncalibrated reverberation chambers," *IEEE Trans. Electromagn. Compat.*, vol. 49, no. 2, pp. 270–279, May 2007.

[10] C. Orlenius, P. Lioliou, M. Franzén, and P-.S. Kildal, "Measurements of total radiated power of UMTS phones in reverberation chamber," in *European Conference on Antennas Propag., EuCAP*, Nov. 11–16, 2007.

[11] V. Monebhurrun, T. Letertre, "Total radiated power measurements of WiFi devices using a compact reverberation chamber," in *IEEE Int. Symp. Electromagn. Compat.*, Jan. 12–16, 2009.

[12] P. Roblin, *Nonlinear RF circuits and nonlinear vector network analyzers*, New York: Cambridge University Press, 2011.

[13] T. S. Rappaport, S. Sun, R. Mayzus, H. Zhao, Y. Azar, K. Wang, G. N. Wong, J. K. Schulz, M. Samimi, and F. Gutierrez, "Millimeter wave mobile communications for 5G cellular: It will work!," *IEEE Access*, vol. 1, pp. 335–349, 2013.

[14] Keysight Technologies Application Note 5988-9215EN, "Fundamentals of RF and microwave power measurements (Part 3)," USA, August 1, 2014.

[15] D. Senic, K. A. Remley, C.-M. Wang, D. F. Williams, C. L. Holloway, D. C. Ribeiro, and A. T. Kirk, "Estimating and reducing uncertainty in reverberation-chamber characterization at millimeter-wave frequencies," *IEEE Trans. Antennas and Propag.*, vol. 64, no. 7, pp. 3130–3140, Jul. 2016.

[16] D. F. Williams, NIST Microwave Uncertainty Framework, Beta Version. NIST, Boulder, CO, USA, Jun. 2014. Available online: https://www.nist.gov/services-resources/software/wafer-calibration-software

[17] J. A. Jargon, D. F. Williams, T. M. Wallis, D. X. LeGolvan, and P. D. Hale, "Establishing traceability of an electronic calibration unit using the NIST Microwave Uncertainty Framework," in *79th ARFTG Conf. Dig*, Montreal, QC, Canada, Jun. 2012, pp. 32–36.

[18] D. Senic, D. F. Williams, K. A. Remley, C.-M. Wang, C. L. Holloway, Z. Yang, and K. F. Warnick, "Improved antenna efficiency measurement uncertainty in a reverberation chamber at millimeter-wave frequencies," *IEEE Trans. Antennas Propag.*, IN PROCESS

Development of a Reference Wafer for On-Wafer Testing of Extreme Impedance Devices

H. Votsi*‡, I. Roch-Jeune†, K. Haddadi†, C. Li‡, G. Dambrine†, P. H. Aaen*, N. Ridler‡
*Advanced Technology Institute, University of Surrey, Guildford, United Kingdom
†Institute of Electronics, Microelectronics and Nanotechnology, University of Lille, Lille, France
‡National Physical Laboratory, Teddington, United Kingdom

***Abstract*—This paper describes the design, fabrication, and testing of an on-wafer substrate that has been developed specifically for measuring extreme impedance devices using an on-wafer probe station. Such devices include carbon nano-tubes (CNTs) and structures based on graphene which possess impedances in the kΩ range and are generally realised on the nano-scale rather than the micro-scale that is used for conventional on-wafer measurement. These impedances are far removed from the conventional 50-Ω reference impedance of the test equipment. The on-wafer substrate includes methods for transforming from the micro-scale towards the nano-scale and reference standards to enable calibrations for extreme impedance devices. The paper includes typical results obtained from the designed wafer.**

***Index Terms*—Calibration, on-wafer measurement, nano-scale, co-planar waveguide, RF nanotechnology, extreme impedance measurement.**

I. Introduction

New nano-scale device and material technologies are rapidly emerging to support the Internet-of-Things (IoT), wearable electronics and quantum computing. These new devices derive their advantages from material properties and physical dimensions. Universal high-frequency techniques and standards are required to measure accurately and characterize these devices for their further use in new applications. The intrinsic high impedances (kΩ) of these devices are significantly higher than the 50-Ω reference impedance of the measurement equipment [1]. This is the main barrier to characterize accurately such devices using the available test equipment, as a highly sensitive system will be required to account for the high reflections generated by these devices [2]. In addition, the dimensions of these devices are three orders of magnitude smaller than the available microwave probes. This paper describes a reference wafer that contains access structures and calibration standards that deal with the change in mechanical dimensions to enable reliable on-wafer metrology of nano-scale devices.

Research has been published to date on physically accessing nano-scale devices, using conventional measurement systems, via a co-planar waveguide (CPW) that is tapered down to a few μm [3]- [5]. The reference wafer described in this paper includes similar access structures. The wafer also includes calibration standards that enable the reference planes of the measurements to be moved to the device-under-test (DUT). The standards enable several calibration techniques to be investigated for high-frequency characterization at this scale.

II. Design

The design of the access structures is based on a ground-signal-ground (GSG) CPW transmission line similar to [3]. Fig. 1 shows the dimensions of an open-circuit structure used as one of the calibration standards. Going from left to right in Fig. 1, the signal conductor width is 100 μm and the separation between the signal and ground conductors is 66 μm. The signal and ground conductors are then tapered so that the signal conductor width is reduced to 4 μm. The same methodology can be extended to narrower lines, however the dimensions were limited by the uncertainty of the fabrication process. This provides a position where a nano-scale device can be placed and subsequently measured. The conductor metal used is gold (Au) of 500 nm thickness on a 400 μm gallium arsenide (GaAs) dielectric substrate. A 25 nm titanium (Ti) layer was used beneath the Au to enhance adhesion to the substrate. The dimensions of the CPW were chosen to preserve a 50-Ω characteristic impedance (Z_0) at all places along the CPW line. This minimizes reflections originating from the structures, and thus transfers the maximum amount of the signal to the DUT.

The calibration standards included on the fabricated wafer are five lines having lengths of 0.5 mm, 1 mm, 2 mm, 3 mm and 5 mm, five offset shorts with different phase delays designed for 15 GHz, open, short, 50-Ω load, and thru. In addition, empty one-port and two-port structures with gaps between 2 μm and 20 μm were included to enable nano-scale devices to be placed and measured. Calibration standards were designed to perform a two-tier calibration moving the

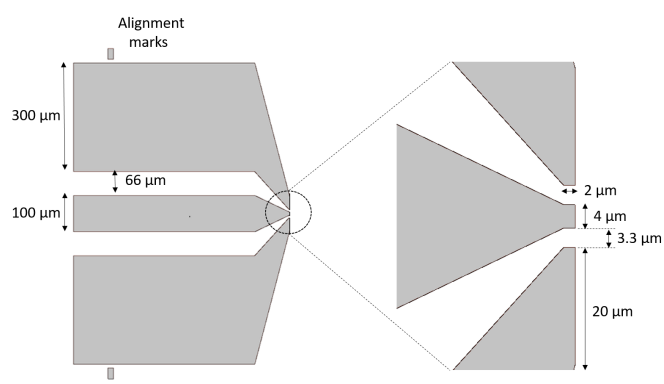

Fig. 1. Open-circuit calibration standard included in the fabricated wafer. The dimensions shown were selected to achieve a 50-Ω characteristic impedance across the entire structure.

978-1-5090-4514-3/16/$31.00 ©2016 IEEE

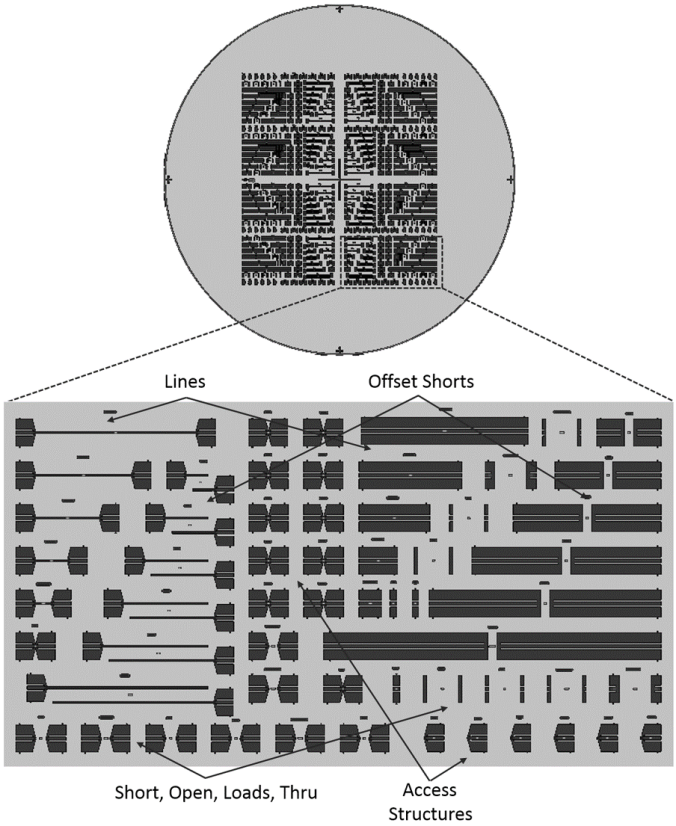

Fig. 2. Layout of the fabricated 3 inch wafer including all the access structures and calibration standards.

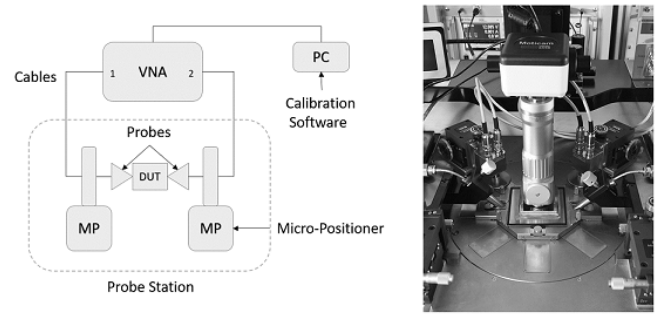

Fig. 3. (Left) Simplified block diagram of the two-port test set-up, (Right) Photograph of the measurement set-up at n3m-labs.

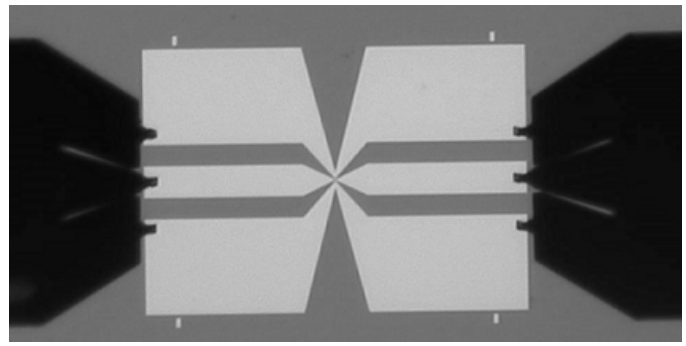

Fig. 4. Back-to-back access structure measured using two GSG probes.

reference plane of the measurement from the tips of the microwave probes to the end of the tapered conductor line of the CPW.

III. FABRICATION

The fabrication of the wafer was performed at the Institute of Electronics, Microelectronics and Nanotechnology (IEMN, RENATECH). The resistive layer (Ti) used for the load standards has thickness of 23 nm. The process flow is based on conventional optical lithography, metal evaporation and liftoff steps. Scanning electron microscope (SEM) based images show a dispersion of the structure dimensions over the full wafer less than +/- 300 nm. The variation in the thickness of the metallic layers, obtained by atomic-force microscopy (AFM) measurements, is between +/- 10 nm and +/- 1.5 nm for Au and Ti layers respectively. Fig. 2 shows the 3 inch wafer designed and it includes eight copies of the access structures and calibration standards.

IV. MEASUREMENT SET-UP

Initial measurements were performed on the fabricated structures to verify, by comparing with electromagnetic simulations, that they have been designed and fabricated correctly. For the S-parameter measurements, a Keysight N5247A PNA-X Vector Network Analyzer was used. The on-wafer probes used were MPI Titan 26 GHz GSG probes with 150 μm pitch.

The system was calibrated up to the probe tips by the short-open-load-thru (SOLT) calibration method using an MPI AC-2 impedance standard substrate [6]. The measurement configuration using an MPI TS-2000 probe station located at n3m-labs[1] is shown in Fig. 3. QAlibria software was used to calibrate the VNA and to obtain the corrected results [7]. The frequency range of the measurement was set to 0.1-26 GHz with 100 Hz IF bandwidth.

V. STRUCTURE MEASUREMENTS

Measurements were performed on two different back-to-back access structures included in the fabricated wafer. This structure will be used as a thru calibration standard when measuring a nano-scale device in order to move the reference plane of the measurement to the end of the tapered line. One of the these back-to-back structures is shown in Fig. 4.

The reflection (S_{11}) and transmission (S_{21}) coefficients obtained for the measurements and electromagnetic simulation of these back-to-back structures are shown in Figs. 5 and 6 respectively. The simulation and design of the structures was performed using *em* from Sonnet Software [8]. For the simulation 50-Ω ports were used in a single mode CPW structure. The simulated structure includes a 500 nm Au

[1]n3m-labs is the joint NPL/University of Surrey Nonlinear Microwave Measurement and Modeling Laboratories, n3m-labs.org.

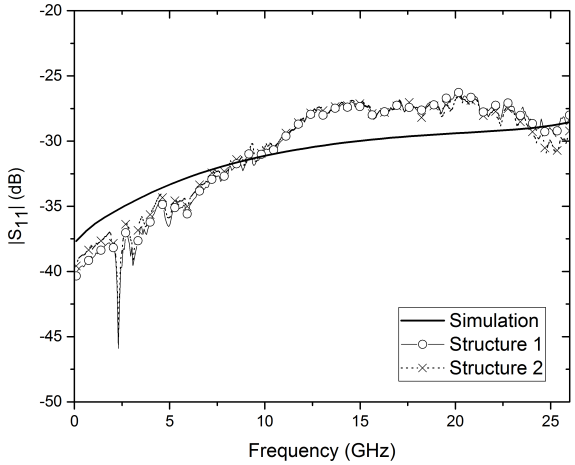

Fig. 5. Simulated and measured reflection coefficient of the back-to-back access structure.

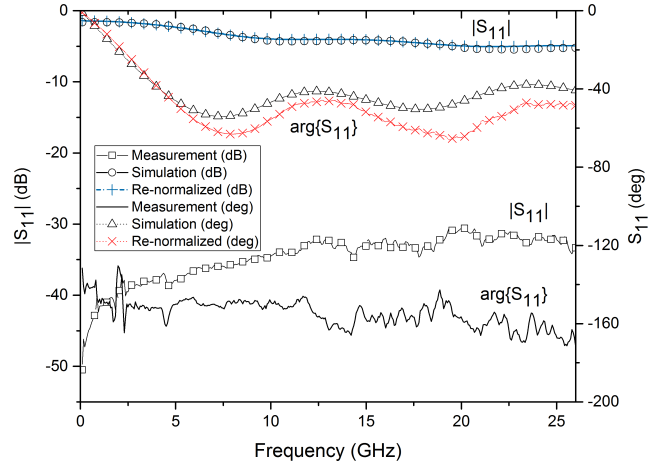

Fig. 7. Measured and simulated reflection coefficient of the 5-mm line.

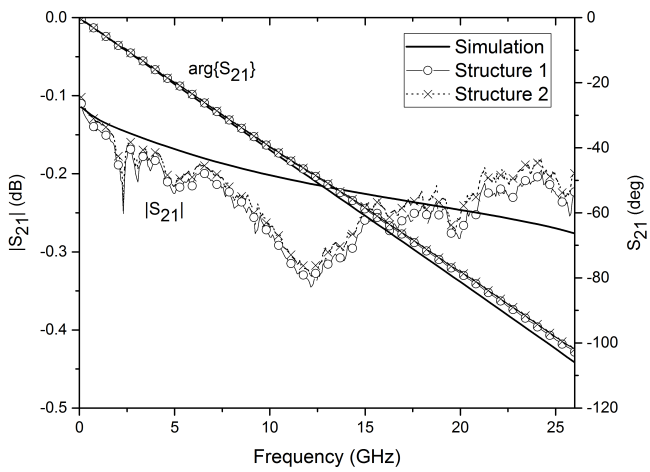

Fig. 6. Simulated and measured transmission coefficient of the back-to-back access structure.

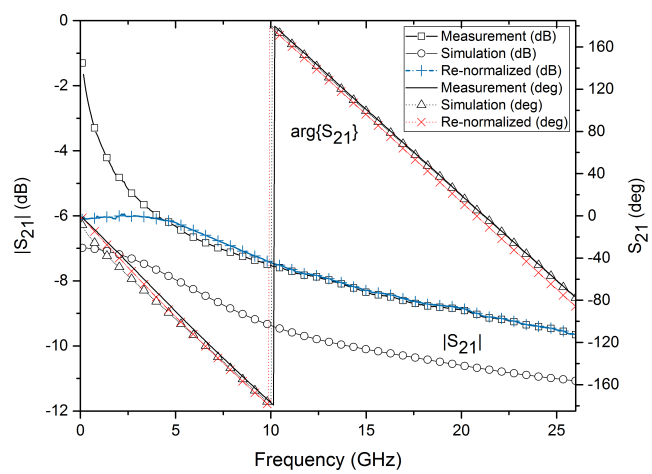

Fig. 8. Measured and simulated transmission coefficient of the 5-mm line.

metallization with conductivity of 3.8×10^7 S/m on a 400 μm GaAs dielectric with a relative dielectric constant (ϵ_r) of 12.9 and resistivity of 1 MΩ·m.

The measurement results show that the reflection coefficient is lower than -25 dB at all frequencies and therefore the designed structures have an approximately 50-Ω characteristic impedance. Moreover, there is good agreement between the simulated and measured data. A plot of the reflection coefficient's phase is not included because phase becomes indeterminate when the magnitude of a signal is relatively small (i.e. compared to the measurement system noise floor).

VI. Device Measurements

Since the S-parameter measurements of the access structures have shown that they behave as expected, a measurement of a device was implemented using the access structures and calibration standards included on the reference wafer. The same measurement set-up as before was used. A multi-line thru-reflect-line (TRL) [9], [10] calibration was conducted to move the reference plane of the measurement to the DUT. One of the back-to-back structures measured was used as the thru standard, an open was used as the reflect standard and four lines with lengths of 0.5 mm, 1 mm, 2 mm and 3 mm as the line standards. A 5-mm line included on the wafer was used as the device to be measured.

The line standards, due to the small physical dimensions at the sub-micro scale, are very lossy having a high characteristic impedance [11] expressed by $Z_0 = (R + j\omega L)/(G + j\omega C)$ where R is the resistance per unit length, L is the inductance per unit length, G is the conductance of the dielectric per unit length, C is the capacitance per unit length and ω is the angular frequency.

Through simulation the characteristic impedance of one of the line standards was calculated. This impedance has to be accounted for as it is a critical parameter for an accurate TRL calibration. Using (1) and (2) [12] the measured S-parameters were re-normalized to the 50-Ω reference impedance of the system.

$$S_{NORM} = (S_{MEAS} - XI)(I - S_{MEAS}X)^{-1} \quad (1)$$

$$X = (Z_{Line} - Z_{REF})/(Z_{Line} + Z_{REF}) \quad (2)$$

where S_{NORM} are the re-normalized S-parameters, S_{MEAS} are the measured S-parameters, I is the identity matrix, Z_{Line} is the characteristic impedance of the line standard and Z_{REF} is the reference impedance of the measurement system.

The S-parameter measurements of the 5-mm line are shown in Figs. 7 and 8. The measured data do not match the simulated data because they are referenced to the characteristic impedance of the line standard, whereas the simulated data are referenced to 50 Ω. The re-normalized S-parameters of the measured data match the simulation data more closely. This indicates that the reference plane of the measurement has been successfully moved to the DUT due to the calibration.

VII. Conclusion

The design and fabrication of a reference wafer containing access structures and calibration standards enabling the measurement of nano-scale devices at microwave frequencies has been presented. The structures presented are based on a CPW design, moving the reference plane of the measurement from the conventional micro-scale to the sub-micro scale.

Now that the structures and standards have been verified, they will be utilized in the near future to develop a new method which transforms the 50-Ω reference impedance of the test equipment to the kΩ range for the accurate characterization of extreme impedance nano-scale devices. In addition, the validity of different calibration techniques for nano-scale microwave measurements will be investigated using the calibration standards included on the wafer.

Acknowledgment

The work described in this paper was funded and supported by the research project 14IND02 PlanarCal "Microwave measurements for planar circuits and components" sponsored by the European Metrology Programme for Innovation and Research (EMPIR) and the UK Engineering and Physical Sciences Research Council (EPSRC) grant EP/L02263X/1.

References

[1] T. Ryhnen, M. Uusitalo, O. Ikkala, and A. Krkkinen, *Nanotechnologies for Future Mobile Devices*, Cambridge University Press, 2010.

[2] H. Happy, K. Haddadi, D. Theron, T. Lasri, and G. Dambrine, "Measurement techniques for RF nanoelectronic devices: new equipment to overcome the problems of impedance and scale mismatch," *IEEE Microw. Mag*, vol. 415, no. 1, pp. 30-39, 2014.

[3] K. Kim, T. M. Wallis, P. Rice, C. J. Chiang, A. Imtiaz, P. Kabos, and D. S. Filipovic, "A framework for broadband characterization of individual nanowires," *IEEE Microw. Compon. Lett.*, vol. 20, no. 3, pp. 178-180, 2010.

[4] T. M. Wallis, D. Z. Gu, A. Imtiaz, C. S. Smith, C. J. Chiang, P. Kabos, P. T. Blanchard, N. A. Sanford, and K. A. Bertness, "Electrical characterization of photoconductive GaN nanowires from 50 MHz to 33 GHz," *IEEE Trans. Nanotechnol.*, vol. 10, no. 4, pp. 832-838, 2011.

[5] C. L. Hsu, G. Ardila, and P. Benech, "A de-embedding technique for metallic nanowires in microwave characterization," *Microelectronic Eng.*, vol. 112, pp. 241-248, 2013.

[6] MPI, "AC-2 Calibration Substrate" 2015. [Online]. Available: http://www.mpi-corporation.com/PDFFiles/AC2Manual.pdf.

[7] MPI, "MPI QAlibria®- RF calibration software" 2016. [Online]. Available: http://www.mpi-corporation.com/ast/mpi-rf-probes-accessories/mpi-qalibria-rf-calibration-software/.

[8] Sonnet Software, "High frequency electromagnetic software," 2016. [Online]. Available: http://www.sonnetsoftware.com/.

[9] G. F. Engen and C. A. Hoer, "Thru-reflect-line - improved technique for calibrating the dual 6-port automatic network analyzer," *IEEE Trans. Microw. Theory Techn.*, vol. 27, no. 12, pp. 987-993, 1979.

[10] R. B. Marks, "A multiline method of network analyzer calibration," *IEEE Trans. Microw. Theory Techn.*, vol. 39, no. 7, pp. 1205-1215, 1991.

[11] D. F. Williams, U. Arz and H. Grabinski, "Characteristic-impedance measurement error on lossy substrates," *IEEE Microw. Compon. Lett.*, vol. 11, no. 7, pp. 299-301, 2001.

[12] K. Kurokawa, "Power waves and the scattering matrix," *IEEE Trans. Microw. Theory Techn.*, vol. 13, no. 2, pp. 194-202, 1965.

The Impact of ENR and Coaxial Calibration in Accurate On-Wafer Noise Parameter Testing for Ultra-Low Noise Devices

Kevin Kellogg[1], Larry Dunleavy[1], Scott Skidmore[1], Gary Simpson[2]

[1]Modelithics Inc., Tampa, FL, 33620, USA, [2]Maury Microwave Corporation, Ontario, CA, 91764, USA,

***Abstract* — A revealing case study is presented to explore the impact of excess noise ratio (ENR) and vector network analyzer (VNA) mechanical coaxial calibration on accurate on-wafer noise parameter testing for ultra-low noise devices. On-wafer noise parameter tests were conducted on a GaAs pHEMT device from 2-50 GHz after calibration with three different noise sources. For each, ENR specified from an external calibration service and also with ENR measured internally using vector corrected noise power measurements with appropriate coaxial calibration kits. Initial results show that significant variation in noise parameters, especially Fmin can result from seemingly subtle differences in ENR values as well as coaxial calibration accuracy. Excellent agreement is demonstrated for noise parameter measurements made with the three different noise sources, after using in-house measured ENR values and eliminating the use of a suspect coaxial calibration kit.**

***Index Terms* — Calibration, Low Noise Amplifier, Microwave Measurement, Noise Figure, Noise Parameters.**

I. Introduction

Accurate noise parameters are able to provide a complete description of a linear device's noise figure and sensitivity to changes in source impedance when presented with any realizable source and load impedance. These parameters are incredibly important to fully describe due to finite dynamic range considerations, particularly in the transmit/receive applications that dominate our current communications systems.

The measurement of noise of an active device has undergone a dramatic transformation over the past 50 years evolving from the arduous and time consuming, single-frequency manual methods with offline computer routines [1,2] into automated, repeatable methods that are able to retain accuracy swept from a few GHz up to 50 GHz gathering more than a thousand data point in a few minutes' time [3].

Although the noise parameters, Fmin (minimum noise figure), Γopt (complex source reflection coefficient at Fmin), Rn (equivalent noise resistance) only require a minimum of four measured source impedances per frequency [4], the standard approach is to apply a least-mean-squares algorithm to reduce the over-determined dataset, which results in a more robust solution [1]. This method of noise parameter measurements has been in use for some time in commercial systems. The ATN NP5 system, based on the cold source impedance method [2], was for many years the most popular system in the industry for determining device noise parameters. However, recent equipment advances have led to the availability substantially improved capability in terms of measurement speed, bandwidth, cohesiveness of solution set and ease of implementation. One such system is the Maury ATS/Keysight PNA-X-based ultra-fast noise parameter measurement system [3]. This system allows for quickly gathering thousands of data points cross frequency. Improved software algorithms speed up data processing while allowing automatic deletion of bad or outlier data points. In practice, this method has allowed for increasing measurement bandwidth and solution accuracy while reducing the measurement time by approximately 1/3. Noise parameter test system set-up and calibration time have also been reduced in complexity and time requirements.

The focus of this work is on how variations in system calibration devices and input data can affect the final noise parameter results using a case study approach with a 50 GHz, Maury/Keysight noise parameter system of Fig. 1. In this system, the Keysight PNA-X provides S-parameters and noise power measurement hardware selected by the external noise source switch and internal port 2 low noise receiver switch. The enabling Maury Microwave hardware includes an automated source impedance tuner, an input module with bias tee, and an output module with bias tee and a broadband amplifier. Maury ATS software is used for system operation, calibration and device data acquisition.

Specifically explored is the impact of excess noise ratio (ENR) and vector network analyzer (VNA) mechanical coaxial calibration on accurate on-wafer noise parameter testing for an ultra-low noise GaAs pHEMT device. The study was motivated after initial difficulty with obtaining agreement between results using two different diode noise sources as part of system calibration. A third noise source was used to try to

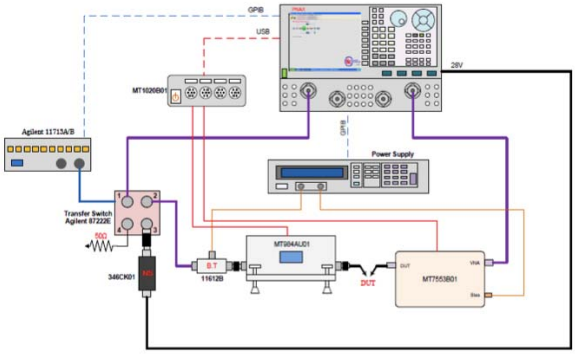

Fig. 1 Block diagram of the Maury Microwave/Keysight noise parameter measurement system.

978-1-5090-4514-3/16/$31.00 ©2016 IEEE

resolve the discrepancies observed and the differences were ultimately traced to ENR and coaxial calibration issues.

II. Method of Noise Parameter Measurement

Although a number of methods exist for the measurement of noise parameters [5], system calibration generally involves use of a diode noise source that has been characterized with a specific ENR determined over frequency through an independent calibration method,

$$\mathrm{ENR} = (T_{hot} - T_{cold})/290\mathrm{K} \qquad (1)$$

where the ENR is equal to the difference between the effective 'hot' temperature, $T_{hot,}$ and the 'cold' temperature T_{cold} (room temp[1]) in relation to 290 K [6]. This noise source is connected to a switchbox to allow for in-situ s-parameter measurements, as well as a Maury Microwave automated impedance tuner used to vary the source impedance presented to the device-under-test (DUT). A carefully calibrated receiver, in this case, the PNA-X noise receiver is used to measure the noise power delivered to the receiver at room temperature over an array of source impedances that are presented to the DUT, as seen in Fig. 1, which is a block diagram representation of the noise parameter test bench. The DUT noise is then amplified before it reaches the noise receiver to boost signal to noise ratios and minimize uncertainties. The noise power is described as

$$P = kB\{[t_{ns} + t_0 (F_1\text{-}1)]\, G_{a1} + t_0(F_2\text{-}1)\}G_{t2} \qquad (2)$$

where k is Boltzmann's constant, B is the system bandwidth, t_o is 290 K, t_{ns} is the noise source temperature in K, F_1 is the DUT noise figure, as a function of source impedance, F_2 is the receiver noise figure, as a function of DUT output impedance, G_{a1} is the DUT available gain as a function of source impedance, and G_{t2} is the receiver transducer gain, another function of source impedance [3]. The received noise powers are then de-embedded with the receiver noise figure and gain data, and attributed to the DUT.

III. Calibration Procedures

The noise parameter system must be carefully characterized in order to achieve the most accurate results. The ATS software-driven procedure is conducted as follows. The first calibration defines the DUT measurement reference plane. In the presented work, the VNA was calibrated with an on-wafer multi-line TRL calibration routine as described by Marks [7] from 2-50 GHz. This on-wafer s-parameter calibration step remained constant for all of the noise parameter results to be shown later.

[1] *T_{cold} is assumed to be 290 K for calibration.*

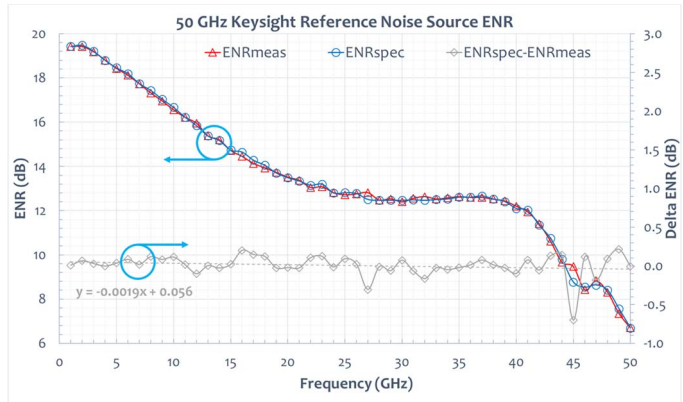

Fig. 2 Reference 50 GHz Keysight noise source, comparison of ENR specified vs. measured in-house using a 2.4 mm calibration kit.

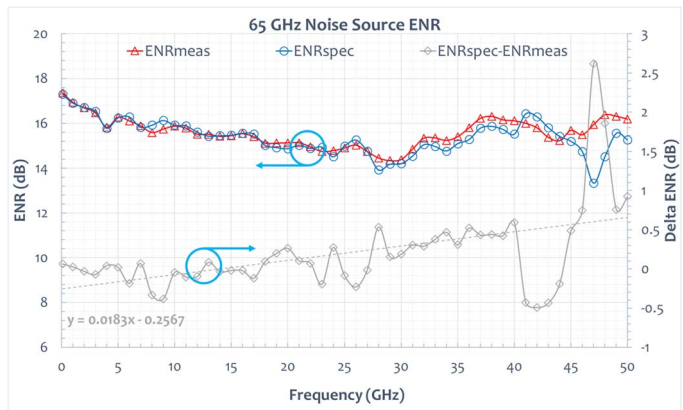

Fig. 3 65 GHz noise source comparison of ENR specified vs. measured in-house with a 1.85 mm calibration kit.

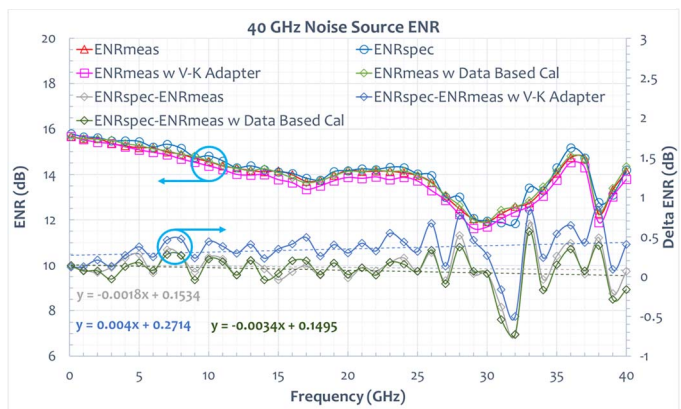

Fig. 4 40 GHz noise source, ENR comparisons of specified vs. measured in-house using a K (Anritsu 2.92 mm equivalent) calibration kit and with the ENR of the same noise source fitted with a V-K adapter and characterized with the in-house method and a 1.85 mm calibration kit.

Following on-wafer s-parameter calibration, a 1-port coaxial calibration is done at the interface to the noise source, the error terms are subtracted, and used to determine the s-parameters of the path from the noise source to the DUT. The software then automates characterization of the tuner by determining the physical tuner states that provide the best cross-frequency solution, so that frequency may be swept at each tuner state while measuring the noise power, in comparison with the much slower legacy approach, where tuner states are swept at each frequency while measuring the noise power. Next, the tuner s-parameters are de-embedded to the DUT input reference plane. The hot and cold noise source gamma as well as the system output gamma are measured, and after tuner s-parameter characterization is complete, the noise receiver is calibrated with the noise source to determine the noise parameters of the receiver.

Traditionally, the calibration of the ENR of the noise source itself has been tied to an accredited external laboratory. In this work the ENR of each source was also carefully measured in-house, by using a PNA-X low noise receiver calibrated using a broadband, high-accuracy, high dynamic range Keysight U8488A power sensor, and an electronic calibration unit used as an impedance tuner [8]. A source power calibration is performed at the measurement reference plan (or adapter whose s-parameters may be de-embedded), and a thru connection is made from this interface to port 2 to determine the swept frequency response of the noise bandwidth filter and the gain-bandwidth product and noise figure of the noise receiver. Next, a two-port coaxial calibration is performed at the same reference plane. During the calibration, the impedance tuner presents an array of impedance states to the noise receiver that are used to characterize the noise generated by the noise receiver for de-embedding to the device reference plane. Once these calibrations are complete, the ENR of the noise source may be measured directly. The comparison of the in-house measured result (ENRmeas) vs. the externally specified result (ENRspec) of the three noise sources used for FET noise parameter measurements can be seen in Fig. 2 through Fig. 4, along with the ENR difference (ENRspec – ENRmeas) and ENR difference linear fit.

IV. FET Measurements and Discussion of Results

The DUT noise parameters presented in Fig. 5 and Fig. 6 are those of an ultra-low noise pHEMT was that was measured under a single small signal operating point (bias conditions of 2 V drain-to-source with 5 mA of drain current) compared with three noise sources: a 65 GHz broad-band noise source with a 1.85 mm coaxial interface, a 40 GHz noise source with a K (Anritsu 2.92 mm equivalent) coaxial interface, and a 50 GHz Keysight 346CK01 with a 2.4 mm coaxial interface used as the reference standard ENR source. The s-parameters of the DUT are measured just before the noise parameters measurement, but these results are not presented.

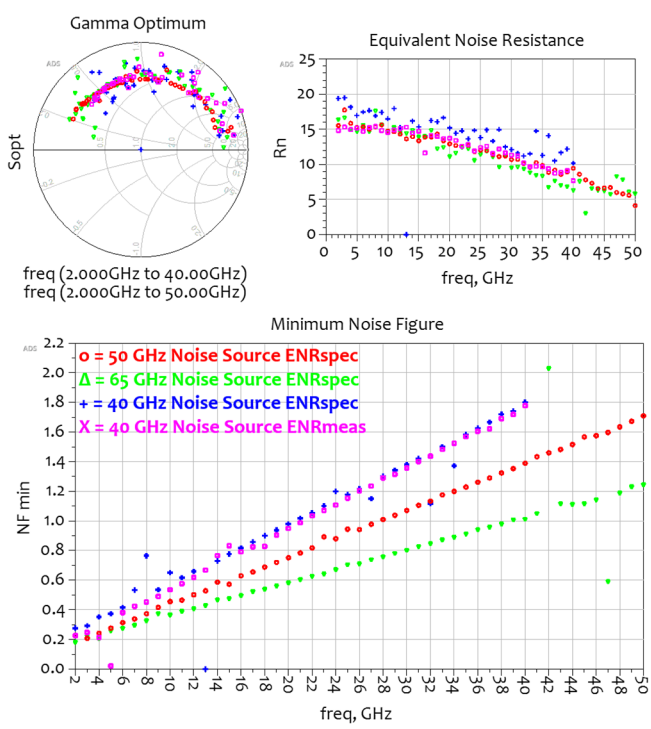

Fig. 5 Raw FET noise parameters measured from 2-50 GHz using three different noise sources with the externally calibrated ENR, plus one measurement using in-house measured ENR with the K-Cal kit

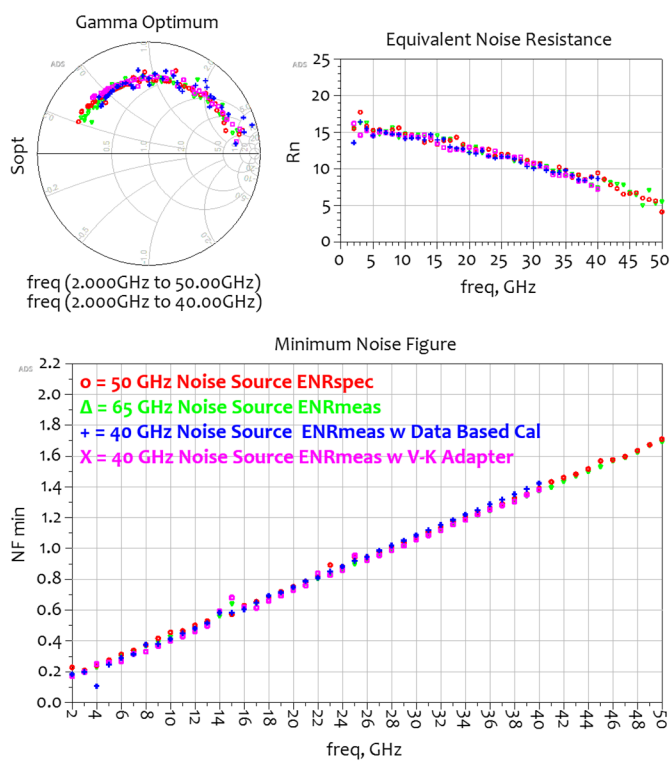

Fig. 6 Raw FET noise parameters measured from 2-50 GHz using three different noise sources with the in-house calibrated ENR.

For reference, the s-parameter response was equivalent between measurements and calibrations. All the presented measurements were taken by the same measurement system operator, and the same level of care was taken in each measurement, yet there remains a clear and distinct difference in the solutions reported value of Fmin (Fig. 5). Generally speaking, the noise parameters other than Fmin were equivalent, although it is clear that there is more scatter present in all of the noise parameter results obtained using the specified values of ENR, barring the reference 50 GHz Keysight noise source results. It should be noticed that the in-house ENR characterization produced an excellent correlation to that of the externally calibrated and specified value of the Keysight 50 GHz noise source, as seen in Fig. 2 where the average difference was 0.007 dB from the specified value, a median of 0.015 dB, and a standard deviation of 0.13 dB from 1 – 50 GHz.

The measurements of the in-house 40 GHz and 65 GHz noise sources display a lesser degree of correlation. The 40 GHz noise source measured ENR value trended in the much the same manner as the specified ENR with a nearly constant +0.15 dB offset. The 65 GHz noise source measured ENR showed a very similar trend as the specified ENR, although it displayed a frequency dependent offset, and after 45 GHz, seemingly changed trends completely. This discrepancy was later found to be the result of a faulty reference transfer standard used during an external calibration.

In an effort to determine the most correct set of values and frequency trend for Fmin of the DUT, the same DUT was then re-measured using the in-house measured ENR for each of the three noise sources, and the results are shown in Fig. 6. The 65 GHz noise source and the 40 GHz noise source characterized with a V-K adapter were now aligned with the reference 50 GHz noise source Fmin result. The notable exception remained the 40 GHz noise source whose calibration involved a K-connector calibration kit. The results suggest that the accuracy (or lack thereof) of the coaxial calibration alone resulted in an inflated Fmin result, as well as Γopt and Rn values that displays more scatter than those of the higher frequency, more accurately defined calibration kits. The difference of approximately 0.4 dB at 40 GHz is quite a significant performance variation in general and particularly when the higher frequency extrapolated result is considered.

To resolve this discrepancy, the K calibration kit was characterized with a multi-line TRL calibration, effectively transferring the higher accuracy of the TRL calibration to that of the lower accuracy SOLT calibration standard definitions. For reference, the calibration kit s-parameter response showed as much as 12% difference at 40 GHz when comparing the two results. The data based standard definitions were used in place of standard simple model definitions (lossless, delay only) and the ENR of the 40 GHz noise source was remeasured and the measurement was repeated, using the K Cal kit with data based standard definitions in the measurement of the input network and de-embedding, as well as the hot and cold noise source gammas. In addition to displaying less scatter overall in the noise parameters, the resultant Fmin measurement fell in line with the expected result seen in Fig. 6.

III. Conclusion

This work demonstrated that obtaining accurate noise parameter measurements of ultra-low noise results can be very dependent on the accuracy of noise source ENR and coaxial calibration standard calibration coefficients. The robustness and repeatability of the Maury Microwave/Keysight Technologies noise parameter system for use in ultra-low noise device measurements was exemplified by obtaining excellent agreement for a pHEMT through 50 GHz after repeated calibrations involving three different noise sources and three different coaxial calibration kits. Also demonstrated was the accuracy and consistency of the ENR measurement methods enabled by the PNA-X based noise receiver calibrated against a high dynamic range power sensor.

Acknowledgement

The authors would like to thank Hugo Morales of Modelithics for his inputs, to acknowledge Dave Ballo of Keysight Technologies, who provided insight and thoughtful suggestion on this work, as well as Rich Daigler for arranging the Keysight reference noise source for the comparison results herein. We also would like to thank Sathya Padmanabhan of Maury Microwave for arranging for the re-characterization of the K-connector calibration kit as used for the final results.

References

[1] R. Lane, "A microwave noise and gain parameter test set." Solid-State Circuits Conference. Digest of Technical Papers. 1978 IEEE International. Vol. 21. IEEE, 1978.

[2] V. Adamian, and A. Uhlir. "A novel procedure for receiver noise characterization." IEEE Transactions on Instrumentation and measurement 2.22 (1973): 181-182.

[3] G. Simpson, D. Ballo, J. Dunsmore, A. Ganwani, “A new Noise Parameter Measurement Method Results in More than 100x Speed Improvement and Enhanced Measurement Accuracy”, 72 ARFTG Microwave Measurement Conference, December 2008.

[4] G. Vasilescu, G. Alquie, and M. Krim, “Exact computation of two-port noise parameters,” Electron. Lett., vol. 25, no. 4, pp. 292–293, Feb. 1989.

[5] L. Belostotski and J. Haslett, “Evaluation of Tuner-Based Noise-Parameter Extraction Methods for Very Low Noise Amplifiers,” IEEE Trans. On Microwave Theory. And Tech., pp236-250. Jan. 2010.

[6] Application Note, “Fundamentals of RF and Microwave Noise Figure Measurements”, AN 57-1, Keysight Technologies.

[7] R. Marks, "A multiline method of network analyzer calibration." IEEE Transactions on Microwave Theory and Techniques 39.7 (1991): 1205-1215.

[8] Application Note, “High-Accuracy Noise Figure Measurements Using the PNA-X Series Network Analyzer” Keysight Technologies.

Fused Silica based RSOL calibration substrate for improved probe-level calibration accuracy

Luca Galatro, Marco Spirito

Electronics Research Laboratory (ERL), Delft University of Technology, Delft, The Netherlands,

***Abstract* — In this contribution we present a calibration substrate manufactured with integrated circuit technology on fused silica, used for reciprocal SOL calibration. The fabrication technology is described together with the standard layout, and the precise control of the geometrical properties is exploited to create accurate pitch-dependent standard model to be used during the calibration procedure. The calibration accuracy is benchmarked with the conventional alumina impedance standard substrates, using the provided (polynomial fit) standard definitions, giving an estimate of the accuracy improvement that the proposed calibration substrate can provide.**

***Index Terms* — VNA, calibration, on-wafer, probe-level, RSOL, fused silica.**

I. Introduction

The accuracy of S-parameter measurements of any device under test (DUT) is set, at the first order, by the quality of the VNA calibration. This is typically performed by measuring a certain number of known devices (i.e., the calibration standards). Depending on the specific calibration technique employed, the quality of the calibration is directly dependent on the accuracy with which the calibration standards are known/modeled [1][2]. When considering planar devices, for which wafer-probes need to be employed, it is common practice to perform a probe-level calibration (first-tier) using a low-loss substrate (i.e., alumina or fused silica), which can then be transferred to the environment where the DUT is embedded. In planar environments, the accurate modeling of the calibration standards can become cumbersome, due to ambiguity in the definition of the calibration reference plane [3] and the limited control on the accuracy with which the standards are manufactured. For this reason, calibration techniques in which little knowledge of the standards is required, like TRL [4] and LRM [5], might be preferred. However, TRL calibration results to be impractical for probe level calibrations performed on general purpose substrates when a broadband range of frequencies is considered, due to the large number of long transmission lines that would be required. Also, both TRL and LRM calibration define the calibration reference plane at the center of the (non-zero) thru standard, and not at the probe tips. While moving the reference plane to the probe tips is possible by considering single mode propagation in the thru line, this assumption is generally violated in the close proximity of the probe tips, due to higher order modes generated at the non-ideal probe-to-line transition [6]. On the other end, SOL calibration using an unknown thru (RSOL [7]) has been proven to be as accurate as TRL calibration, when a sufficiently accurate model of the standards is provided [8]-[10]. Also in this case, as the authors described in [3] and [10], the calibration reference plane can be univocally defined using EM simulations for the standard modeling. This technique also allows to create probe-independent calibration kits, as opposed to the conventional probe-paired calibration substrates [11], where the imperfections of the probe-to-line transition are embedded in the DUT instead than in the calibration error terms, leading to measurement error [3].

In order to achieve accurate calibration standard modeling, additional care should be dedicated to the manufacturing of the calibration standards. The process presented in [10], based on integrated circuit technology, and the use of fused silica as substrate, had the goal of improving the quality of the standard manufacturing with a special focus on the load, in order to increase repeatability and avoid the common practice of resistance tuning via laser trimming.

In this contribution we present a RSOL calibration kit manufactured on fused silica with the process described in [10] and its performances, in terms of measurement accuracy, when employed for VNA calibration in the frequency range from 10 MHz to 50 GHz. The paper is structured as follows, first the process technique and the layout of the calibration kit are described. Then, the modeling of the calibration standards is discussed. Finally, the proposed calibration kit is used for VNA calibration and measurements of both one port and two ports passive devices are employed to compare it towards a commercially available alumina calibration kit.

II. Fabrication technology

For RSOL as well as for LRM calibration, the variation of the load performances, both in terms of DC resistance and electromagnetic behavior, constitute one of the biggest sources of uncertainty [9][10]. In commercially available calibration kits, the load standard is typically defined by means of a purely inductive model [12]. In this, while the DC resistance is very well controlled by means of laser trimming [11], the purely inductive model results to be inaccurate since the large capacitive loading provided by the contacting metal stripes is neglected [10]. At the same time, the laser trimming procedure, while keeping the resistance value highly repeatable, poses a limit in the EM modeling of the load standard, since the geometrical modifications generated during the trimming procedure are not predictable. The only way to avoid laser trimming is to use a fabrication process that could

978-1-5090-4514-3/16/$31.00 ©2016 IEEE

allow very precise control of the geometrical properties (width/thickness) of the resistive layer. In this framework, a lithographic process like the one proposed in [10], featuring a layer thickness variation in the order of 1% across a single 2x2 cm^2 and horizontal accuracy in the order of parts of nanometer, can represent a good candidate for the manufacturing of a precision RSOL calibration substrate.

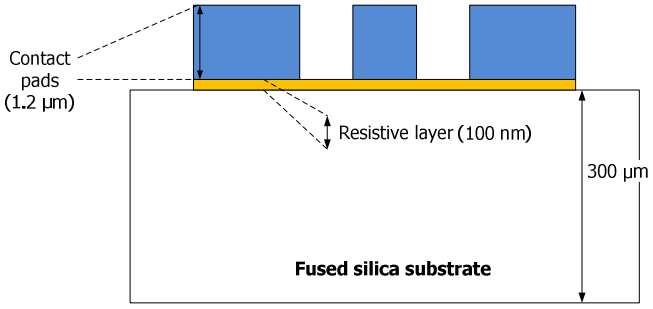

Fig. 1: Schematic cross section of the 50 Ω resistors fabricated on the proposed fused silica substrate

Fig. 1 shows a simplified schematic cross section of a calibration load manufactured in the proposed technology. The resistive layer with controlled thickness is first deposited, then patterned by means of lithography. The contact pads are then deposited on top of the resistive layers, in order to guarantee a good ohmic contact between the low resistivity material of the pad (aluminum) and the high resistivity material used for the resistance.

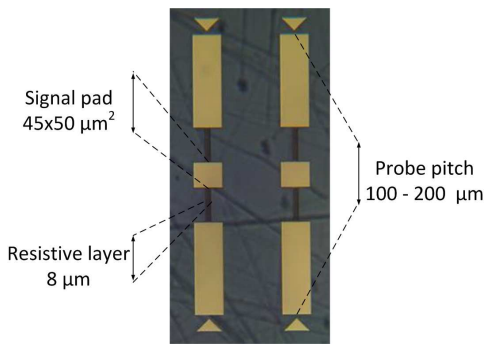

Fig. 2: Load standard artifact realized using the proposed technology

For the other standards (short, open and thru) the same manufacturing process is used, with the low resistivity material always deposited on top of the high resistivity layer. Fig. 2 shows one of the load artifact realized on the proposed technology. All the designed structures feature a 45x50 μm^2 signal pad, and a geometry which can allocate probe pitches in the range 100-200 µm.

III. Simulation setup

In order to realize an accurate model for the calibration devices manufactured as described in section II, EM simulators have been employed. Being the structures mostly planar, a 2.5D full-wave EM environment (i.e., Keysight Momentum) can be considered of sufficient accuracy for the purpose. For each calibration standards, the material properties and geometrical characteristics (width and length) have been defined as provided by the manufacturer. The resistive layer thickness value has been extracted by means of DC measurements, using the width, length and resistivity as constants. The contact of wafer probes is simulated by means of internal ports, and different models have to be defined for different probe pitches, since the behavior of the standards is dependent on the distance between the stimuli. On the other hand, as described in [10], the impact of probe displacement on the wafer pads during an RSOL calibration is weak, for this reason the ports can be safely placed at the center (in the x direction) of the pads, i.e., at 25 µm from the border, without losing in generality, as depicted in Fig. 3a. The result is a pitch-dependent model, but no other probe effect needs to be taken into account, while the calibration reference plane will be only weakly sensitive on the probe positioning.

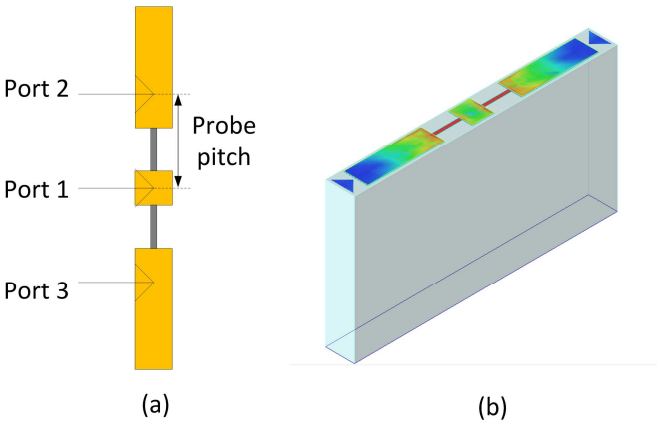

Fig. 3: a) Simulation setup in Keysight momentum for the load standard. The port positioning depends upon the targeted probe pitch. b) 3D model of the load standard after simulation, indicating field density over the conductor and resistive layer surface.

After the simulations, the S-parameters of each standard can be extracted, and then used as calibration standard model instead of using the probe-paired calibration coefficients.

IV. Experimental results

Once the calibration kit is manufactured and properly modeled, the performances can be evaluated by means of comparison. In order to do that, measurements have been performed in the frequency range from 10 MHz to 50 GHz, employing a set of Cascade Microtech Infinity i50 probes with 125 µm pitch, using Cascade Microtech Wincal XE ver. 4.5

for the data acquisition and calibration computation. First a RSOL calibration has been performed by using the calibration kit presented in section II in combination with the model realized as described in section III, and the error terms have been saved. Then another RSOL calibration has been conducted on a Cascade Microtech ISS model 101-190C [12], using manufacturer definitions for the standards. Finally, a unique set of raw measurements has been conducted on different DUTs: a set of different loads manufactured with the technology described in section II (0.35 Ω, 0.45 Ω, 41 Ω, 4500 Ω, 6800 Ω), two CPW lines realized on fused silica (726 μm, 1422 μm), a verification line from the ISS substrate (1800 μm) and a CPW line realized on SiGe BiCMOS 130nm technology (600 μm). The two different calibrations have been then applied to each one of the raw measurements. In order to compare the performance of the calibration, the method of [6] has been employed, using simulation data as reference, and defining two different worst case error bounds for the loads and for the transmission lines:

$$WC_{load} = \max\left|S_{ii,n}^{k} - S_{ii,n}^{Ref_k}\right| \quad (1)$$

$$WC_{line} = \max\left|S_{ij,n}^{w} - S_{ij,n}^{Ref_w}\right| \quad (2)$$

Where S^{Ref} is the S-parameter associated to the reference data, with k associated to the load standards and w associated to the line standards, $S^{k}ij_{,n}$ is the nth s-parameter measured with $n \in [1 \div 2]$ being the considered error set, and $i, j \in [1,2]$.

The results of this comparison are two synthetic figures of merit, comprehensive of all the performed measurements, summarizing the error committed by employing a specific calibration technique, and are shown in Fig. 4. When measuring transmission lines (see, Fig. 4a, full squares for fused silica calibration, asterisks for ISS calibration), where the sources of error are dominated by the probe displacement on the transmission lines that are not accounted for by the simulations, both errors tend to increase with frequency. However, fused silica based calibration performs better than ISS in the entire frequency range, with an error 2,5 times smaller at 50 GHz. When the one port measurements are considered, probe displacement error has very small impact on the calibration accuracy [10]. In this case, the error will be mainly determined by the accuracy of the standard definition. As shown in Fig. 4b, while the error associated to the calibration on fused silica is constant versus frequency, the error associated to the conventional ISS calibration is frequency dependent and results to be always higher than the error committed when measuring with the method proposed in this paper (see, Fig. 4b), with a discrepancy that can reach one order of magnitude at 50 GHz.

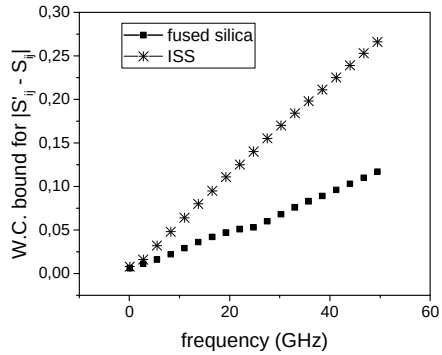

a)

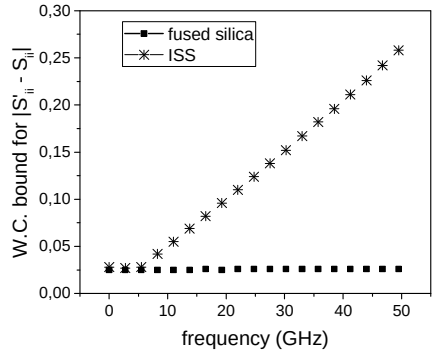

b)

Fig. 4: Worst case error bound for a) measurements of transmission line and b) measurements of one port loads, obtained by using fused silica calibration (■) and ISS calibration (*).

Additional insight can be obtained by considering the impedances of the loads as measured with the two calibrations, as shown in Fig. 5. To exemplify the problem, we focus on the measurements of a very low impedance load, featuring a DC resistance of 0.35 Ω (see, Fig. 5, red curves) and a very high impedance load, with a DC resistance of 4500 Ω (see, Fig. 5, black curves). For the real part of the impedance, both calibrations give results close to simulations (see, Fig. 5a). However, when the imaginary part of the impedance is considered, the ISS calibration is only valid at very low frequencies, while fails to predict the correct values as the frequency increases (see, Fig. 5b). Particularly interesting is the measurement of the very high impedance load, where the ISS calibration shows a positive value for the imaginary part of the impedance, totally neglecting the mainly capacitive behavior of the DUT, which instead is accounted for by the fused silica calibration. This behavior can be easily associated to the inaccurate inductive model of the ISS load, as also described in [10].

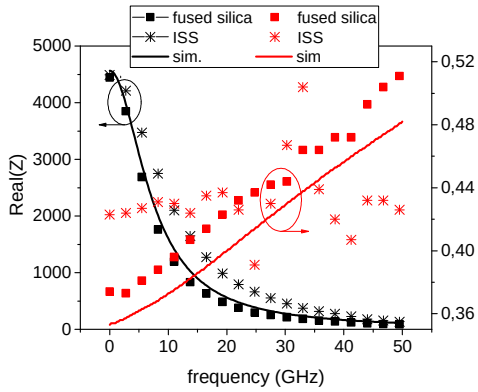

a)

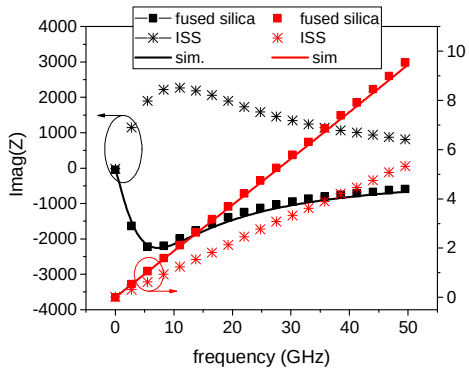

b)

Fig. 5: a) Real and b) Imaginary part of the impedance extracted from the measurements of a 4500 Ω (black curves and symbols) and a 0.35 Ω (red curves and symbols) obtained by using fused silica calibration (■) and ISS calibration (*) as compared to simulations (solid lines).

V. Conclusions

In this paper, we presented the implementation of an RSOL calibration substrate manufactured on fused silica using integrated circuit technology. The high accuracy of the manufacturing process allows avoiding laser trimming for the definition of load standard DC resistance. When used in combination with EM simulation based calibration standard models, this calibration kit allows to avoid non-physical behaviors in s-parameter and impedance measurements while also improving measurement accuracy in respect to calibration kits provided with lumped probe-paired calibration standard definitions.

Acknowledgement

This project has received funding from the European Metrology Programme For Innovation And Research (EMPIR) PlanarCal 14IND02 project. The EMPIR initiative is co-funded by the European Union's Horizon 2020 research and innovation programme and the EMPIR participating states.

References

[1] K. Wong and J. Hoffmann, "Improve VNA Measurement Accuracy by Including Connector Effects in the Models of Calibration Standards". *ARFTG Conf. Dig.*, Columbus, OH, 2013, pp 1 - 7.

[2] F. Mubarak and J. Hoffmann, "Effects of Connectors and Improper Mounting of Air Lines in TRL Calibration", in *Conference on precision electromagnetic measurements (CPEM)*, Ottawa, Canada, 2016.

[3] L. Galatro, F. Mubarak and M. Spirito, "On the definition of reference planes in probe-level calibrations," *ARFTG Conf. dig.*, San Francisco, CA, 2016, pp. 1-4.

[4] G. F. Engen and C. A. Hoer, "Thru-Reflect-Line: An Improved Technique for Calibrating the Dual Six-Port Automatic Network Analyzer," *IEEE Trans. Microw. Theory Techn.*, vol. 27, no. 12, pp. 987-993, Dec. 1979.

[5] H. J. Eul and B. Schiek, "Thru-Match-Reflect: One result of a rigorous theory for deembedding and network analyzer calibration," in *IEEE European Microwave Conf*, Sept. 1988, pp. 909-914.

[6] D. F. Williams and R. B. Marks, "Calibrating On-Wafer Probes to the Probe Tips," *ARFTG Conf. Dig.*, Orlando, FL, USA, 1992, pp. 136-143.

[7] A. Ferrero, U. Pisani, "Two-port network analyzer calibration using an unknown 'thru'," in *IEEE Microw. and Guided Wave Lett.*, vol.2, no.12, pp.505-507, Dec. 1992

[8] M. Imparato, T. Weller, L. Dunleavy, "On-Wafer Calibration Using Space-Conservative (SOLT) Standards", *IEEE MTT-S Int. Microw. Symp. Dig*, Anaheim, CA, USA, 1999, pp. 1643-1646.

[9] S. Padmanabhan, L. Dunleavy, J. E. Daniel, A. Rodriguez, and P. L. Kirby, "Broadband space conservative on-wafer network analyzer calibrations with more complex load and thru models," *IEEE Trans. Microw. Theory Tech.*, vol. 54, no. 9, pp. 3583–3593, Sep. 2006.

[10] M. Spirito, L. Galatro, G. Lorito, T. Zoumpoulidis, F. Mubarak, "Improved RSOL planar calibration via EM modelling and reduced spread resistive layers," *ARFTG Conf. Dig.*, Atlanta, Georgia, USA, Dec. 2015.

[11] Cascade Microtech, "On-Wafer Vector Network Analyzer Calibration and Measurements", Appl. Note, (online). Available https://www.cascademicrotech.com/files/ONWAFER.pdf

[12] Cascade Microtech (Online). Available: https://www.cascademicrotech.com/files/iss_map_101-190.pdf

Kicking the Tires of the NIST Microwave Uncertainty Framework, Part 1

Ronald A. Ginley
National Institute of Standards and Technology (NIST) RF Technology Division
325 Broadway, mc 672.01, Boulder, CO 80305, USA, rginley@boulder.nist.gov

***Abstract* — As with anything new, especially metrology tools, you want to know how good the new tool is. This is generally done through comparisons with existing systems. In this paper, such a comparison is described. The new NIST method of processing measurements and uncertainties, the Microwave Uncertainty Framework will be compared to the established NIST method for measuring one and two-port scattering-parameters. The setup of the comparison, results, and a discussion of the results will be covered. This paper, Part 1, will cover the comparison of the responses generated by the different methods. Part 2 will discuss the comparison of the uncertainties calculated with the different approaches.**

***Index Terms* — Microwave measurements, coaxial connectors, s-parameters, uncertainties**

I. Introduction

As with anything new you want to see how good it is. The colloquial expression for this is "kicking the tires" which has been defined as "checking the viability of an unknown system by a quick test" (derived from literally kicking the tires of an automobile). In the world of microwave metrology we have more formal approaches to testing the viability of a new analysis or measurement approach. The comparison of results and uncertainties from different techniques is one of the standard methods used to evaluate new approaches.

The NIST Microwave Uncertainty Framework (or Framework or MUF for short) is a recently developed tool for producing measurement results and uncertainties [1-5]. The ability of the MUF to produce accurate results must be verified and this will be done by comparing the MUF results against the existing technique used at NIST. The established technique used at NIST for s-parameter measurements is the multiline method for network analyzer calibration [6]. The multiline method is applied in a NIST software package titled "Multical." Data is taken from the Vector Network Analyzer (VNA) and analyzed using other NIST software packages.

II. Kicking the Tires – How do you kick a tire?

There are several steps involved in this comparison process. The VNA needed to be calibrated both with the multiline method and the method employed in the MUF (a version of the multiline calibration). Next, data was taken for a series of devices under test (DUTs). A set of six DUTs were measured, three one-ports (two matched terminations and an offset short) and three two-ports (a low-loss device, 20 dB and 50 dB attenuators). All of the devices, calibration standards and DUTs, had 3.5 mm connectors and the frequencies measured were from 0.2 to 33.0 GHz by 0.1 GHz steps. Finally, the corrected DUT results were compared.

The MUF process can be described as: take raw measurements of the calibration standards and the DUTs, the MUF will then generate the error correction coefficients based on the raw calibration standards' data, finally the correction coefficients are applied to the DUT raw data to get the final results. The established NIST technique is a bit different: take raw measurements of the calibration standards, use Multical to generate the correction coefficients, download these to the VNA, then take corrected measurements of the DUT.

The specifics of the actual process steps are as follows:

1) Uncertainty models were established in the MUF for the devices used in the VNA calibration
2) Raw measurements (no VNA correction applied) were taken of the devices used for the VNA calibration
3) The identical data was used in both Multical and the MUF to form the error correction matrices for the VNA
4) Starting with the VNA correction turned off, raw measurements were taken of one of the DUTs.
5) Without touching the DUT, the VNA correction from Multical was applied and corrected data of the DUT was taken using the NIST measurement software (a program called MeaslpX was used to take the corrected data from the VNA and another program called Calrep was used to analyze the data taken by MeaslpX)
6) All DUTs were measured by use of the process of 4) and 5)
7) The raw calibration standards data and the raw DUT data were processed through the MUF to arrive at the corrected response for each DUT
8) The corrected MUF responses were compared to the results from the Multical and NIST measurement software process

Throughout this comparison, we tried to keep the two measurement paths as similar as possible. Because of the

differences in the two measurement paths, it was necessary to take both the uncorrected and corrected measurements of the DUTs. The uncertainty models used for the calibration standards will be detailed in Part II of this paper which will be published later. That being said, it is still necessary to have a basic understanding of the uncertainty models used for the Monte-Carlo analysis in the MUF. Figure 1 shows the basic model that was used for the airline standards in the MUF.

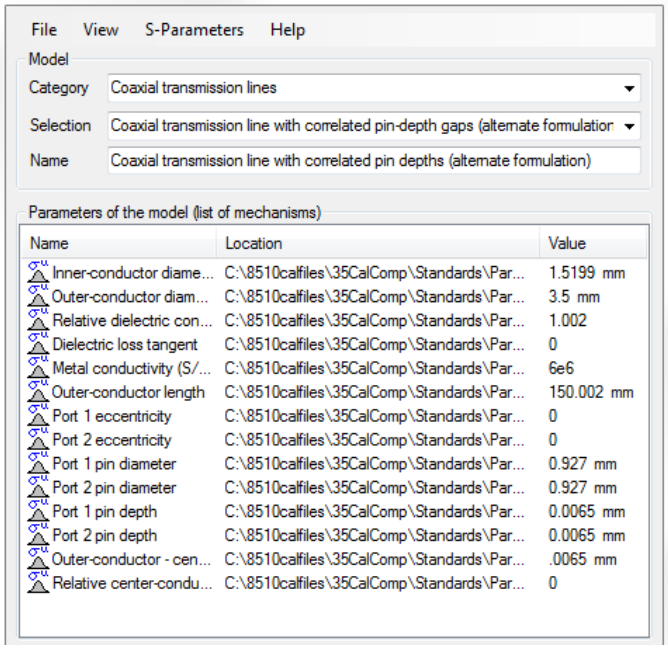

Figure 1. Airline uncertainty model used in the MUF

III. I'VE KICKED THE TIRES - HERE'S HOW THEY FELT

In all, three sets of data are being compared. One from our established technique (notated as Calrep) and two sets from the MUF. One of these sets is the Nominal Value result which is produced when only the base data is used and is not perturbed by any uncertainty components (notated as MUF SA (for Sensitivity Analysis)). The other MUF result is the result from the Monte-Carlo process (MUF MC) that includes a statistical bias introduced in the results (in other words, this is the average value calculated from the results of all of the Monte-Carlo passes) [7].

Figure 2 shows the S_{11} response results from one of the DUTs, a matched termination. There are several items that are noteworthy on the chart. Except at frequencies below approximately 2.5 GHz, there is good agreement between the results from the established technique (Calrep) and the two MUF results (MUF SA and MUF MC). The two MUF responses agree with each other as one would expect. The MUF Monte-Carlo response shows more "raggedness" which is also expected because of the statistical nature on which it is based (100 Monte-Carlo simulations were used). The differences between the various results can be seen in figure 7.

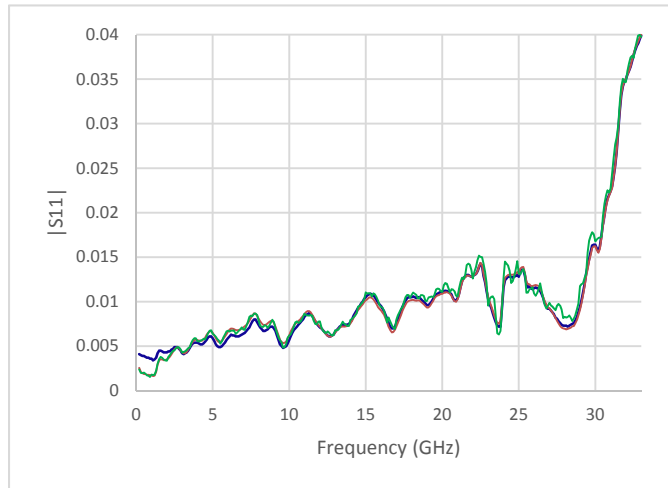

(a)

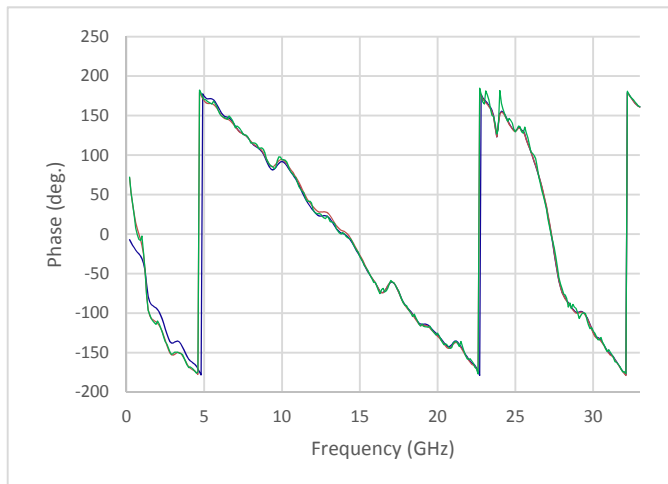

(b)

Figure 2. S_{11} magnitude (a) and phase (b) results for a matched termination. Blue line is the Calrep response, Red is the MUF SA response and Green is the MUF Monte-Carlo response (note the orange and green plots lie virtually on top of each other).

Figure 3 shows the S21 magnitude results for a 50 dB attenuator. Here there is good agreement between all three responses. The statistical variations in the Monte-Carlo result are about the same magnitude as the dynamic range variations.

Figure 4 shows the results from the offset short DUT. Here, 100 Monte-Carlo simulations were used and there is reasonable agreement between the two MUF results. Figure 5 shows the absolute value of the differences between the Calrep and the MUF results with the Calrep uncertainty also shown for the offset short. At the higher frequencies there is good agreement between the Calrep and the MUF results; however, at the

bottom end, about 5 GHz and below, there are discrepancies in the results. Note that there was very good phase agreement between all three approaches (less than 0.3 degrees).

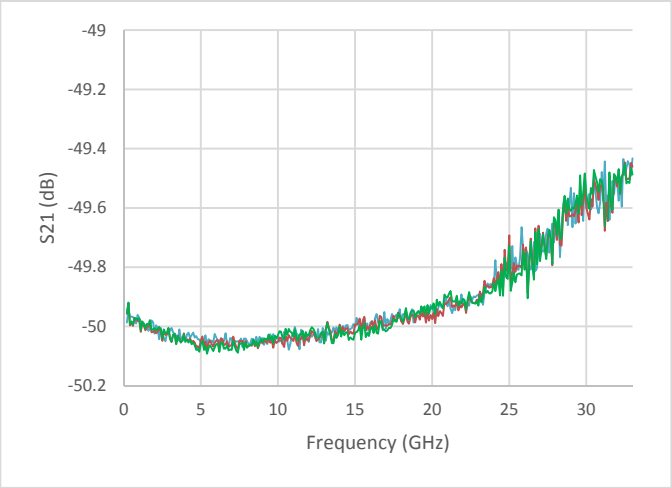

Figure 3. S_{21} magnitude results for a 50 dB attenuator. Blue line is the Calrep response, Red is the MUF SA response and Green is the MUF MC response.

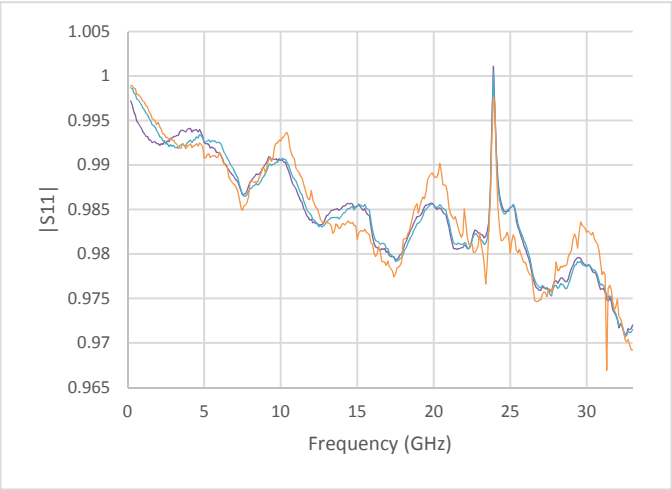

Figure 4. S_{11} magnitude results for an offset short. Blue line is the Calrep response, Orange is the MUF SA response and Green is the MUF MC response.

There are several common treads found from the results. In general, there is good agreement between the different methods used for obtaining the results. Discrepancies are seen at the low frequencies (5 GHz and below), although these differences are fairly small (on the order of 0.002 for S_{11} and on the order of 0.04 dB for S_{21}). This low frequency problem is seen in both reflection and transmission responses, but not seen in all of the DUT responses. The Monte-Carlo response shows more variation than the other responses due mostly to the statistical nature of its derivation.

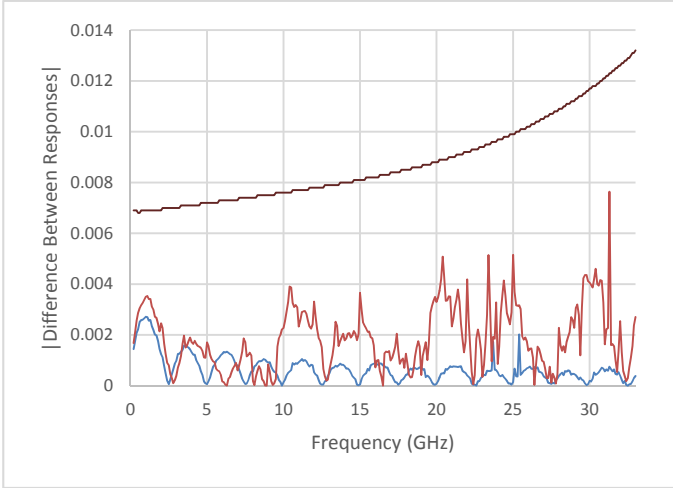

Figure 5. Absolute value of differences in responses for the offset short. Blue is |Calrep – MUF SA| and red is |Calrep – MUF MC|. The brown line represents the typical uncertainty associated with the Calrep measurement.

IV. What have I really learned from kicking the tires

There are several points of discussion coming from the results of the "kick". First, there is generally good agreement between the results from our established technique and the results from the MUF.

Increasing the number of Monte-Carlo iterations from 100 to 1000 does not greatly influence the difference between the Monte-Carlo responses and the unperturbed Nominal Solution from the sensitivity analysis. This can be seen in figure 6 which shows the difference between the nominal unperturbed solution and the Monte-Carlo 100 iteration and 1000 iteration solutions. There is a periodicity to the difference that needs to be investigated further (maybe a Part III?)

As pointed out earlier, there is a difference in the responses at frequencies less than approximately 5 GHz. The difference is between the established technique and both of the MUF results (SA and MC). This is best seen in figure 2a. To investigate this issue, we have taken several steps. The first was to process the exact same DUT raw file through the Multical software and through the MUF (this differs with how we took the Calrep data which was obtained as corrected data through the use of another NIST software package). The results of this can be seen in figure 7. There is essentially no difference between the Calrep results and the results obtained by processing the files through the Multical software. There is the

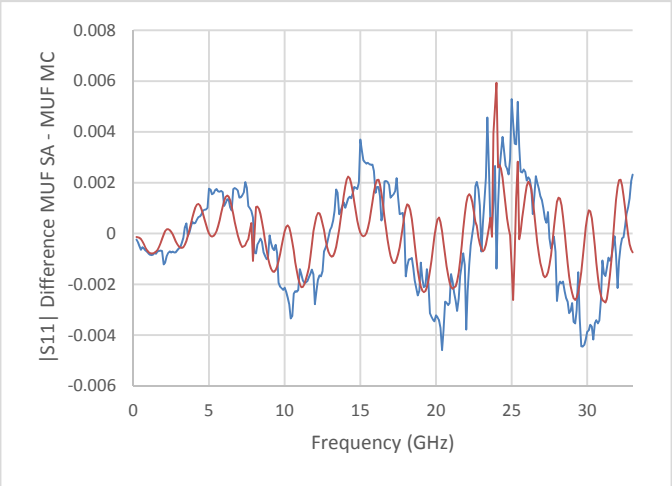

Figure 6. Differences in the Monte-Carlo $|S_{11}|$ responses for the offset short. Blue is (MUF Nominal Solution – MUF Monte-Carlo 100 iterations) and red is (MUF Nominal Solution – MUF MC 1000 iterations).

difference, as seen before, with the MUF results. This indicates that there is a difference in how Multical and the MUF are applying the multi-line calibration technique. The best guess as to a cause for this is the different way that Multical handles moving from an 8 to 12-term solution versus how the MUF uses the 8 and 12-term solutions. Investigation into this is ongoing.

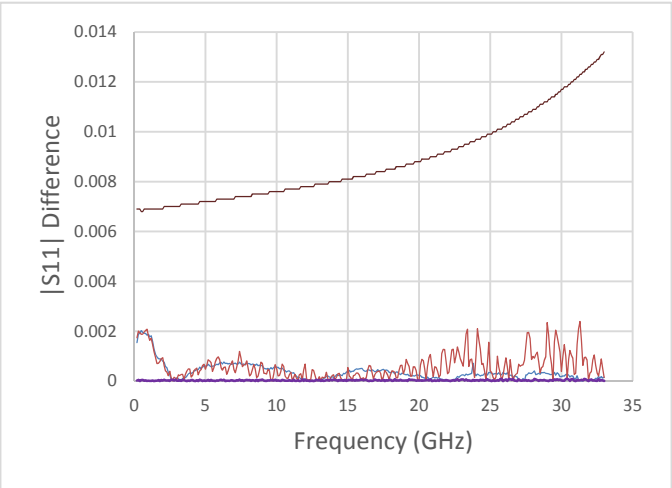

Figure 7. $|S_{11}|$ Differences for the matched termination. Blue is |Calrep - MUF SA|, red is |Calrep – MUF MC|, brown is the Calrep uncertainty (k=2), and purple is |Calrep – Multical| (which is essentially zero).

V. My toe is sore from kicking – what else have I learned

The response results from the NIST Microwave Uncertainty Framework show good agreement with our established method with a few caveats. We are still investigating differences in responses at low frequencies and periodicity issues related to the Monte-Carlo responses.

Stay tuned for Part II or "My Tires Have Air, How Certain am I that they Will Roll?"

References

[1] D. F. Williams, NIST Microwave Uncertainty Framework, Beta Version, http://www.nist.gov/ctl/rf-technology/relatedsoftware.cfm, 2015.

[2] J. A. Jargon, D. F. Williams, T. M. Wallis, D. X. LeGolvan, and P. D. Hale, "Establishing traceability of an electronic calibration unit using the NIST Microwave Uncertainty Framework," *79th ARFTG Microwave Measurement Conference*, Montreal, CANADA, Jun. 2012.

[3] J. A. Jargon, U. Arz, and D. F. Williams, "Characterizing WR-8 waveguide-to-CPW probes using two methods implemented within the NIST Uncertainty Framework," *80th ARFTG Microwave Measurement Conference*, San Diego, CA, Nov. 2012.

[4] J. A. Jargon, D. F. Williams, P. D. Hale, and M. D. Janezic, "Characterizing a noninsertable directional device using the NIST Uncertainty Framework," *83rd ARFTG Microwave Measurement Conference*, Tampa Bay, FL, Jun. 2014.

[5] J. A. Jargon, C. H. Cho, D. F. Williams, and P. D. Hale, "Physical models for 2.4 mm and 3.5 mm coaxial VNA calibration kits developed within the NIST Microwave Uncertainty Framework," *85th ARFTG Microwave Measurement Conference*, Phoenix, AZ, May 2015.

[6] R. B. Marks, "A multiline method of network analyzer calibration," *IEEE Trans. Microwave Theory Tech.*, vol. 39, no. 7, pp. 1205–1215, July 1991.

[7] K.A. Remley, D.F. Williams, P.D. Hale, C.M. Wang, J. Jargon, and Y. Park, "Millimeter-Wave Modulated-Signal and Error-Vector-Magnitude Measurement With Uncertainty," *IEEE Trans. Microwave Theory Tech.*, vol.63, no. 5, pp. 1710-1720, May 2015

Power Level Control of mm-Wave Test Benches for Accurate Small and Large-signal DUT Measurements

C. De Martino, Z. Hu, L. Galatro, G. Sarris and M. Spirito

Electronics Research Laboratory, Delft University of Technology

Mekelweg 4, 2628CD Delft, Netherlands

***Abstract* — In this contribution we describe the accuracy improvement achievable using a vector corrected, power calibrated test-bench when measuring mm-wave non-linear devices. The absence of automatic level control in commercially available network analyzer frequency extenders can result in AM distortion of the transfer characteristic. Moreover, when large-signal mm-wave test-benches are employed (i.e., using multipliers and power meters) the lack of vector correction causes transfer characteristic errors.**

The usage of power levelled mm-wave VNA test-benches allows to properly measure the true small-signal s-parameter response as well as accurately correct for the impedance mismatch present, providing increased correlation between small and large-signal test-benches response.

The accuracy limitation of classical approaches and the improvement achieved by the levelled mm-wave VNA test-bench are validated on a 140GHz power amplifier.

***Index Terms* — Power control, Power calibration, S-parameters measurements, mm-wave, sub-mm-wave.**

I. Introduction

The increasing interests in millimeter-wave (mm-wave) systems for commercial applications, such as automotive and high data rate communication (falling under the umbrella of 5G), is pushing for higher quality mm-wave measurements and device models. Improving the model predictive capabilities is the path to minimize the redesign attempts, thus making the developing phase of a product commercially feasible.

The mm-wave frequency range is characterized by the extensive use of frequency multiplication stages to generate signals. The testing and instrumentation field also makes use of frequency multiplication in the up- and down-converting extension modules of state-of-the-art VNAs. The frequency multiplier chains used in commercial VNA test-set extenders provide a strongly non-linear power relation between the input and output, nevertheless, as it was shown in [1] accurate power control at the mm-wave port is feasible up to the sub-mm-wave frequency range. Despite this, several contributions in the field still suffer from error arising from a non-accurate power level control during scattering parameter measurements, see Fig. 1 a), and errors arising from the simple scalar corrections of large-signal power-meter based setups, see Fig. 1 b).

In this paper we analyze how these errors can be traced to the absence of amplitude power level control of mm-wave VNA extenders, and we describe how the use of full vector correction, using VNA based large-signal setups, allows to achieve an high correlation between the *small-signal* and *large-signal* test-benches response.

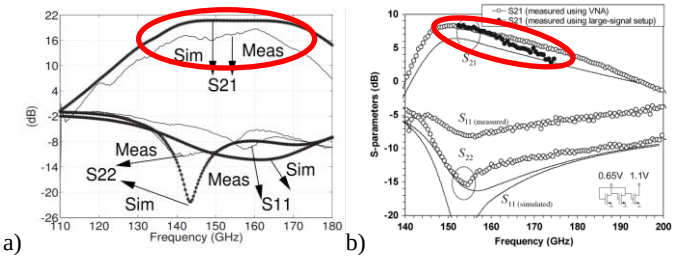

a) b)

Fig. 1: a), Small-signal model-hardware correlation of the PA from [2], b) measured (circles) and simulated (solid lines) S-parameters of the three-stage 150 GHz amplifier, measured with VNA and large-signal setup, from [3].

The paper is organized as follows, first an analysis of the AM distortion in the transfer characteristics of non-linear device excited by non-levelled drive signal is described, together with the limitation of commonly employed scalar mm-wave large-signal setups. Then, the proposed VNA based power controlled small-signal and large-signal test bench of [1] is briefly described. Finally, a 140GHz power amplifier characterization is used as a test vehicle to reproduce some of the shortcomings that can be encountered in mm-wave test-benches and highlight the high correlation between small-signal and large-signal setups when full vector correction is employed.

II. MM-waves Test-Benches Shortcomings

A. Small-signal

The small-signal characterization of power amplifiers, aims to look at input matching, reverse isolation and the small-signal gain. The latter is often evaluated simply looking at the S_{21} at a sufficient back-off level, i.e., the linear region of Fig. 2. When the amplifier is composed by several stages, which is often the case at mm-wave frequencies due to the limited gain per stage, the compression mechanism of the gain curve can be very diverse, from very pronounced to very soft, mostly depending on the area ratios of the stages.

When the absolute power level of the drive signal is unknown and the lower dynamic range, compared to the fundamental VNA operation, advises not to intensively reduce

978-1-5090-4514-3/16/$31.00 ©2016 IEEE

the drive power (i.e., using waveguide attenuators) not to incur in noisy measurement traces, a clear risk of measuring in the weakly non-linear region (Fig. 2) exists. When this occurs the S_{21} parameter is actually modulated by the non-constant drive level (versus frequency) and the non-linear device input-output characteristic. This can result in non-physical fluctuations in the measured S-parameter, as can be observed in Fig. 1 a.

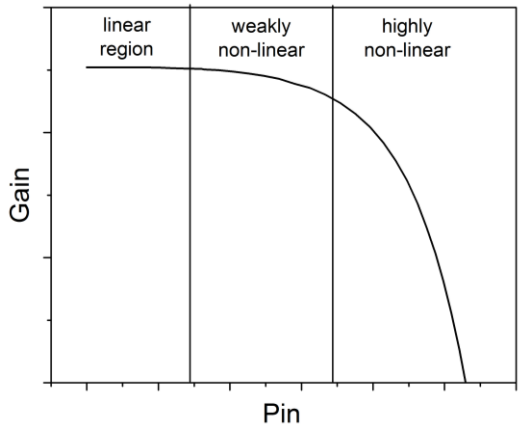

Fig. 2: Gain vs. P_{in} characteristic of a general active device.

B. Large-signal

In order to characterize the key parameters of PAs (i.e., P_{1dB} and PAE), large-signal setup as shown in Fig. 3 are employed. The scalar nature of such setups only allows for a response type of calibration, thus neglecting losses arising from mismatches in the setup.

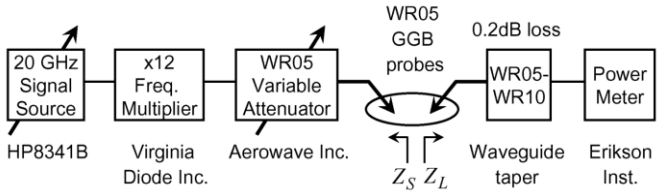

Fig. 3: G-band large-signal measurement setup (153 GHz to 173 GHz), from [3].

It is important to note that all the components shown in Fig. 3 are already part of a VNA with frequency extenders, with the only exception that stand alone frequency multipliers could generate few dBs more of power due to the absence of the directional coupler.

III. System Architecture and Calibration Procedure

The block scheme of the VNA based power controlled small- and large-signal setup, using vector correction, presented in [1] is shown in Fig. 4. The system features a calorimeter based power meter, required for power calibration. All the data manipulation, including calibration and power control, are performed using a user friendly GUI interface which runs on an external computing unit.

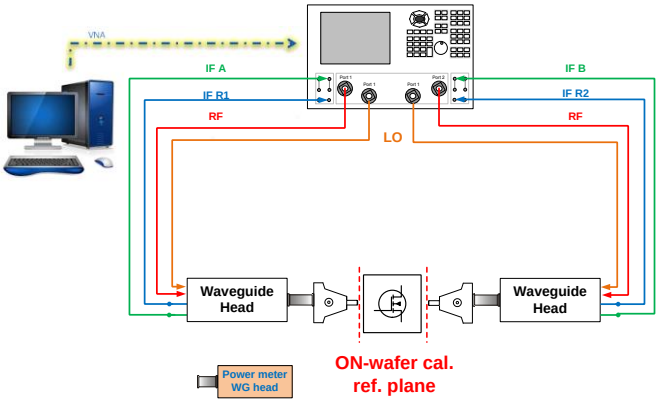

Fig. 4: Simplified scheme block of the employed measurement setup.

The calibration procedure consists of four steps:

1. two-port calibration is performed at the waveguide interface of the extenders (i.e. TRL calibration [4]);
2. power calibration [5] is performed at the input waveguide port, providing knowledge of the absolute power at the mm-wave port of the extender modules;
3. a power leveling procedure is carried out, enabling accurate power control at the waveguide ports;
4. finally, an on-wafer two-ports calibration is performed (i.e. TRL) in order to shift the calibration reference planes from the waveguide ports to the wafer probe tips.

After completing the calibration steps described above, the system is capable to perform power controlled S-parameter measurements as well as large-signal measurement.

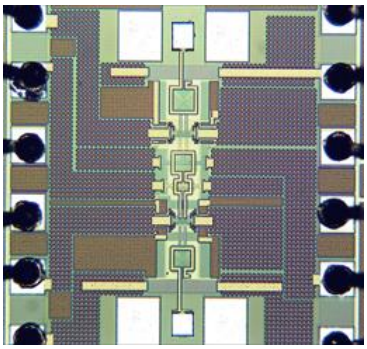

Fig. 5: Chip micrograph of the measured power amplifier.

IV. Power Controlled Vector Corrected S-Parameter Measurements

To demonstrate the capability of the VNA based power controlled setup, measurements of a multi-stage power amplifier, were conducted in the frequency range from 130 to 180 GHz. Two VDI extender modules were employed for the measurements, and a VDI Erickson PM5 power meter, was employed for the power calibration. A micrograph of the measured amplifier is shown in Fig. 5. First, the DUT was measured, for a defined bias level, using the classic mm-wave

VNA setup (i.e., without power control). Then, measurements were performed at a fixed, controlled power level of $P_{av,in}$ = -30 dBm. Finally, power sweeps in the range from -43 dBm to -12 dBm, at different frequencies, have been employed to realize large-signal measurement of the device.

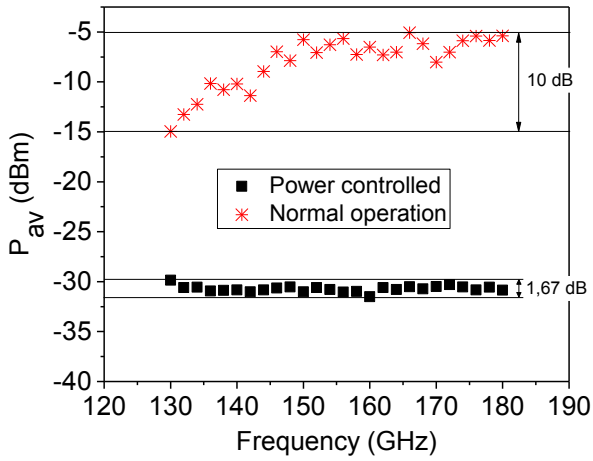

Fig. 6: Power available versus frequency at port 1 of the employed system for normal operation (red asterisks) and using power control (black squares).

A. *Power controlled S-parameters*

Fig. 6 shows the measured available power from port 1 of the WR5 extender in the conventional operation mode, i.e., no power level, (red asterisks) and for power controlled measurements (black filled squares). While the non-controlled available power presents a variation higher than 10 dB across the entire frequency range, the power control guarantees power fluctuations lower than 2 dB in the same frequency range.

Fig. 7 shows the measurement results for the S_{21} of the considered amplifier in the entire frequency range. Measurements highlight a strong discrepancy between the two methods in the frequency range (solid line and dashed line) from 130 to 157 GHz (see, Fig. 7 section A), where the difference in terms of S_{21} reaches 10 dB at 140 GHz. This discrepancy can be better explained when looking at the large-signal measurements. Fig. 8 shows the transducer gain (G_T) of the device under test, versus P_{av}, for 140 GHz (black filled squares) and 170 GHz (red asterisks). At 140 GHz, the power level employed for the S-parameter measurements (circa -10 dBm) is not sufficiently low to operate the DUT in the linear region, see Fig. 2. This means that the S-parameters cannot be correctly measured and a variation in input power would result in a modulation of the measured S-parameter. When the measurement is performed at P_{av} = -30 dBm with the power controlled system, the device is operating in the linear region, so that the S-parameter measurements do not depend upon the input power, as it should be. These results show how the capability to fine control the power level during active device measurement allows to prevent incorrect drive to the device, which could lead to inaccurate measurements.

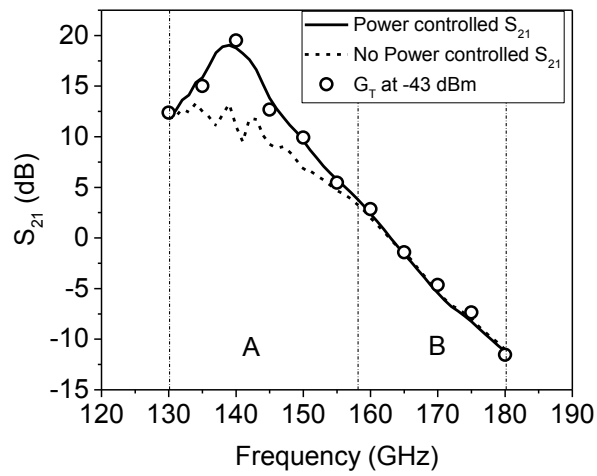

Fig. 7: S_{21} of the considered PA measured in normal system operation (dashed line), with -30 dB controlled P_{av} (solid line) and G_T obtained using the large-signal measurements at -43 dBm.

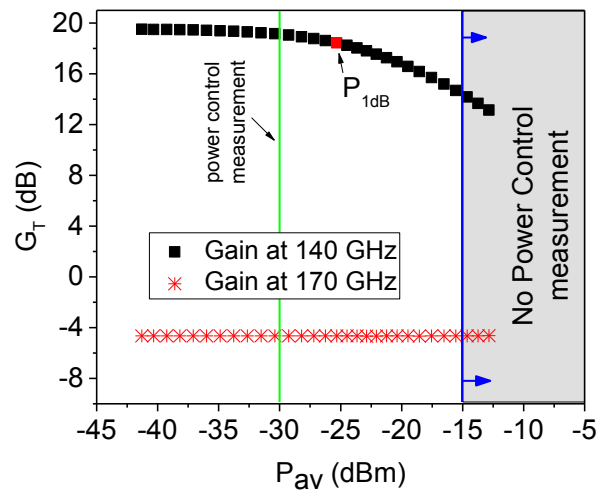

Fig. 8: G_T of the measured PA, obtained using large-signal measurements at 140 GHz (black squares) and 170 GHz (red asterisks). In Gray is shown the range of P_{av} levels where no power control is performed.

B. *Vector corrected large signal measurements*

As explained in Section II, one of the main challenges associated to the use of conventional mm-wave large-signal measurement setups, like the one depicted in Fig. 3, lies in the usage of a simple scalar/response correction, providing different results between small-signal and large-signal test-benches even when the same power level is applied.

The use of a full vector calibration in combination with power measurements, as it is described in section II, allows always having comparable results, both during power controlled S-parameter measurements and large-signal measurements. In order to verify this principle, an experiment was conducted using large-signal measurements of the device. If these measurements are adequately vector corrected, G_T extracted a low power (i.e., in linear regime) should be equal

to the S_{21} parameter measured using power controlled frequency sweep.

In Fig. 7 the S_{21} predicted by using G_T measurement at a power P_{av} = -43 dBm is shown (empty circle) as compared to power control S-parameters measurement (solid line). As predicted, the two curves (solid line and the circles) closely track each other, highlighting how the vector correction is correctly applied also to large-signal measurements.

V. Conclusions

In this paper, the advantages of using power control for mm-wave active device characterization is presented. The proposed method allows to properly control the power level during S-parameter measurements. This allows to always guarantee small-signal operation, preventing incorrect measurement results that may occur when large input power fluctuation can drive the device in large-signal regime. Also, the combination of S-parameter and power calibration allows performing vector corrected large-signal characterization at mm-wave, as it was not possible with conventional scalar large-signal mm-wave test-benches.

VI. Acknowledgments

This research is supported by the Dutch Technology Foundation STW (project 13325), which is part of the Netherlands Organization for Scientific Research (NWO), and which is partly funded by the Ministry of Economic Affairs.

References

[1] L. Galatro, S. Galbano, A. Santaniello and M. Spirito, "Power control for S-parameters and large-signal characterization at (sub)-mmWave frequencies," *Microwave Measurement Conference (ARFTG), 2015 85th*, Phoenix, AZ, 2015, pp. 1-4.

[2] N. Sarmah, B. Heinemann and U. R. Pfeiffer, "A 135–170 GHz power amplifier in an advanced sige HBT technology," *2013 IEEE Radio Frequency Integrated Circuits Symposium (RFIC)*, Seattle, WA, 2013, pp. 287-290.

[3] M. Seo, B. Jagannathan, J. Pekarik and M. J. W. Rodwell, "A 150 GHz Amplifier With 8 dB Gain and 6 dBm in Digital 65 nm CMOS Using Dummy-Prefilled Microstrip Lines," *IEEE Journal of Solid-State Circuits*, vol. 44, no. 12, pp. 3410-3421, Dec. 2009.

[4] G. F. Engen and C. A. Hoer, "Thru-Reflect-Line: An Improved Technique for Calibrating the Dual Six-Port Automatic Network Analyzer," *IEEE Transactions on Microwave Theory and Techniques*, vol. 27, no. 12, pp. 987-993, Dec 1979.

[5] A. Ferrero and U. Pisani, "An improved calibration technique for on-wafer large-signal transistor characterization," *IEEE Transactions on Instrumentation and Measurement*, vol. 42, no. 2, pp. 360-364, Apr 1993.

Spectral Characterization of Linear Isotropic and Anisotropic Dielectric Materials Using Terahertz Measurement Systems

Jeffrey Seligman[1], Christopher Walker[1], Ben Sternberg[1], and Christopher Green[2],

[1]University of Arizona, Tucson, AZ, [2]Rogers Corporation, Advanced Connectivity Solutions, Chandler, AZ

***Abstract* — In this study, quasi-optical techniques are used to evaluate the properties of dielectric substrates at millimeter wave frequencies. Anisotropy with respect to wave polarization was observed in the composite materials using several instruments including the FTS, TDS, and THz VNA. The measurements were carried out from 200 GHz to 3000 GHz (3 THz) depending on the instrument. Material loss deviated significantly above 500 GHz. Uniform plastics such as H/LDPE polyethylene were well behaved by comparison.**

***Index Terms* — Dielectric material characterization, measurements, loss tangent, Fourier transforms, time domain, anisotropic, nondestructive testing, terahertz.**

I. Introduction

The performance of modern electronic components is now being limited by the materials from which they are made rather than by their circuit design. Hence, there has been an increased emphasis on the development and characterization of high performance dielectrics which require novel broadband instrumentation and extraction techniques, from which models can be formulated. This information results in improved packaging and component designs. Several different types of thin (5-125 mils) dielectric sheets were characterized at terahertz (THz) frequencies using quasi-optical, nondestructive evaluation techniques (NDE) [1]. Composite substrates, polyethylene plastics, and PolyJet™ 3-D (Stratasys, Inc.) printing polymers were tested. Free space (Quasi-optical) methodology eliminates all conductors, as compared to the IPC-TM-650 test methods that require stripline conductors. Therefore, these results depend only on the dielectric properties of the test sample, its thickness, and the surrounding environment, plus the test setup. A precision test fixture was developed to accomplish these measurements. It was also able maintain calibration during sample changes.

The test systems reported on included a Fourier Transform Spectrometer (FTS/FTSIR), a Time Domain Spectrometer (TDS) and a THz Vector Network Analyzer (VNA). Using these instruments, the submillimeter spectral characteristics (i.e., dielectric constant and loss tangent) of the samples was obtained. Wave polarization anisotropy was observed in some of the composite materials. The TDS was the most flexible instrument for vector dielectric characterization followed by the VNA, which operates at a lower frequency range. The FTS (scalar) offered the highest frequency of operation (> 3 THz). All calibration was done using a modified SOLT free space technique and the dielectric measurements were made in the transmission mode. The extraction process for the TDS used the Debye model [2] combined with an iterative process [3]. The VNA analysis used s-parameters and a predictive averaging process.

Some applications of these techniques include:

1) Characterization of IC dielectric packaging materials including nano-dielectrics, structured dielectrics, explosives, carbon nanotubes, and thickness determination [4].
2) THz imaging, which can be used for security scanning applications, geological soil and surface depth analysis, and forensics.
3) Biomedical applications including cell irregularity and pill coating analysis (Teraview Ltd., Cambridge, UK).

II. Equipment and Experiment Description

The specific measurement systems used in this project included a Beckman Fourier Transform Spectrometer (FS-720, RIIC, circa 1976, Figure 3), a Picometrix T-Ray 4000 Time Domain Spectrometer (Figure 4), a terahertz Vector Network Analyzer (Virginia Diodes Extender plus a Rohde-Schwarz ZVA40 Vector Analyzer, Figure 5), and a VDI scalar sub-millimeter wave analyzer system (200-850 GHz).

III. DISCUSSION

Below 500 GHz, the parameter results compared favorably with lower frequency IPC TM-650 methods. Above 500 GHz, the data showed significant deviations on all test platforms. This is probably due to internal scattering and absorption [Hejase:1]. The plastic samples tested were isotropic, while the composites had polarization based anisotropic effects. Plastics are not mechanically suitable for packaging or substrates because they are unstable with respect to temperature, humidity, and thickness variation. However, they have well behaved loss characteristics and served as a basis for parameter comparison. Figures 6 and 7 show a difference in dielectric values on a composite material when irradiated by a polarized wave. When the sample was rotated 90 degrees, anisotropic effects were visible at THz, but this effect is generally not observable at 10 GHz, a standard IPC test frequency.

The tables (Fig 1-2) show the comparisons between the different systems. The FTS results are scalar and relative; however, more data can be obtained by using pairs of samples

978-1-5090-4514-3/16/$31.00 ©2016 IEEE

325-500 GHz Measured PSU and 500-750 GHz at Virginia Diodes using VNA / ZVA 40									
Frequency Range (GHz)	Sample Description	ε_r' (Dk mfgr) @10GHz	Loss Tan (Df mfgr) @10GHz)	ε_r' Min Over Freq Range (H,V)	ε_r' Max Over Freq Range (H,V)	ε_r' Avg Over Freq Range (H,V)	Loss Tan Min Over Freq Range (H,V)	Loss Tan Max Over Freq Range (H,V)	Loss Tan Avg Over Freq Range (H,V)
325 - 500	RO3003™, 20mils	3.00	0.002	---, 2.84	---, 3.05	---, 2.94	---, 0.0042	---, 0.0043	---, 0.0043
500 - 750	RO3003™, 10mils	3.00	0.002	2.66, 2.71	3.32, 3.38	3.07, 3.10	0.0018, 0.0055	0.0019, 0.0066	0.0019, 0.0062
325 - 500	RO3006™, 25mils	6.15	0.003	6.65, 7.04	7.46, 7.92	7.14, 7.53	0.0143, 0.0138	0.0193, 0.0187	0.0172, 0.0166
500 - 750	RO3006™, 25mils	6.15	0.003	7.17, 7.50	7.93, 8.36	7.61, 8.00	0.0077, 0.0118	0.0729, 0.0757	0.0446, 0.0480
500 - 750	RO3010™, 10mils	10.2	0.0035	11.28, 11.15	14.06, 13.32	13.19, 12.40	0.0078, 0.0053	0.0113, 0.0122	0.0098, 0.0092
325 - 500	RO4350B™, 60mils	3.66	0.0060	3.65, 3.68	3.80, 3.86	3.75, 3.78	0.0099, 0.0152	0.0173, 0.0247	0.0141, 0.0206
500 - 750	RO4350B™, 60mils	3.66	0.0060	3.67, 3.69	3.83, 3.95	3.75, 3.76	0.0184, 0.0268	00347, 0.0403	0.0276, 0.0345
325 - 500	RO5870™, 31mils	2.33	0.0015	2.38, 2.37	2.52, 2.50	2.45, 2.43	0.0038, 0.0038	0.0039, 0.0039	0.0038, 0.0038
325 - 500	RO6002®, 30mils	2.94	0.0017	2.84, 2.83	3.06, 3.03	2.94, 2.93	0.0012, 0.0012	0.0014, 0.0014	0.0013, 0.0013
500 - 750	RO6002®, 30mils	2.94	0.0017	---, 2.83	---, 3.06	---, 2.97	---, 0.0011	---, 0.0045	---, 0.0030
325 - 500	TMM®10, 25mils	9.20	0.0031	9.39, 9.73	10.42, 10.69	9.92, 10.26	0.0060, 0.0120	0.0111, 0.0174	0.0089, 0.0151
500 - 750	TMM®10, 50mils	9.20	0.0031	10.82, 9.87	11.21, 10.52	11.06, 10.27	0.0081, 0.0054	0.0120, 0.0116	0.0103, 0.0089

Materials Measured 5/31-6/2/2012 at Portland State University Picometrix T-Ray 4000 Time Domain Spectrometer OFFSET=680pS, Tavg=6000									
Frequency Range (GHz)	Sample Description	ε_r' (Dk mfgr) @10GHz	Loss Tan (Df mfgr) @10GHz)	ε_r' Min Over Freq Range (H,V)	ε_r' Max Over Freq Range (H,V)	ε_r' Avg Over Freq Range (H,V)	Loss Tan Min Over Freq Range (H,V)	Loss Tan Max Over Freq Range (H,V)	Loss Tan Avg Over Freq Range (H,V)
200 - 1600	RO3003™, 20mils	3.00	0.002	3.0, 3.05	3.0, 3.12	2.9, 3.06	0.01, 0.01	0.056, 0.065	0.02, 0.03
200 - 1600	RO3006™, 25mils	6.15	0.003	6.9, 6.9	7.6, 8.2	7.4, 7.8	0.025, 0.025	0.022, 0.03	0.015, 0.020
200 - 1600	RO4350B™, 60 mils	3.66	0.0060	3.65, 3.70	3.8, 3.76	3.73, 3.73	0.03, 0.02	0.065, 0.07	0.045, 0.04
200 - 1600	RO5870™, 31mils	2.33	0.0015	2.43, 2.375	2.45, 2.475	2.44, 2.46	0.01, 0.05	0.035, 0.12	0.025, 0.07
200 - 1600	RO6002®, 30mils	2.94	0.0017	2.90, 2.90	2.95, 2.95	2.93, 2.93	0.008, 0.008	0.028, 0.027	0.013, 0.013
200 - 1600	TMM®10, 15mils	9.20	0.0031	10.25, 10.8	10.8, 11.4	10.6, 11.2	0.015, 0.015	0.032, 0.043	0.022, 0.025
200 - 1600	HDPE_K17_dull	2.25-2.35	0.0003	2.49, 2.47	2.48, 2.46	2.485, 2.465	0.012, 0.005	0.025, 0.010	0.013, 0.007
200 - 1600	LDPE_K112_0125	2.25-2.35	0.0003	2.282, 2.282	2.286, 2.286	2.284, 2.284	0.001, 0.001	0.0045, 0.0045	0.0015, 0.0015

Fig 1 (a,b) VNA and TDS Permittivity and Loss Tangent Data (H, Horizontal=0 deg & V, Vertical=90 deg relative polarization)

FTS Data Summary Using The University of Arizona Astronomy Beckman FS720 Spectrometer					
Sample Description	ε_r' (Dk mfgr) @10GHz[2]	Loss Tan (Df mfgr) @10GHz)[2]	Average Relative Level	Voltage Scale[3] (mV)	Overall Relative Avg (mV)
RO3003™, 10mils	3.00	0.002	0.70	18.00	12.60
RO3003™, 20mils	3.00	0.002	0.80	13.00	10.40
RO4350B™, 10mils	3.66	0.0060	1.00	9.00	9.00
RO4350B™, 20mils	3.66	0.0060	0.50	12.30	6.15
RO6002®, 20mils	2.94	0.0017	0.75	24.80	18.60
RO6002®, 30mils	2.94	0.0017	1.00	28.20	28.20
TMM®10, 25mils	9.20	0.0031	5.00	1.18[1]	5.90
TMM®10, 50mils	9.20	0.0031	3.00	1.58[1]	4.70

Notes:

(1) 1.1 mil Beam Splitter/Filter used for TMM®10 Measurement (SF=3.5)

(2) Rogers Corp. Loss Tangent @10 GHz per method IPC TM-650-2.5.5.5C

(3) 7.4 mil Beam Splitter/Filter used for TMM®10 Measurement (SF = 3.5)

TMM®10 is a ceramic, hydrocarbon, termose polymer composite resin

RO4350B™ is a woven glass reinforced hydrocarbon/ceramic

RO6002™ is a RT/Duroid® Laminate

RO3003™ is a ceramic-filled PTFE composite, high freq circuit material

Fig. 2 FTS Relative Transmission Loss Data

with different thicknesses and then solving both Beer equations [5]. This method relies on the requirement that each sample comes from the same manufacturing lot.

The TDS appeared to be the most useful instrument for free space spectral material measurements. It relies on amplitude loss and time delay (phase) directly, using a very narrow pulse, rather than swept s-parameters. Since the TDS is pulsed, it does not see some types of reflection. A TDS system is coherent [X-C Chang:5], vector based, wideband (but less than an FTS), and it has high dynamic range. It is easy to calibrate, very stable, makes rapid measurements with integrated averaging, and it does not require a vacuum chamber. Since it is coherent, it is ideal for observing polarization based anisotropy and 3-D material defects. Its sensor heads can be moved to scan at different angles. It exposes material defects and inhomogeneity that is not always visible on the VNA. On the other hand, the VNA can see narrow band effects. Both the VNA and TDS are limited by their source power and detector sensitivity, and both instruments can perform transmission and reflective measurements. All these methodologies are limited by the ability to measure thickness exactly, which is needed in the extraction process to determine time delay. Surface averaging was used to minimize this error.

The THz VNA systems consisted of a lower frequency VNA (40GHz/ZVA™) which was preceded by a VDI THz Extender unit. Two bands of operation were used, 325-500 GHz (at PSU) and 500-750 GHz (at VDI). A VNA is a linear, coherent vector system and the data is extracted in the form of s-parameters. The latest generation of VNA's (PNA™) use X-Parameters™ and can handle non-linear devices.

An FTS/IR has a wider bandwidth, higher frequency of

operation, and the Multiplex Advantage, but it uses an incoherent arc lamp source and is therefore a scalar system. FTS polarization effects would therefore require a filter or a Wollaston Prism thus adding loss and calibration error. The FS-720 system was evacuated and it used a cooled IR Labs bolometer detector. The data from this system showed relative sample loss that correlated well with manufacturer specifications. (See Figures 6 & 7, esp. RO4350B)

IV. Conclusion

Several quasi-optical THz systems were used for these measurements and the results were consistent across the different platforms. The study demonstrated anisotropic and isotropic behavior of several dielectric substrates commonly used in component and package designs. Polyethylene samples were used as a control group. The most revealing results were obtained with the TDS, followed next by the VNA. Both these systems use coherent sources producing vector data. These experiments demonstrated that THz instrumentation could be used to characterize dielectric substrates and show subtle imperfections. The project emphasis was on experimental implementation rather than computational techniques.

Acknowledgement

The FTS measurements were performed at the University of Arizona, the TDS and VNA measurements were done at the NEAR Lab at Portland State University (Dr. Zurk, director, along with Gabe Kniffin and Sam Henry), and at Virginia Diodes, Inc, with CTO Jeff Hesler's assistance. Funding was provided by a DURIP grant partnered with Raytheon Missile Systems. Rogers Corporation provided the composite samples along with Dr. Al Horn's technical support. The fixture was designed and fabricated with the resources at Universal Cryogenics and the UA machine shop. The cryogenic Bolometer detector system and operational data used for the FTS were provided by Infrared Laboratories, Tucson, AZ. The samples were prepared at the University of Arizona and Prototron, Inc., Tucson, AZ. The U of A project staff included Chris Walker, Ben Sternberg, Bill Peters, and Abe Young, who all provided much appreciated guidance. Jeff Harman, HCI, Inc. upgraded the servo in the FTS and Chris Green helped with the VNA techniques and documentation support.

References

[1] J.A Hejase, P.R Paladhi,.; P. Chahal, "Terahertz Characterization of Dielectric Substrates for Component Design and Nondestructive Evaluation of Packages," in *Components, Packaging and Manufacturing Technology, IEEE Transactions on* , vol.1, no.11, pp.1685-1694, Nov. 2011

[2] Peter J. W. Debye, *Polar Molecules*. New York: Dover, 1929.

[3] Timothy D. Dorney, Richard G. Baraniuk, and Daniel M. Mittleman, "Material Parameter Estimation with Terahertz Time-Domain Spectroscopy," *Journal of the Optical Society of America,* A 18.7 (2001): 1562–1571, 20 Aug. 2012.

[4] Dunaevskn, G.E.; Suslyaev, V.I.; Zhuravlev, V.A.; Badin, A.V.; Dorozhkin, K.V.; Kanygin, M.A.; Sedelmkova, O.V.; Bulusheva, L.G.; Okotrub, A.V., "Electromagnetic response of anisotropic polystyrene composite materials containing oriented multiwall carbon nanotubes," in *Infrared, Millimeter, and Terahertz waves (IRMMW-THz), 2014 39th International Conference on* , vol., no., pp.1-2, 14-19 Sept. 2014

[5] Chan, George C.-Y., and WingTat Chan. "Beer's Law Measurements Using Non-Monochromatic Light Sources—A Computer Simulation." *Journal of Chemical Education 78.9 (2001): 1285*. ACS Publications. Web. 5 Dec. 2014

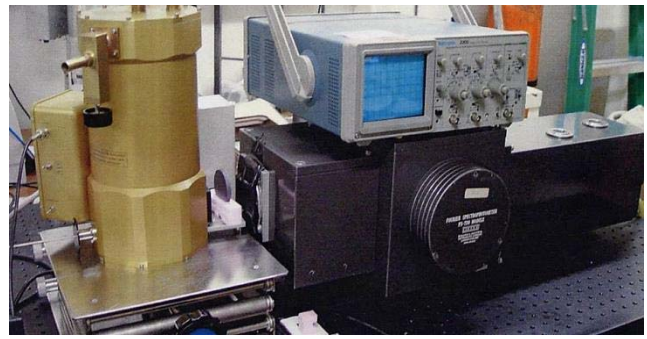

Fig. 3 Fourier Transform Spectrometer (Interferometer) including detector and associated test equipment. Two Vacuum pumps and a lock-in amplifier were also required.

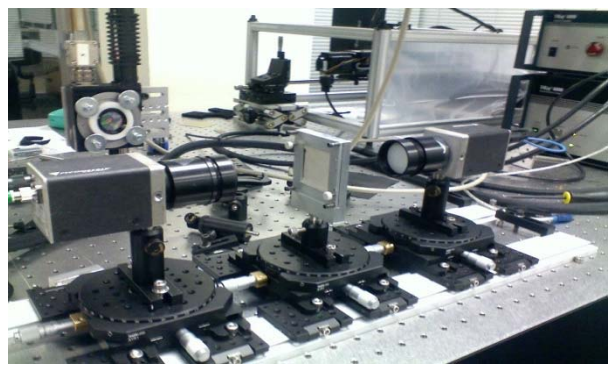

Fig. 4 Picometrix T-Ray 4000 TDS(NEAR Lab at PSU) showing the precision stage, the test fixture, and sample, suspended between the coherent source and an Auston switch detector.

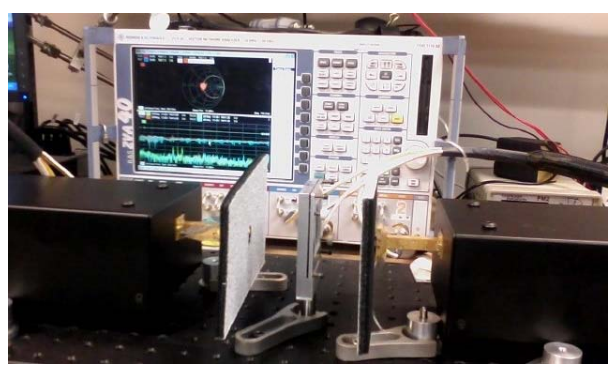

Fig. 5 THz VNA setup at Virginia Diodes, showing ZVA Analyzer, VDI THz Extenders, sample/fixture, waveguide, and absorber (500-750 GHz).

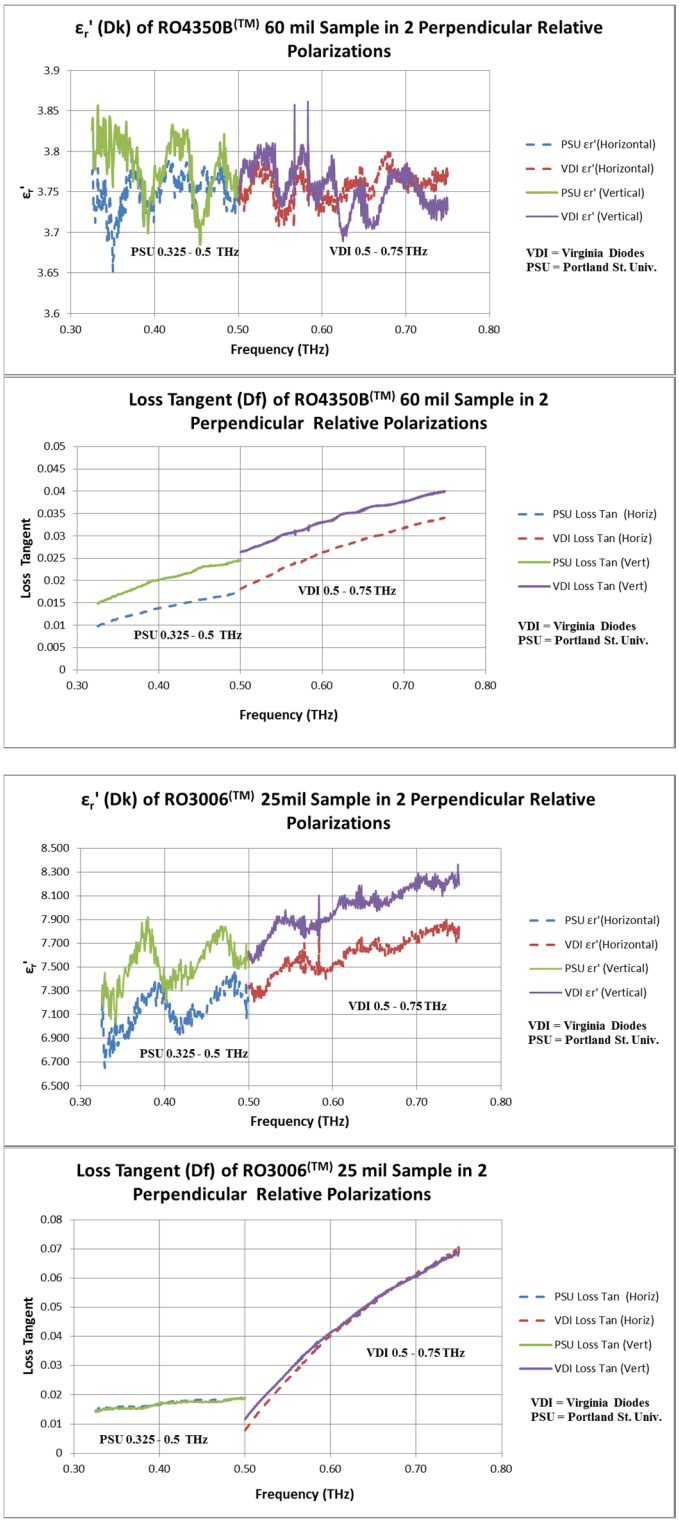

Fig. 6 (a-d) VNA Data for RO4350B™ 60mils and RO3006™ 25mils

These figures show the similarity between the results of the TDS and VNA methods. Note the wider frequency range of the TDS. The higher loss at THz frequencies is expected.

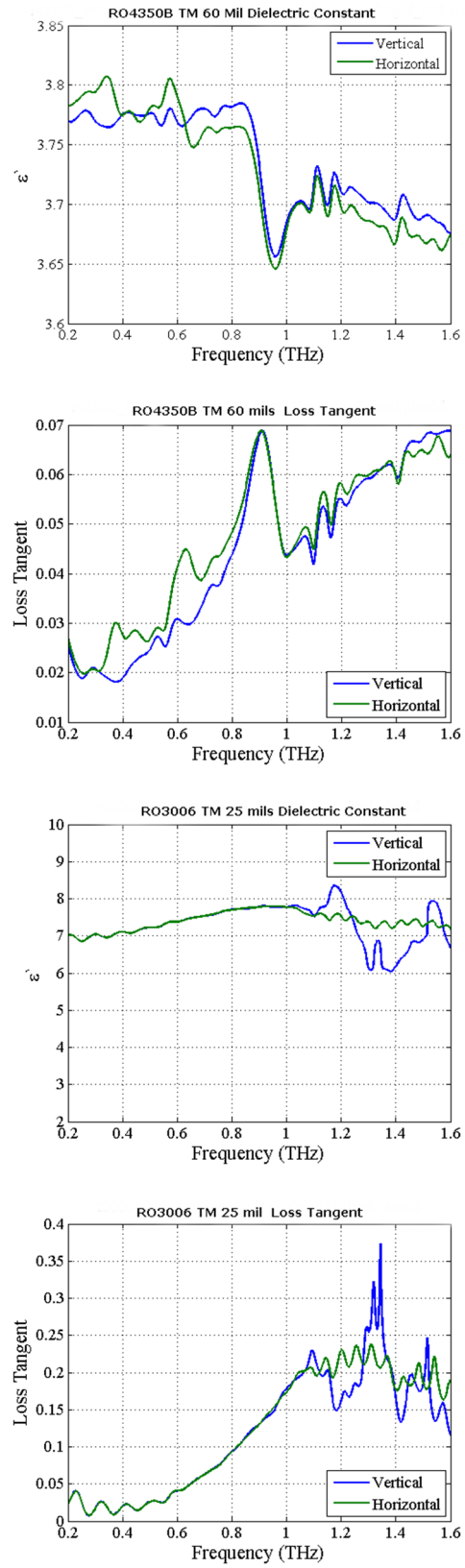

Fig. 7 (a-d) TDS Data for R4350B 60 mils and R3006 25 mils

Performance Evaluations of Dielectric Waveguide for Millimeter-wave On-Wafer Measurements

Masahiro Horibe[1], Ryo Sakamaki[1], and Yuto kato[1]

[1]Research Institute of Physical Measurements, National Metrology Institute of Japan, National Institute of Advanced Industrial Science and Technology, Tsukuba, Japan

***Abstract* — We have developed flexible circular dielectric waveguide for millimeter-wave and terahertz frequency applications. In the millimeter and terahertz frequency range, over 70 GHz, metallic waveguide transmission line is generally used. However, it is hard to build-up the system due to no-flexibility of metallic waveguide lines. High density polytetrafluoroethylene, i.e. PTFE, is used for developed dielectric waveguide lines. The PTFE has dielectric permittivity constant of approximately 2.0 with low loss, tanδ < 10^{-4}. In the developed dielectric waveguide, the electromagnetic wave can transmit with single mode over 60 GHz and multimode over 90 GHz. The proposed dielectric waveguide has also demonstrated the on-wafer measurements for verification devices compared to on-wafer measurement built up by conventional 1.0 mm coaxial cable system. As the comparison results, the proposed dielectric waveguide can potentially be applied to on-wafer measurement at millimeter-wave frequency and above.**

***Index Terms* — Dielectric circular waveguide, millimeter-wave, Terahertz, PTFE, Flexible, on-wafer measurement, verification.**

I. Introduction

Recent years, millimeter wave electromagnetic technology is widely used in the industrial application, i.e. automotive radar, data transfer, WiGig, etc., and mobile telecommunications. In the research and development, waveguide must be used in measurement system and application system at millimeter wave frequency. Metallic waveguides have low loss, but it's rigid, and then, limited flexibility in on-wafer measurement system setup. We propose new concept of flexible dielectric waveguide used in the on-wafer measurement at millimeter-wave frequency and above.

The dielectric waveguide structure is circular geometry [1] to provide low loss and flexibility of waveguide transmission lines. In the concept of dielectric waveguide, transmission line transmits single and higher order mode electromagnetic wave signal, then transmitted signal convert to single mode for each frequency band at waveguide converters to connect to VNA.

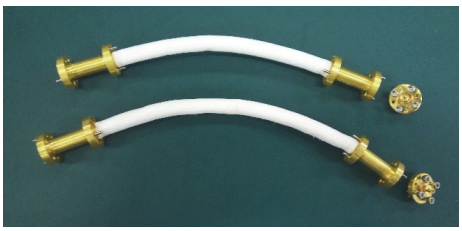

Fig.1. Dielectric waveguide used for measurement system, assembled for WR-10 waveguide bands, together with 1.0 mm coaxial connector converters.

Finally, verification devices were evaluated to compare the measurement performances of the both on-wafer measurement built of the dielectric waveguide system and 1.0 mm coaxial cable system at millimeter-wave frequency band, i.e. 65 GHz to 110 GHz.

II. Design and Performance Evaluation

Polytetrafluoroethylene, PTFE, was adopted to dielectric transmission line. And the diameter of the dielectric circular waveguide was approximately 3.0 mm. Dielectric waveguide was covered by low density PTFE with outer diameter of 15 mm. At the both ends of dielectric waveguide, waveguide converter was attached to convert from circular waveguide to rectangular waveguide [2] with WR-10 waveguide frequency band (Fig. 1).

In the paper, we measured scattering parameter from 75 GHz to 110 GHz by using WR-10 waveguide frequency extension modules. First, VNA was calibrated by Thru-Reflect-Line method in advance. Dielectric circular waveguide was connected and its S-parameter was measured for straight dielectric waveguide with 700 mm long (Fig.2(a)). Furthermore, S-parameter for conventional metallic waveguide (L=50 mm) and 1.0 mm coaxial cable (L=160 mm) were also measured.

Return loss measurement results for dielectric waveguide are shown in Figure 2(a) together with return loss of metallic waveguide and 1.0 mm coaxial cable. Generally, return loss of dielectric waveguide reaches less than -20 dB. The value is almost comparable to that of metallic waveguide coaxial cable in WR-10 waveguide band.

Insertion loss per unit length of dielectric waveguide, drawn by red line in Fig.2(c), was somewhat lossy compared to insertion loss per unit length of metallic waveguide. However, it is better than that of 1.0 mm coaxial cable.

III. On-wafer Measurement for Comparison

A. Measurement Setup

A SUMMIT 12000 probe station with infinity 150-pitch GSG probes and impedance standard substrate (ISS) 101-190 produced by Cascade Microtech Inc. were used for the performance comparison the both on-wafer measurement

978-1-5090-4514-3/16/$31.00 ©2016 IEEE

TABLE I

SYSTEM CONFIGURATION OF ON-WAFER MEASUREMENTS

	1.0 mm coaxial system	**Dielectric waveguide system**
Line configuration	GORE®PHASEFLEX® (*L*=160 mm) 1.0 mm(male) to 1.0 mm(male)	Circular dielectric waveguide (*L*=200 mm) 1.0 mm to WR-10 and WR10 to circular waveguide converters
Frequency Extension Module	N5250A	V10VNA2-T/R 75 GHz-110 GHz
VNA	E8361A	
Probe	· Infinity SP-I110+A-GSG-06 (1.0 mm coaxial connector, 150pitch)	
ISS / calibration method	· 101-190 / Line-Reflect-Reflect-Line (LRRM)	
Measurement frequency range / points	10 MHz to 110 GHz (201 points)	65 GHz to 114 GHz (201 points)
Verification devices	· Short circuits, matched load devices and mismatched line (contact skating: 20um)	

(a)

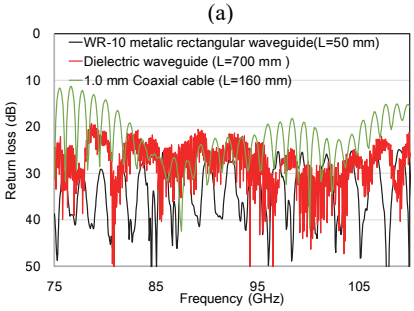

(b)

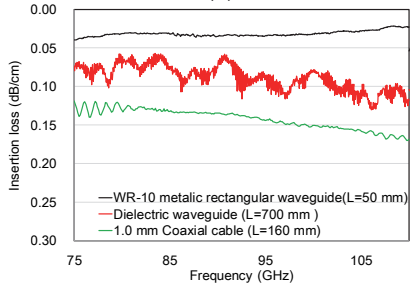

(c)

Fig.2. (a) Photographs of sample measurement by VNA. Measurement results for (b) return loss and (c) insertion loss per unit length for dielectric circular waveguide, metallic rectangular waveguide and 1.0 mm coaxial line with waveguide converters.

system built of conventional coaxial cables and dielectric waveguides. An algorithm for the probe positional control was established by MatLab® program developed by AIST. The vector network analyzer (VNA) produced by Keysight Technologies (formerly Agilent Technologies) with frequency extension modules were used for S-parameter measurements. The detail system configurations are listed in Table I. The IF bandwidth was set at 100 Hz, and the averaging factor was 1.

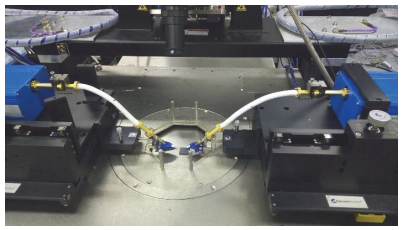

(a)

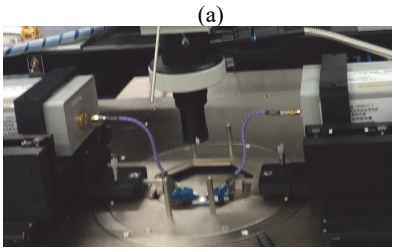

(b)

Fig.3. Measurement systems built of (a) dielectric waveguides and (b) conventional 1.0 mm coaxial cables.

The frequency was varied from 10 MHz to 110 GHz with a linear sweep, and 201 measurement points were examined.

Figure 3(a) shows a photograph of on-wafer measurement system built of dielectric waveguide. Waveguide extension module connected to probe by dielectric circular waveguide with rectangular waveguide converter at both end and 1.0 mm conversion at probe side. Figure 3(b) shows a photograph of conventional on-wafer measurement system built of 1.0 mm coaxial cable.

B. Calibration and Measurement Uncertainty

In the measurement, first, Line-Reflect-Reflect-Match (LRRM) calibration [3-6] was performed on ISS at the probe tips on the both on-wafer measurement systems. In this calibration, “Thru” line, *L*=220 μm, was used as “flush thru”. The insertion loss of “thru” line corrected as “offset insertion loss” in VNA measurement results after the on-wafer calibration. Then the comparison devices, i.e. short circuits, matched loads and mismatched line, etc., were measured.

In our measurement system, contact precision of probe tip to device pads was improved by original contact/positional algorism. The contact repeatability was 0.001 for S_{11}

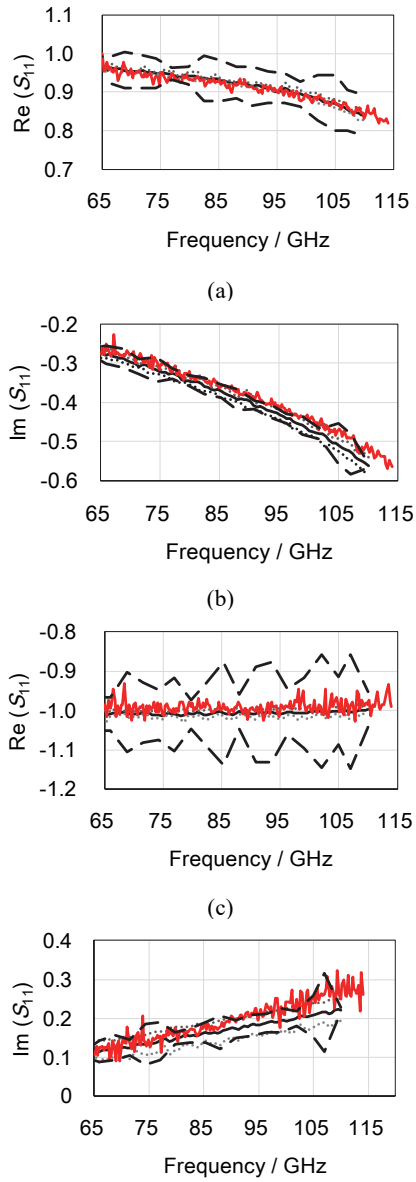

Fig.4. Measurement results for (a) real part and (b) imaginary part of S_{11} for open circuit and (c) real part and (d) imaginary part of S_{11} for short circuit.

measurement of load device at 110 GHz. This is almost one order better than conventional contact/positional algorism, i.e. optical inspection.

In the case of on-wafer measurement built of 1.0 mm coaxial cable, an approximate uncertainty analysis was executed to estimate the uncertainties contributed from probe contact/positional repeatability, the reference data of the calibration standards, and others, i.e. the noise floor, trace noise, nonlinearity, drift, etc.. In the paper, we adopted the uncertainty estimation model reported in Ref. [7-9]. All uncertainty contribution has been evaluated in advance and estimate

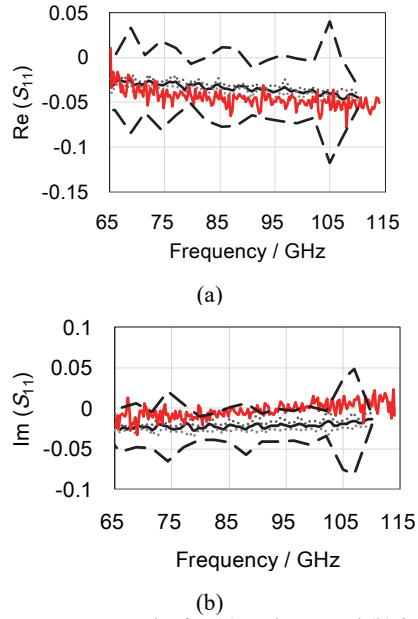

Fig.5. Measurement results for (a) real part and (b) imaginary part of S_{11} for matched load device.

measurement uncertainty for all verification device by the Monte Carlo simulation [10, 11].

IV. Verification and Comparison Results

In the paper, following three types of planar devices were used;

i) High reflect circuits, i.e. Short and Open circuits;
ii) Matched load devices;
iii) 75 ohms mismatch line.

Each verification device was measured by two different measurement systems described above.

To verify the performance of on-wafer measurement system with dielectric waveguide, we compared the measurement results to the results obtained by the measurement system with 1.0 mm coaxial cable. In the comparison, results obtained from 1.0 mm coaxial system was as a reference values. If measurement results observed from dielectric waveguide system agrees to reference values within uncertainty limits, the dielectric waveguide system has equivalent performance with 1.0 mm coaxial cable system in on-wafer measurements.

Fig. 4 shows S_{11} measurement results of open and short circuits on the substrate. Red line indicates measurement results obtained by on-wafer measurement system based on dielectric waveguides. Black solid line indicates reference values characterized by on-wafer system with 1.0 mm coaxial cables. Two black broken lines mean estimated uncertainty limit of reference values described in previous section. Measurement results of real and imaginary part of S_{11} of the device were within the uncertainty limits of reference values.

In Fig. 5, S_{11} measurement result of matched load device are

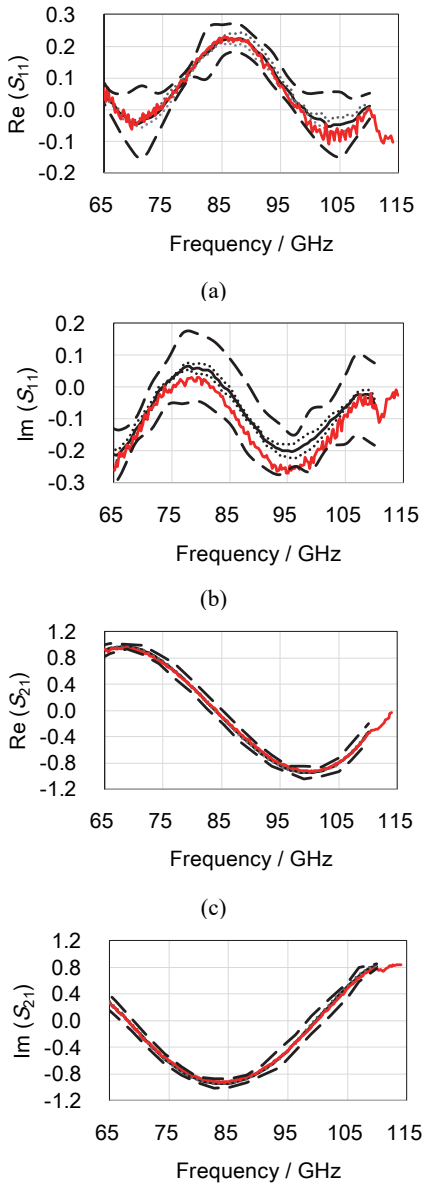

Fig.6. Measurement results for (a) real part and (b) imaginary part of S_{11},and (c) real part and (d) imaginary part of S_{21}, for mismatched line (75 Ω) device.

compared. Real part agreed well each other. However, Imaginary part of the results were slightly large compared to upper limit of the reference values. This difference is coming from noise (dynamic range) issue and positional error of the probe. However, all the measurement result was almost agreed with each other.

In Fig. 6, full S-parameter measurement and comparison were demonstrated using mismatched line with impedance of 75 Ω. All measurement result from dielectric waveguide system agreed to reference values within uncertainty limits.

The on-wafer measurement system built of dielectric waveguide provides almost the same measurement performance of the on-wafer measurement system with 1.0 mm coaxial cables.

V. Conclusion

We have developed flexible waveguide using low loss PTFE as a transmission line. The line provides flexure of waveguide with low return loss and medium insertion loss. The dielectric waveguide was adopted to on-wafer measurement system in the millimeter-wave frequency and above. The measurement system with dielectric waveguide provides the same performance of the system built of 1.0 mm coaxial cables. This means dielectric waveguide is providing innovative solution, i.e. setup flexibility compared to rigid rectangular waveguides, for on-wafer measurement at millimeter-wave frequency and above.

Acknowledgement

This work was supported by the Daikin Industries Ltd.. The author thanks Mr. Yoshiyuki Yanagimoto, former Keysight Technologies Inc. for valuable discussions.

References

[1] IEC 60154-4:1969, Flanges for waveguides. Part 4: Relevant specifications for flanges for circular waveguides.

[2] IEC 60154-2:1980, Flanges for waveguides. Part 2: Relevant specifications for flanges for ordinary rectangular waveguides

[3] A. Davidson, K. Jones, and E. Strid, “LRM and LRRM calibrations with automatic determination of load inductance”, 36th ARFTG Conf. Dig., Monterry, USA, 1990.

[4] F. Purroy, and L. Pradell, “New theoretical analysis of the LRRM calibration technique for vector network analyzers”, IEEE Trans. Inst. Meas., No. 50, Vol. 5, pp. 1307–1314 2001.

[5] A. M. E. Safwat, and L. Hayden, “Sensitivity analysis of calibration standards for SOLT and LRRM”, 58th ARFTG Conf. Dig., San Diago, USA, 2001.

[6] J. E. Pence, “Verification of LRRM Calibrations with Load Inductance Compensation for CPW Measurements on GaAs Substrates”, 42nd ARFTG Conf. Dig., Illinois, USA, 1993.

[7] M. Garelli, and A. Ferrero, “A unified theory for S-parameter uncertainty evaluation”, IEEE Trans. Inst. Meas., No. 60, Vol. 12, pp. 1307–1314, 2012.

[8] A. A. Savin, V. G. Guba, and O. N. Bykova, “Uncertainty analysis in coplanar waveguide with unscented transformation”, 86th ARFTG Conf. Dig., Atlanta, USA, 2015.

[9] V. Teppati, and A. Ferrero, “A Comparison of uncertainty evaluation methods for on-wafer S-parameter measurements”, IEEE Trans. Inst. Meas., Vol. 63, No. 4, pp. 935–942, 2014.

[10] J. P. Hoffman, P. Leuchtmann, J. Schaub, and R. Vahldiech, “Computing uncertainties of S-parameters by means of Monte Carlo Simulation”, paper presented at 69th ARFTG Conf. Dig., Honolulu, USA, 2007.

[11] M. Horibe, and R. Kishikawa, “Metrological traceability in waveguide S-parameter measurements at 1.0 THz band”, IEEE Trans. Inst. Meas., No. 62, Vol. 6, pp. 1814–1820, 2013

Lumped modeling of integrated MIM capacitors for RF applications

Falk Korndörfer* and Volker Mühlhaus†
*IHP, 15236 Frankfurt (Oder), Germany, †Dr. Mühlhaus Consulting & Software GmbH, 58455 Witten, Germany

***Abstract*—This paper presents a scalable MIM capacitor model that is applicable at RF and mm-wave frequencies. The model parameters are obtained from electromagnetic simulations and verified by measurements over a wide range of geometry parameters. A de-embedding method is described that is based on two through structures.**

***Index Terms*—MIM, Modeling, RF-measurements, Passives, S-parameters, De-embedding,**

I. Introduction

Integrated capacitors are important elements in today's RF circuit design. They are used for different purposes in integrated power amplifiers, e.g. as part of the input and output matching networks and as decoupling capacitors in the supply rails. A successful RF design requires accurate models of all components used in the circuit. In this work we present a scalable lumped model of a metal insulator metal capacitor (CMIM) which captures the strong frequency dependence as a function of the actual geometry of the device. The physical size of the capacitor introduces series inductance that leads to a frequency dependent increase of the effective series capacitance. The physical size of the capacitor also introduces a shunt capacitance from the bottom plate to the lossy silicon substrate underneath. This shunt path degrades the quality factor and increases the insertion loss. We model this similar to the shunt path in spiral inductor models [1]: a capacitor represents the oxide dielectric, a resistor plus a capacitor in parallel forms the model of the silicon substrate. We also add series elements to include the frequency dependency of the conductor losses. This results in a more accurate response over a wide frequency range compared to earlier models [2]–[4].

The dimensions of the modeled MIM capacitor type can vary in a range from $7\,\mu\mathrm{m}$ to $70\,\mu\mathrm{m}$ with square or rectangular shape. In addition, the feed line width is variable for a given capacitor width. A further degree of freedom in layout is the angle between both feed lines: $0°$, $90°$ or $180°$. With all these options, the circuit designer is extremely flexible with the layout. On the other hand, this high layout flexibility creates a tremendous amount of combinations which would have to be covered by the model. In this work we will focus on the $180°$ feed line configuration only, meaning connections from the opposite sides of the capacitor. This configuration is most often used in input/output matching networks or decoupling capacitor. The $180°$ configuration also allows the fabrication of easy and reliable measurable test structures especially with respect to the de-embedding which is required in any case. Furthermore we limit ourselves to aspect ratios from 1:2 to 2:1 to confine the complexity.

The compact model development was performed by means of 3D planar EM simulations. This approach allows us to create data points for the entire multidimensional modeling space without the need of exorbitant wafer area for the test structures. A comparison between the EM simulation and measurements was done for a limited but typical set of capacitors before starting the modeling process.

II. Test Structure

We defined a MIM capacitor layout PCell which generates two parts. The first part is the actual MIM capacitor. It is located between the inner metallization layers M2 and M3. As second part, the PCell generates a ground ring for a defined substrate coupling and a defined ground return path. We call this new layout *rfcmim* below. Due to the defined substrate contact, we are able to accurately model the substrate coupling and the influence of the ground return path on the electrical behavior of the *rfcmim*. The new layout also includes defined feed lines which are part of the electrical model. Fig. 1 shows the cross section of the new *rfcmim*. The actual MIM capacitor is inside the dotted box. The dashed box designates the part which is defined by the *rfcmim* PCell. The wiring to the topmost metallization for the later S-parameter measurements is also indicated in Fig. 1. The *rfcmim* PCell allows the generation of capacitances in a range from $50\,\mathrm{fF}$ to $4.9\,\mathrm{pF}$. Feed line width and aspect ratio are also adjustable.

A set of ten capacitors and corresponding de-embedding structures were placed in a 2port configuration of ground-signal-ground (GSG) pads for later measurements. The pitch of the GSG pads is $100\,\mu\mathrm{m}$. The dimensions of the capacitors for the measurements range from $(7 \times 7)\,\mu\mathrm{m}^2$ to $(60 \times 30)\,\mu\mathrm{m}^2$. We limited ourselves to feed line widths of $5\,\mu\mathrm{m}$ and $10\,\mu\mathrm{m}$.

We found from simulation experiments that the classical open-short-de-embedding [5] would lead to an over-de-embedding of the results. The reason for that is the assumption of a perfect 0 Ohm impedance of the short which does not hold in reality because we have to connect between different layers. Although the residual resistance of the short is small it matters if subtracted from the also small series resistance of the capacitor. We figured out that a through based de-embedding method as described in [6] is the most appropriate for our *rfcmim* measurements. We extended the method of [6] to fit to our test structures. Instead of one zero-length-through, our method uses two zero-length-through's for the de-embedding.

978-1-5090-4514-3/16/$31.00 ©2016 IEEE

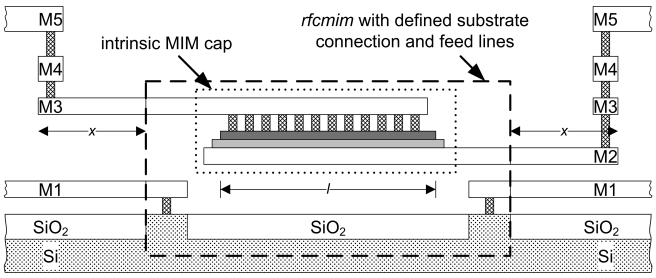

Fig. 1. Cross section of the *rfcmim* test structure. The dotted box indicates the intrinsic MIM capacitor. The dashed box marks the complete *rfcmim* PCell as defined in the design kit. A well defined substrate connection and the feed lines are part of the device.

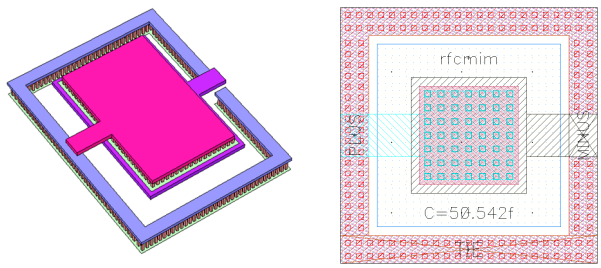

(a) 3D view (b) Layout view

Fig. 2. 3D and layout view of the new *rfcmim*

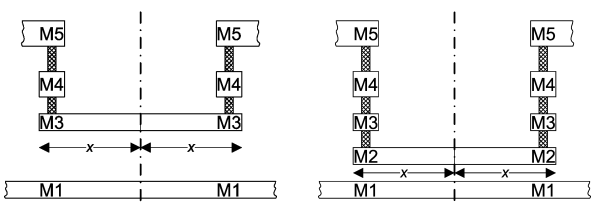

(a) M3 feed line (b) M2 feed line

Fig. 3. Cross sections of the zero-length-through's for the different feed lines. The length x corresponds to x in Fig. 1.

The second through structure is necessary since the ports of the *rfcmim* are at different metallization layer (s. Fig. 1). Each through standard itself is fully symmetrical. The through's were designed by removing the capacitor and moving the ports closer together. Fig. 3 shows the cross-sections of the zero-length-through's for the different metallization layers. The distance x marks the length of the extrinsic feed lines. It is equal for the zero-length-through's and the *rfcmim* test structures (s. Fig. 1). With a total of four through structures we were able to de-embed all measurements. We also placed structures where the *rfcmim*'s were replaced by a short between M3 and M2. These structures are used for an easier extraction of the resistive and inductive components of the model. The pads and feed lines of all structures are shielded from the silicon substrate by a metal ground plane (M1) underneath. The test structures were fabricated in IHP's $0.25\,\mu\mathrm{m}$ SiGe:C BiCMOS technology [7].

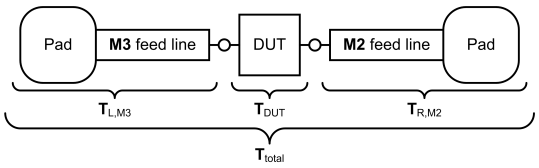

Fig. 4. Representation of the DUT and its wiring as chain matrix

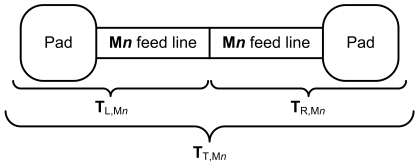

Fig. 5. Symmetrical through standard composed of two mirrored halves

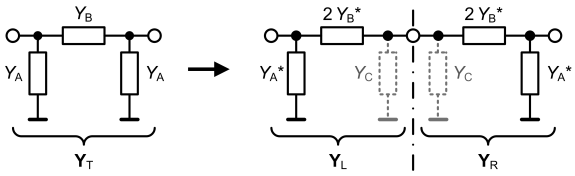

Fig. 6. Bisecting of a symmetrical through structure

III. EM Model Verification

A. Measurement Setup

The S-parameter measurements were performed on-wafer with an Agilent 8510XF vector network analyzer (VNA) in conjunction with a Suss PA200 wafer prober. We measured up to $110\,\mathrm{GHz}$ using Cascade Infinity Probes®. The VNA was calibrated using the Impedance Standard Substrate 104-783 which was placed on a ceramic auxiliary chuck. We applied the eLRRM algorithm [8] for the calculation of the error terms. The measurements, calibration and further data handling were done with Cascade's WinCalXE™software. We measured all structures at five adjacent position on the wafer.

B. De-embedding Method

As mentioned before, a through based de-embedding procedure is the most appropriate method for our test structures. We adapted the method of [6] to our test structure configuration. The combination of DUT and wiring as shown in Fig. 4 can be written in chain matrix form:

$$\mathbf{T}_{\mathrm{total}} = \mathbf{T}_{\mathrm{L,M3}} \cdot \mathbf{T}_{\mathrm{DUT}} \cdot \mathbf{T}_{\mathrm{R,M2}}. \tag{1}$$

Once $\mathbf{T}_{\mathrm{L,M3}}$ and $\mathbf{T}_{\mathrm{R,M2}}$ are known the DUT characteristics can by calculated:

$$\mathbf{T}_{\mathrm{DUT}} = \mathbf{T}_{\mathrm{L,M3}}^{-1} \cdot \mathbf{T}_{\mathrm{total}} \cdot \mathbf{T}_{\mathrm{R,M2}}^{-1} \tag{2}$$

$$\mathbf{T}_{\mathrm{DUT}} = \mathbf{T}_{\mathrm{L,M3}}^{-1} \cdot \mathbf{T}_{\mathrm{L,M3}} \cdot \mathbf{T}_{\mathrm{DUT}} \cdot \mathbf{T}_{\mathrm{R,M2}} \cdot \mathbf{T}_{\mathrm{R,M2}}^{-1}. \tag{3}$$

The matrices $\mathbf{T}_{\mathrm{L,M3}}$ and $\mathbf{T}_{\mathrm{R,M2}}$ are obtained by bisecting of symmetrical through structures in two identical but mirrored halves. Bisecting means solving

$$\mathbf{T}_{\mathrm{T,M}n} = \mathbf{T}_{\mathrm{L,M}n} \cdot \mathbf{T}_{\mathrm{R,M}n} \tag{4}$$

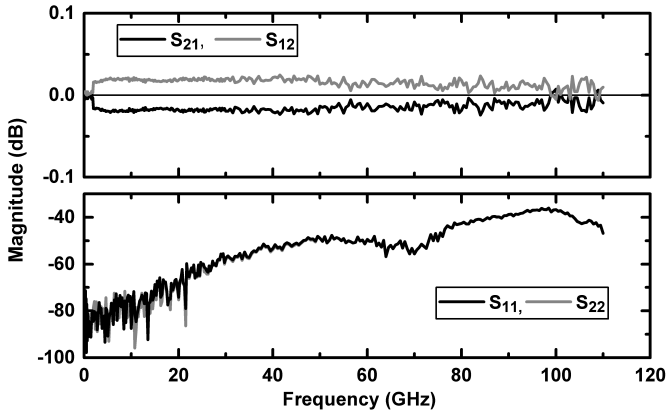

Fig. 7. Results after applying the through de-embedding to the through structure itself (M2 through, $w_\mathrm{f} = 5\,\mu\mathrm{m}$)

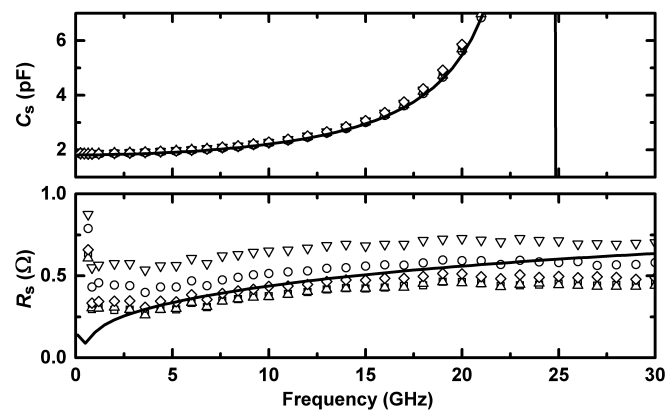

Fig. 8. Measurement (symbols) and EM simulation (line) results of the effective series capacitance and the effective series resistance of a *rfcmim* with $w = 60\,\mu\mathrm{m}$, $l = 30\,\mu\mathrm{m}$, $w_\mathrm{f} = 10\,\mu\mathrm{m}$.

for the structure shown in Fig. 5. Expressing a through as Y-matrix, its bisecting is illustrated in Fig. 6. In the general solution the element Y_C differs from zero, $Y_\mathrm{A}^* \neq Y_\mathrm{A}$ and $Y_\mathrm{B}^* \neq Y_\mathrm{B}$. The problem cannot be solved directly since this equation system is under-determined. There are two knowns but three unknowns. One solution method is shown in [9], [10]. It uses optimization algorithms to determine the unknown elements.

In our test structure configuration the admittance of the pad is the dominating shunting element, thus we follow with the approach of [6] and assume $Y_\mathrm{C} = 0$. In that case $Y_\mathrm{A}^* = Y_\mathrm{A}$ and $Y_\mathrm{B}^* = Y_\mathrm{B}$ and can easily be calculated from $\mathbf{Y}_\mathrm{T}$. We compute

$$Y_\mathrm{A} = 0.5\,(Y_{11} + Y_{22} + Y_{21} + Y_{12}) \tag{5}$$

$$2\,Y_\mathrm{B} = -\,(Y_{21} + Y_{12})\,. \tag{6}$$

to enforce symmetry and to even out small unbalances caused by imperfections of the measurements. The left and right halve of the bisected through are then given by

$$\mathbf{Y}_\mathrm{L} = \begin{bmatrix} Y_\mathrm{A} + 2\,Y_\mathrm{B} & -2\,Y_\mathrm{B} \\ -2\,Y_\mathrm{B} & 2\,Y_\mathrm{B} \end{bmatrix} \tag{7}$$

$$\mathbf{Y}_\mathrm{R} = \begin{bmatrix} 2\,Y_\mathrm{B} & -2\,Y_\mathrm{B} \\ -2\,Y_\mathrm{B} & Y_\mathrm{A} + 2\,Y_\mathrm{B} \end{bmatrix} \tag{8}$$

and are converted to the corresponding chain matrices $\mathbf{T}_{\mathrm{L,M}n}$ and $\mathbf{T}_{\mathrm{R,M}n}$ for the later calculations.

C. De-embedding Verification

Applying the previously described de-embedding method to the through structure itself should result in a perfect zero-length-through. The expected results are $S_{21} = S_{12} = 1$ as well as $S_{11} = S_{22} = 0$. Fig. 7 shows the results of the M2 through with $5\,\mu\mathrm{m}$ width. The transmission remains within $\pm 0.03\,\mathrm{dB}$ over the entire frequency range. The reflection stays below $-35\,\mathrm{dB}$. The verification with the through for M3 metallization gave similar results. The verification results show the excellent performance of the through de-embedding.

D. Results

Fig. 8 shows the measurement and EM simulated results of the effective series capacitance C_s and the effective series resistance R_s of a $60\,\mu\mathrm{m} \times 30\,\mu\mathrm{m}$ *rfcmim* with $10\,\mu\mathrm{m}$ feed line width. The parameters C_s and R_s are calculated as

$$C_\mathrm{s} = -\frac{1}{2\pi f\,\Im\{Z_\mathrm{s}\}} \tag{9}$$

$$R_\mathrm{s} = \Re\{Z_\mathrm{s}\} \tag{10}$$

with $Z_\mathrm{s} = -2\,(Y_{21} + Y_{12})^{-1}$. Measurement and EM simulation results fit excellent. The variation of the series resistance in the measurements is attributed to the non-perfect reproducibility of the contact resistance. Measurement and EM simulation of the medium size *rfcmim*'s also fit very well (not shown here). In case of the smallest *rfcmim* we found a strong difference between the simulated and the measured series resistance. The reason is the difficulty to extract a small real part from a high impedance. Here, the higher dynamic range of the EM simulation is beneficial. We can conclude that the EM model simulation results are a reliable data source for the lumped model parameter extraction.

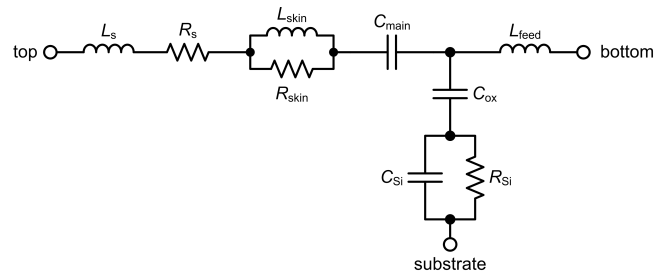

Fig. 9. Topology of the *rfcmim* lumped model

IV. The RFCMIM Lumped Model

A. Topology

The topology of the model is derived from the physical structure of the *rfcmim*. It is shown in Fig. 9. It consists of the main capacitance C_main, a series resistance R_s, and a series inductance L_s. The element L_s represents the inductance of the feed line to the upper plate and the inductance of the capacitor

itself. The inductance of the bottom feed line is modeled by L_{feed}. The skin effect is taken into account by the parallel connection of R_{skin} and L_{skin}. The capacitance C_{ox} in series with the parallel circuit of C_{Si} and R_{Si} composes the substrate network.

B. Model Equations

The following sections list the equations which we implemented in the *rfcmim* model. The parameter l is the dimension of the intrinsic capacitor in direction of the current flow. The dimension perpendicular to the current flow is denoted by w. The width of the feed lines is given by w_{f}.

1) Series Elements:

$$C_{\mathrm{main}} = C_{\mathrm{A}} w\, l + 2\, C_{\mathrm{P}}\, (w + l) \tag{11}$$

$$R_{\mathrm{s}} = R_{\mathrm{s0}} + R_{\mathrm{s1}} \frac{l}{w} + R_{\mathrm{s2}} \frac{l^2}{w} + R_{\mathrm{s3}}\, l + R_{\mathrm{s4}} \frac{1}{w_{\mathrm{f}}} \tag{12}$$

$$R_{\mathrm{skin}} = R_{\mathrm{skin0}} + R_{\mathrm{skin1}}\, l \tag{13}$$

$$L_{\mathrm{s}} = L_{\mathrm{feed}} + L_{\mathrm{plate}} - L_{\mathrm{skin}} \tag{14}$$

$$L_{\mathrm{feed}} = L_{\mathrm{f0}} + L_{\mathrm{f1}}\, w - L_{\mathrm{f2}} \log \frac{w_{\mathrm{f}}}{1\,\mu\mathrm{m}} \tag{15}$$

$$L_{\mathrm{plate}} = L_{\mathrm{plate1}}\, l + L_{\mathrm{plate2}} \frac{l}{w} \tag{16}$$

$$L_{\mathrm{skin}} = L_{\mathrm{skin0}} + L_{\mathrm{skin1}}\, l \tag{17}$$

2) Shunt Elements:

$$C_{\mathrm{ox}} = C_{\mathrm{ox0}} + 2\, C_{\mathrm{ox1}}\, (w + l) + C_{\mathrm{ox2}}\, w\, l + C_{\mathrm{f1}}\, w_{\mathrm{f}} \tag{18}$$

$$C_{\mathrm{Si}} = C_{\mathrm{Si0}} + 2\, C_{\mathrm{Si1}}\, (w + l) + C_{\mathrm{Si2}}\, w\, l \tag{19}$$

$$R_{\mathrm{Si}} = R_{\mathrm{Si0}} + 2\, R_{\mathrm{Si1}}\, (w + l) + R_{\mathrm{Si2}}\, w\, l \tag{20}$$

V. Results

We used the Keysight ADS software for extraction, fitting, and final optimization of the model parameters. Table I summarizes the obtained parameters of the new *rfcmim* model. With this parameter set the low frequency capacitance is reproduced with less than $\pm 1\,\%$ deviation between EM model and lumped model. The self resonance frequency is modeled better than $\pm 3\,\%$ in most cases. The worst case deviation of the resonance frequency is $7\,\%$.

VI. Conclusion

We presented an improved lumped model of an integrated MIM capacitor. The modeling is based on EM simulation results that were verified by measurements up to $110\,\mathrm{GHz}$. The new model takes into account the influence of the lossy silicon substrate and the inductance caused by the ground return path. Furthermore, the skin effect in the series resistance is modeled. The new model correctly depicts the geometry effects on the the self resonance. The self resonance frequency is predicted better than $\pm 3\,\%$ in most cases. We also presented a de-embedding method based on the bisecting of two zero-length-through structures. This method does not show over de-embedding effects.

TABLE I
Results of the parameter extraction

Parameter	Value	Parameter	Value
C_{A}	$1.0\,\mathrm{fF/\mu m^2}$	L_{f0}	$6.52\,\mathrm{pH}$
C_{P}	$50\,\mathrm{aF/\mu m}$	L_{f1}	$92.4\,\mathrm{fH/\mu m}$
R_{s0}	$112\,\mathrm{m\Omega}$	L_{f2}	$4.68\,\mathrm{pH}$
R_{s1}	$34.1\,\mathrm{m\Omega}$	C_{ox0}	$43.2\,\mathrm{aF}$
R_{s2}	$15.1\,\mathrm{\mu\Omega/\mu m}$	C_{ox1}	$66.6\,\mathrm{aF/\mu m}$
R_{s3}	$1.77\,\mathrm{m\Omega/\mu m}$	C_{ox2}	$7.23\,\mathrm{aF/\mu m^2}$
R_{s4}	$885\,\mathrm{m\Omega\,\mu m}$	C_{f1}	$85\,\mathrm{aF/\mu m}$
R_{skin0}	$206\,\mathrm{m\Omega}$	C_{Si0}	$36.2\,\mathrm{fF}$
R_{skin1}	$6.14\,\mathrm{m\Omega/\mu m}$	C_{Si1}	$276\,\mathrm{aF/\mu m}$
L_{plate1}	$372\,\mathrm{fH/\mu m}$	C_{Si2}	$3.29\,\mathrm{aF/\mu m^2}$
L_{plate2}	$483\,\mathrm{fH}$	R_{Si0}	$827\,\Omega$
L_{skin0}	$1.68\,\mathrm{pH}$	R_{Si1}	$-2.49\,\Omega/\mu\mathrm{m}$
L_{skin1}	$85.4\,\mathrm{fH/\mu m}$	R_{Si2}	$48.5\,\mathrm{m\Omega/\mu m^2}$

Acknowledgment

The authors would like to thank Uwe Roßmann for the programming of the *rfcmim* PCell.

References

[1] C. P. Yue and S. S. Wong, "Physical modeling of spiral inductors on silicon," *IEEE Trans. Electron Devices*, vol. 47, no. 3, pp. 560–568, Mar. 2000.

[2] H. D. Ky, S. Meszaros, M. Cuhaci, and B. Syrett, "Physical lumped modelling of thin-film MIM capacitors," in *Microwave Conference, 1990. 20th European*, vol. 2, Sep. 1990, pp. 1269–1275.

[3] P. Lombard, J. D. Arnould, O. Exshaw, H. Eusebe, P. Benech, A. Farcy, and J. Torres, "MIM capacitors model determination and analysis of parameter influence," in *Industrial Electronics, 2005. ISIE 2005. Proceedings of the IEEE International Symposium on*, vol. 3, Jun. 2005, pp. 1129–1132.

[4] D. Gruner, Z. Zhang, V. Subramanian, F. Korndörfer, and G. Böck, "Lumped element MIM capacitor model for Si-RFICs," in *2007 SBMO/IEEE MTT-S International Microwave and Optoelectronics Conference*, 2007.

[5] M. C. A. M. Koolen, J. A. M. Geelen, and M. P. J. G. Versleijen, "An improved de-embedding technique for on-wafer high-frequency characterization," in *Proceedings of the 1991 Bipolar Circuits and Technology Meeting*, 1991.

[6] H. Ito and K. Masuy, "A simple through-only de-embedding method for on-wafer s-parameter measurements up to 110 GHz," in *2008 IEEE MTT-S International Microwave Symposium Digest*, 2008.

[7] B. Heinemann, R. Barth, D. Knoll, H. Rücker, B. Tillack, and W. Winkler, "High-performance BiCMOS technologies without epitaxially-buried subcollectors and deep trenches," in *2006 International SiGe Technology and Device Meeting*, 2006.

[8] L. Hayden, "An enhanced line-reflect-reflect-match calibration," in *Proceedings of the 67th ARFTG Conference*, Jun. 2006.

[9] E. Daniel, "Bisect de-embedding for network analyzer measurement," US Patent US20 060 056 310 A1, Mar. 16, 2006.

[10] ——, "Bisect de-embedding for network analyzer measurement," US Patent US7 643 957 B2, Jan. 5, 2010.

Design of WR-6 (110GHz ~ 170GHz) Waveguide Microcalorimeter

Wenze Yuan, Chao Ma, Xiaohai Cui, and Yong Li

National Institute of Metrology, Beijing, China
E-mail: cuixh@nim.ac.cn

***Abstract* — A WR-6 (110GHz~170GHz) waveguide microcalorimeter as the primary power standard has been recently developed in the National Institute of Metrology, China (NIM). The new thermoelectric conversion power sensor is designed which is the key part in the WR-6 microcalorimeter. In this paper, the structure design and analyzing methods of the new power sensor will be described in detail, and preliminary measurement results of the uncorrected effective efficiency will be shown.**

***Index Terms* — WR-6 microcalorimeter, power sensor, uncorrected effective efficiency.**

I. INTRODUCTION

The unique position of terahertz (THz) wave in the electromagnetic spectrum brings it many excellent features. The terahertz technique has attracted much attention from a variety of fields such as communication, imaging, etc. [1]. Reliable and practical measurement standards are important to support the development of terahertz technique. It has become an urgent task to develop terahertz power standards, as power is the key parameter of THz wave. The frequency of power standards in National Institute of Metrology, China (NIM) has reached up to 110GHz with the development of a series of rectangular waveguide power primary standards.

Recently, NIM developed a WR-6 (110GHz ~ 170GHz) power standard to improve its power measurement capability. A WR-6 microcalorimeter system was established to serve as the power primary standard and a new power sensor as the key part of the microcalorimeter was designed. In this paper, the structure design, measurement methodologies and experiment results will be reported.

II. MICROCALORIMETERS AND POWER SENSORS

A. Microcalorimeters

Microcalorimeters serve as millimeter-wave power primary standards in many national metrology institutes (NMIs). NIM also established microcalorimeter systems to serve as primary national standards of microwave and millimeter-wave power of China. Microcalorimeters can be used to determine the effective efficiency of a transfer standard which is a thermoelectric conversion power sensor by measuring the total RF power dissipated in the sensor and the DC power [2]. The effective efficiency η_e can be calculated using the following equation.

$$\eta_e = \mathrm{g}\eta_{e,\mathrm{uncor}} = \mathrm{g}\frac{1-\left(\frac{V_2}{V_1}\right)^2}{\frac{e_2}{e_1}-\left(\frac{V_2}{V_1}\right)^2} \qquad (1)$$

Here V_1 and e_1 are the output voltages of the power meter and the thermopile with only DC applied to the power sensor. V_2 and e_2 are the same voltages when both DC and RF were applied simultaneously. g is the correction factor of the microcalorimeter and $\eta_{e,\mathrm{uncor}}$ is the uncorrected effective efficiency [3].

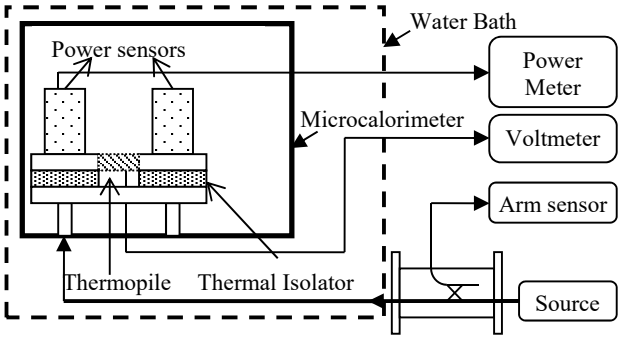

Fig.1 Schematic diagram of WR-6 microcalorimeter system

B. Power Sensors

Generally, commercial thermistor mounts serve as the transfer standards in the microcalorimeters. Unfortunately, with requirement of broad work band, there are no commercial thermistor mounts available for the WR-6 microcalorimeter. We designed a new WR-6 (110GHz ~ 170GHz) terahertz power sensor for the microcalorimeter, because the attempt to extend the work frequency range of thermistor mounts with connecting linear tappers was failed.

In the past, a WR-28 (26.5GHz ~ 40GHz) waveguide broadband power sensor was designed as the power transfer standard (Fig.2).

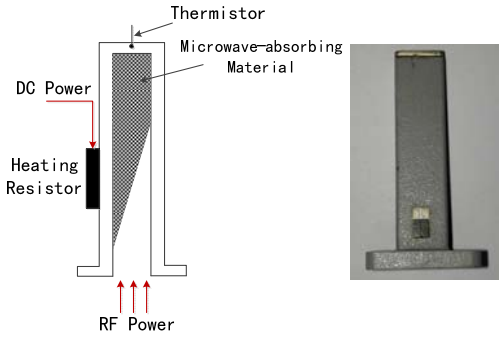

Fig.2 WR-28 broadband power sensor

978-1-5090-4514-3/16/$31.00 ©2016 IEEE

When microwave power is put into the sensor, resistance of the thermistor which serves as a temperature sensor will be maintained constant by regulating the DC power applied to the heating resistor. The absorbed RF power can be represented by the variation of dc power which is usually called substituted DC power. Because the heat transfer path of DC power to the temperature sensor is not identical with that of absorbed RF power, it is difficult to obtain the relationship between them [4]. With the decrease in waveguide sizes, there are much more difficulties from the difference of thermal paths to analyze the relationship between DC substitute power and RF power.

Hence, learned from the old broadband sensor, tightly we integrated the RF load, the DC heating resistor and the temperature sensor together into a sensor chip with the microelectronic technology to bring nearly identical thermal paths.

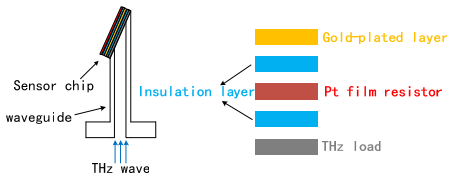

Fig.3 WR-6 power sensor

Pt film resistor can substitute the DC heating resistor and the temperature sensor because it has excellent stability and linearity as one of RTDs in a large temperature range. The Pt film resistor is biased and applied DC power to keep its resistance constant. When the chip absorbs THz power, the temperature will change. The DC power applied to the Pt resistor will automatically be reduced to keep the temperature and resistance constant.

Many materials such as silicon substrate, carbonyl iron particles, carbon nanotubes, wave-absorbing ceramics, served as the THz load, was tested to obtain higher THz wave absorptivity. The reflectivity of the power sensor is selected to estimate the property of the wave-absorbing materials. Considering smoothness of the reflectivity and the complexity of manufacture, the silicon substrate was chosen to be the load, and its reflectivity $|\Gamma|$is showed in Fig.4.

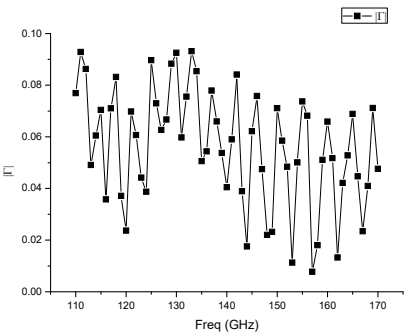

Fig.4 Reflectivity of the power sensor

Stainless steel is used for the waveguide because of its low thermal conductivity, and the thickness of the waveguide is 0.1mm. Hence, the waveguide with low thermal conductivity and thermal capacity can improve the sensitivity and the response time of the power sensor to THz power.

To prevent THz power leakage, the sensor chip is sealed carefully to the waveguide with conductive silver adhesives and the top layer of the chip is gold-plated.

III. Measurement Results

The temperature change of laboratory is controlled within 1℃ and the WR-6 microcalorimeter is placed in the water bath in which the temperature stability can reach 0.8m ℃。The sensor chip is biased and applied DC power by a modified self-balanced bridge. The uncorrected effective efficiency $\eta_{e,\mathrm{uncor}}$ is showed in Fig. 5. The determination of correction factor g and the uncertainty analysis are in our future plans.

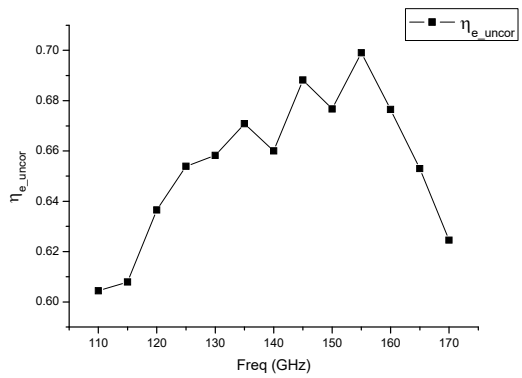

Fig.5 Uncorrected effective efficiency $\eta_{e,\mathrm{uncor}}$

IV. Summary

A WR-6 waveguide microcalorimeter has been briefly reported in this paper. A new power sensor was designed to serve as the transfer standard in the microcalorimeter. The power sensor has quite low reflectivity in the broad frequency range. The heat transfer paths of DC and THz power are nearly identical because of the sensor chip. Measurement results of uncorrected effective efficiency indicate the good performance of the new power sensor.

Acknowledgement

This work was supported by the National Science and Technology Supporting Program “Wireless Communication Power Measurement Standard and Traceability Technology Research” of China under Grant No. 2014BAK02B02.

REFERENCES

[1] Renbin Zhong, “Study of Terahertz Transmission Lines”, University of Electronic Science and Technology of China, 2012.

[2] Cui, Xiaohai, et al. "Correction factor evaluation technique for a rectangular waveguide microcalorimeter." Arftg Microwave Measurement Conference 2013:1-3.

[3] J. W. Allen, F. R. Clague, N. T. Larsen, and M. P. Weidman, “NIST microwave power standards in waveguide,” *NIST Technical Note 1511*, Feb. 1999.

[4] Cui, Xiaohai, et al. "Design and measurement of a WR-28 calorimeter." Precision Electromagnetic Measurements IEEE, 2010:773-774.

CAD-Assisted Microwave Characterization of Ink-Jet Printed CPW on PET Substrates

A. Sahu*,V. Devabhaktuni*,A. Lewandowski†, T. M. Wallis‡, and P. H. Aaen§
*Dept. of Electrical Engineering and Computer Science,The University of Toledo, Toledo, Ohio, USA
† Institute of Electronic Systems, Warsaw University of Technology, Warsaw, Poland
‡National Institute of Standards and Technology Boulder, Colorado, USA
§Department of Electronic Engineering, Advanced Technology Institute, University of Surrey, UK
Email: Abhishek.Sahu@utoledo.edu

***Abstract*— This paper describes the computer-aided-design (CAD)-assited microwave characterization of coplanar waveguide (CPW) lines formed by ink-jet printed technology on flexible polyethylene terephthalate (PET) substrates. A space-mapping technique is used to link the measured results with simulations and the mapping is used to extract the electrical properties of the ink and supporting dielectric spacer employed during measurements. Results indicate that the losses in lines are predominantly due to the loss tangent of the substrate and the conductivity of the ink. Estimates of the conductivity of the ink and the dielectric constant of the spacer used during measurement were obtained as 2.97×10^7 S/m, and 1.79 respectively.**

***Index Terms*— Ink-jet printed CPW, flexible substrates, multiline calibration, CAD**

I. INTRODUCTION

To enable microwave circuits for emerging markets like the internet-of-things (IoT), there is a need for the inexpensive manufacture of environmentally friendly electronics and ink-jet printing has received significant recent interest. Inkjet printing allows the use of non-traditional substrate materials, for example polyethylene terephthalate (PET) and paper, which are very inexpensive. In addition, these substrates are mechanically flexible and can conform to non-planar geometries. The manufacturing process is additive and only the ink needs to be added to the substrate. Circuits can then be printed using ink-jet printers or even roll-to-roll printing systems. Additive manufacturing is suitable for rapid, cost-effective mass manufacturing. Recent research has led to the development of various components such as radio frequency identification (RFID) tags [1], antennas [2], [3], and coplanar waveguides (CPW) [4] by use of ink-jet printing on flexible substrates such as Kapton [5].

Polyethylene terephthalate (PET) is a widely used flexible substrate that is being explored for microwave circuit design. CPWs on flexible PET were reported to have an attenuation of 0.6 dB/mm at 40 GHz [6]. Furthermore, meander inductors have been successfully designed on PET substrates [7], [8]. In order to understand the limitations of substrate selection and to offer development guidance on new, nano-particle based metallic inks and their processing, there is a need to have robust, repeatable and accurate characterization.

Recently, the authors presented calibrated microwave measurements of ink-jet-printed CPWs on a PET substrate as a first step toward developing a broadly-applicable test platform for evaluation of flexible, ink-jet-printed microwave circuits as well as their constituent materials [9]. Utlizing a novel metrology, it was shown that repeatable measurements can be performed for inkjet printed circuits on PET. Nevertheless, there is an urgent need for a robust metrology to quantitatively characterize the constituent inks and components fabricated using such techniques.

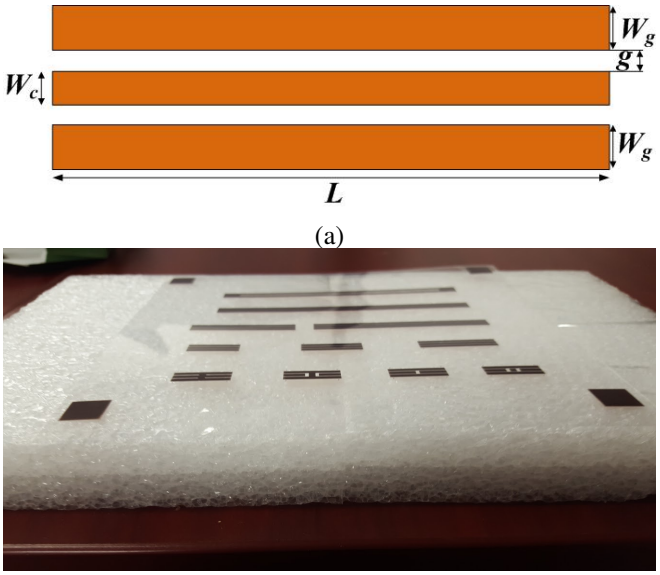

Fig. 1. (a) CPW dimensions (b) Photograph of fabricated CPW lines on PET substrates with spacer underneath.

A TDR/TRT and S-parameter measurement based characterization of ink-jet printed interconnects was reported in [10]. Electrical performance characterization of a flexible circuit for mobile application was presented in [11]. Nevertheless, a robust metrology to characterize the ink properties on PET-based substrates is yet to be reported. To this end, we report a CAD-assisted space mapping technique to characterize ink-jet-printed CPW lines on a PET substrate. Section II describes the fabrication and measurement of CPW lines. Characterization and parameter extraction methodology is described in section III. Results and conclusions are discussed in section IV and V.

978-1-5090-4514-3/16/$31.00 ©2016 IEEE

II. Fabrication and Measurement of CPW Lines

A. Fabrication

The fabrication process was performed using a commercial process [12]. The process uses ink-jet printing as a precursor on which copper is electroplated. In this work, the copper is plated to be approximately 2 μm thick. We used a clear PET substrate for our work due to its much lower cost compared to other flexible circuits such as polymide and Kapton, high chemical resistance to acids and solvents, and ability to withstand higher operating temperature than other thermoplastics. Contact profilometer measurements were performed on the traces revealed their thickness to be approximately $2\mu m$ over the entire substrate with a surface roughness of about $0.2\mu m$.

Figure 1(a) is a photograph of a CPW line with (W_c) 1.983 mm, gap width (g) 0.13 mm, ground conductor width (W_g) 1.983 mm, substrate thickness 125 μm and copper thickness 2 μm. The line lengths were determined based on the approach in reference [13]. A multiline TRL calibration kit was designed with six CPW lines having lengths of 14.97 mm, 18.42 mm, 23.57 mm, 35.78 mm, 61.60 mm, and 97.93 mm. Additionally, a CPW Short circuit has been fabricated for use as a reflect standard in the mulitline TRL calibration.

B. Measurement

The CPW lines were measured using a commercial on-wafer probe station, a vector network analyzer (VNA), and ground-signal-ground contact probes (1.0 mm pitch). During measurements, the PET substrate was supported by a 0.5 cm-thick, porous dielectric. The power level of the VNA was set to -17.0 dBm and the uncorrected S-parameters were measured for each device from 0.1 GHz to 20 GHz. We adopted a multiline Thru-Reflect-Line calibration [6] technique to characterize the propagation constant and reflect reflection coefficient of the CPW lines.

III. Characterization and Parameter Extraction

We utilized a CAD-based space mapping methodology to characterize the fabricated ink-jet printed CPW lines. To this end, the dielectric constant and loss tangent of PET are well characterized in literature and hence were kept as their standard values as 3.1 and 0.01 respectively. A simulation was performed utilizing these values to compare with measurement. CPW lines were drawn on PET substrates and the dielectric spacer was then designed underneath. Open boundary conditions were defined around the model and at the bottom PEC boundary condition was defined as per the measurement set up. Figure 2 shows the simulation setup developed in Ansys's $HFSS^{\|}$ to carry out the EM simulation.

Since there are two unknown parameters in the experiment, let us define the conductivity of the copper electroplated ink-jet printed lines as *sigma* and the dielectric constant of the spacer underneath as *epsr*. The resulting attenuation and phase constants here are defined as α and β.

$^{\|}$Trade names are used for clarity and do not imply endorsement by NIST.

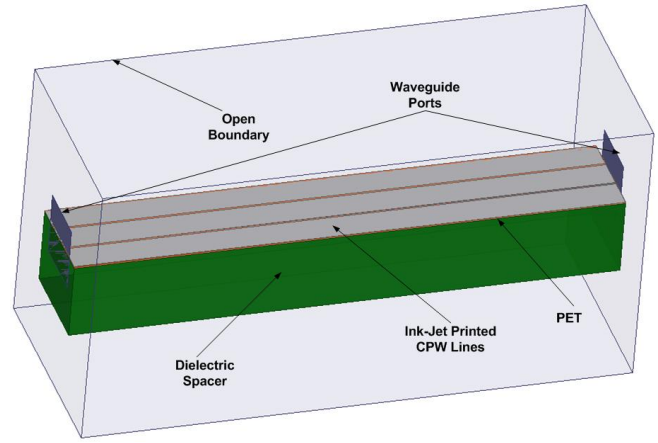

Fig. 2. Simulation setup of CPW lines for proposed methodology.

The proposed methodology to extract the unknown parameters from simulation and measurement data set is summarized as below.

step 1: Start the simulation with an initial value of $sigma_0$ and $epsr_0$.

step 2: Keep the $sigma_0$ fixed and find different values of β by varying $epsr_0$. Define an optimization function as the difference of the measurement and the simulated results. Obtain an optimized value of $epsr_0$ to provide the best match for beta between EM simulation and measurement data set.

step 3: Following step 2, obtain a *sigma* that provides the best match for α between Em simulation and measurement data set. Define this as $sigma_1$.

step 4: keep $sigma_1$ fixed, and obtain $epsr_1$ to give best match for β between simulation and measurement.

step n: Iterate *step 1- step 3* till you get a convergence between simulation and measurement grids for *sigma* and *epsr*.

The above approach is easily cast in the framework of space mapping [14]. In the above context, the measurement data set is the fine model and the EM analysis result is the coarse model.

IV. Results and Analysis

Following the methodology described above, we performed several iterations to obtain the value of unknown parameters. The dielectric constant and loss tangent of PET substrate were defined as 3.1 and 0.01. Additionally, the initial values for *sigma* and *epsr* were set as 8.54×10^7 S/m (same as copper) and 3.1 (same as PET) to define an uniform model for iteration 1. After each iteration, we updated the search range by observing the results from previous iterations. It was observed that the search engine converged after six iterations. The final values of *sigma* of the ink and *epsr* of the dielectric spacer were found to be 2.97×10^7 S/m and 1.79. Figure 3 depicts the comparison of attenuation and phase constant plots from EM simulation and measurement. As can be observed, both the results are in agreement, which demonstrates the general effectiveness of the proposed methodology. However, there is a slight mismatch for the

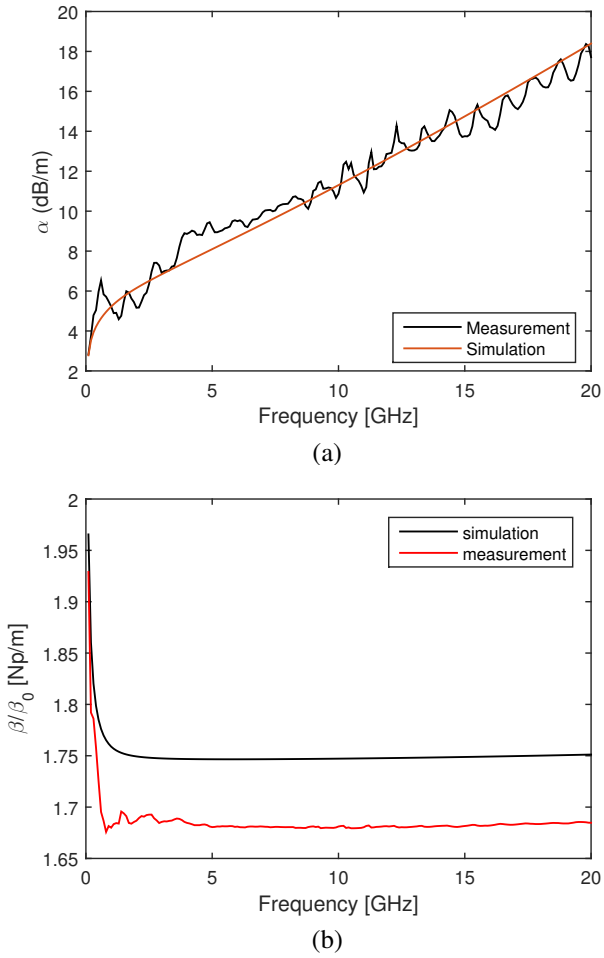

Fig. 3. (a) Comparison of attenuation constant from measurement and simulation (b) Comparison of normalized phase constant from measurement and simulation

normalized β from simulation and measurement which is attributed to the small gap between the porous dielectric and PET. The ripples in the measured attenuation might be due to imprecise probe positioning during measurement. Furthermore, it was also observed that the losses in the CPW lines are mostly affected by the conductivity of the ink and loss tangent of PET substrate. The loss tangent of the dielectric spacer has minimal effect on the overall losses.

V. CONCLUSIONS

This paper proposes a methodology for characterization of CPW lines on flexible PET substrate. Using a CAD-based space mapping method, we were able to extract the conductivity of the electroplated copper ink and the dielectric constant of the spacer used in the measurement. By utilizing the known parameters of PET from fine model, the unknown ink conductivity and spacer dielectric constant are extracted from the coarse model as 2.9734×10^7 S/m and 1.786 respectively. Results obtained from simulation agree quite well with measurement. However, as the porous dielectric is not entirely flat there is a small gap between the PET and the spacer that leads to a slight mismatch in results. Together these results demonstrate a viable and robust technique for characterization of ink-jet printed microwave circuits as well as the constituent materials.

REFERENCES

[1] M. A. Ziai and J. C. Batchelor, "Temporary on-skin passive UHF RFID transfer tag," *IEEE Trans. Antennas Propag.*, vol. 59, no. 10, pp. 35653571, Oct. 2011.

[2] G.A. Casula, G. Montisci and G. Mazzarella, "A Wideband PET InkjetPrinted Antenna for UHF RFID," *IEEE Antennas Wireless Propag. Lett.*, vol. 12, pp. 1400-1403, 2013.

[3] T. Peter, Y.Y. Sun, T.I. Yuk, H.F. AbuTarboush, R. Nilavalan and S.W.Cheung, "Miniature transparent UWB antenna with tunable notch for green wireless applications," *Antenna Technology (iWAT)*, 2011 International Workshop on, pp. 259-262.

[4] K. Hettak, T. Ross, R. James, A. Momciu and J. Wight, "Flexible Polyethylene Terephthalate-based inkjet printed CPW-fed monopole antenna for 60 GHz ISM applications," *Microwave Conference (EuMC), 2013 European*, pp. 1447-1450.

[5] S. Swaisaenyakorn, P. R. Young and M. Shkunov,"Characterization of inl-jet printed CPW on Kapton substrates at 60 GHz" *Loughborough Antennas and Propagation Conference (LAPC), 2014, UK*, pp. 676-678.

[6] K. Hettak et al, "Low-cost mm-wave coplanar waveguide bandpass filter using inkjet printing of silver nano-particles on flexible plastic substrate," *Proc. IEEE International Microwave Symposium*, 17-22 May 2015, pp: 1-3.

[7] A. B. Menicanin, L. D. Zivanov, M. S. Damnjanovic and A. M. Maric, "Low-cost CPW meander inductors utilizing ink-jet printing on flexible substrate for high-frequency applications," *IEEE Trans. Electron Devices*, vol. 60, no. 2, pp. 827-832, Jan. 2013.

[8] A. Manicanin, L. Zivanov, C. Zlebic, M. Kisic, N. Blaz and M. damnzanovic, "Fully inkjet printed CPW meander inductors on PET flexible substrate," *in 38th Int. Spring Seminar on Elect. Tech.*, Eger, May 6-10 2015, pp. 43-46.

[9] A. Sahu, V. Devabhaktuni, A. Lewandowski, T. M. Wallis, and P. Aaen, "Microwave Characterization of Ink-Jet Printed CPW on PET Substrates," *in 86th ARFTG Microwav eMeasurment conference.*, Atlanta, GA, Dec 3-4 2015, pp. 1-4.

[10] B. Shao, R. Weerasekara, A. T. Woldegiorgis, Li-Rong Zheng, R. Liu, and W. Zapka, "High frequency characterization and modelling of inkjet printed interconnects on flexible substrate for low-cost RFID applications," *Electronics System-Integration Technology Conference*, Greenwich, 1-4 Sept. 2008, pp. 695-700.

[11] S. Koskinen, L. Pykari, and M. Mantisalo, "Electrical Performance Characterization of an Inkjet-Printed Flexible Circuit in a Mobile Applications," *IEEE Trans.Compon. Packag. Manufac. Tech.*, vol. 3, no. 9, pp. 1604-1610, Sep. 2013.

[12] http://inkjetflex.com/site/rapid-prototyping/.

[13] A. Lewandowski, W. Wiatr, L.J. Opalski, and R. Biedrzycki, "Accuracy and bandwidth optimization of the over-determined offset-short reflectometer calibration" *IEEE Trans. Microw. Theory Tech.*, vol. 63, no. 3, pp. 1076-1089, March 2015.

[14] J. C. Rautio, and S. Arvas, "Measurement of Planar Substrate Uniaxial Anisotropy" *IEEE Trans. Microw. Theory Tech.*, vol. 57, no. 10, pp. 2456-2463, Oct. 2009.

Digitally Assisted Analog Predistortion Technique for Power Amplifier

Karan Gumber, Praveen Jaraut, Meenakshi Rawat, Karun Rawat

Department of Electronics & Communication Engineering, Indian Institute of Technology, Roorkee 247667, India

***Abstract* — This paper presents a digitally assisted analog-predistortion scheme for linearization of high power amplifier. Taking advantage of recent available digital signal processing solutions, the proposed method reduces hardware requirement of conventional analog predistorter by alleviating the need of Vector multiplier, hybrid 90^0 coupler and delay lines. Proposed method provides flexibility in terms of digitally compensation of delay, gain and phase control of signal. The proof-of-concept of method is presented for reducing odd-order intermodulation distortion (IMD). A better performance of 11-db reduction as compared to conventional analog predistorter in terms of 3rd IMD is achieved for two-tone test signal centered at frequency 2000 MHz and 2020 MHz.**

***Index Terms* — Delay-lines, field programmable gate array, intermodulation distortion, linearization, power amplifiers, rat race coupler.**

I. Introduction

Power Amplifier (PA) is the most power-consuming device in wireless communication system. Specifically envelope varying communication signals of 3rd and 4th generation results in nonlinear behavior of PA in the saturation region. It results in in-band intermodulation distortion (IMD), increases adjacent channel interference and give rise to spectral regrowth. However, there is a trade-off between power efficiency and linearity in RF PA. Therefore, to achieve acceptable adjacent channel power ratio (ACPR) levels, linearization techniques such as predistortion are proposed in the literature. Among these, analog predistorter has advantage of compact design and no need of baseband information of incoming RF signal [1]-[3]. Essentially, this is a RF-in-RF-out predistortion system, which is desirable when baseband information is not available, such as RF repeater system.

In order to obtain linear amplitude/amplitude modulation (AM/AM) and amplitude/phase modulation (AM/PM) characteristics of PA, predistorter setup has to provide inverse characteristics of the PA. Gain compression characteristics of power amplifier are compensated by expansion characteristics of predistorter [4]. Analog Predistortion (APD) technique generates IMD terms using a pair of anti-parallel diode which in turn cancels IMD of PA by using vector multiplier (VM), 90° hybrid RF coupler, power combiners/splitters and RF delay lines. In APD technique, delay compensation is performed manually by varying the length of cable. Due to its rigidity, APD system is unable to perform when system characteristics changes with time or other factors [5], [6].

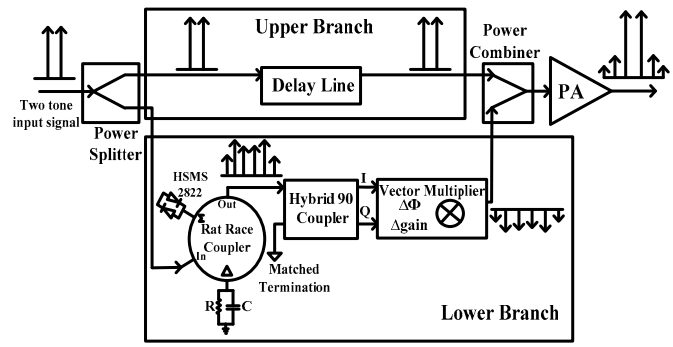

Fig. 1. Conventional Analog Predistorter

This paper presents a digitally assisted analog predistortion (DA-APD) setup for linearization of PA output that takes the advantage of low complexity, yet flexible digital control. Instead of using RF delay lines for delay compensation, it is easier to compensate delay digitally. Also gain and phase of a signal can be controlled digitally instead of using VM. In the proposed method, it also eliminates the need of 90° hybrid RF coupler which is used in APD setup in order to provide in-phase (I) and quadrature phase (Q) signals to VM. Therefore, by utilizing the DA-APD setup with RF PA, due to better control of parameters, better linearization is achieved as compared to the Cubic Predistorter Linearizer.

A. Conventional Analog Predistorter

Fig. 1 shows the schematic of a conventional Analog Predistorter. It consists of rat-race coupler (RRC), 90° hybrid RF coupler, RF delay lines, VM, power splitter and power combiner. Two-tone input signal is provided to upper and lower branches by using power splitter. Delay line in the upper branch compensates the time delay of the lower branch. Delay compensation is performed manually by varying the length of cable. In order to compensate the delay in APD, we must know the time delay in the lower branch. One of the complicated tasks in APD is to find out the time delay introduced by lower branch. After finding the exact time delay in the lower branch, it is compensated by connecting a proper length of cable in the upper branch. In the lower branch, input is given to input port of RRC. Sigma port of RRC is mounted with pair of anti-parallel HSMS 2822 varactor diode, which is used to generate odd-order IMD. Delta port is mounted with parallel RC components, which are used to eliminate main signal from, predistorted signal. The anti-parallel diode circuit and RC

978-1-5090-4514-3/16/$31.00 ©2016 IEEE

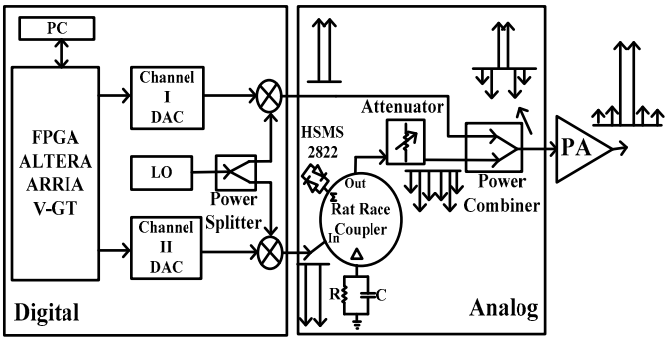

Fig. 2. Digitally assisted Analog Predistorter

circuit are combined using 180° degree hybrid coupler i.e. RRC. However, practically these main tones are not properly eliminated using RRC. The output signal from output port of RRC is given at input port of 90° hybrid RF coupler. The isolated port of 90° hybrid RF coupler is terminated by 50 Ω matched termination resistive load.

The outputs of 90° hybrid RF coupler provide in-phase (*I*) and quadrature phase (*Q*) signals at RFIN_I and RFIN_Q pins of VM. VM consist of matched pair of continuous variable gain amplifiers which is used to vary the gain and phase of input signal [7]. The output of variable gain amplifiers are summed and given at input of power combiner. The output of VM is combined with the two-tone signal of the upper-branch signal using power combiner and then fed to input of RF-PA.

B. Digitally Assisted Analog Predistorter

The proposed DA-APD applied to RF-PA is shown in Fig. 2. Analysis is proposed by two tone test signal composed of almost equal power. The two tone input signal is given as:

$$x(t) = \mathrm{Re}\left(Ae^{j\omega_1 t} + Ae^{j\omega_2 t}\right)e^{j\varphi} \tag{1}$$

$$x(t) = A\left(\cos(\omega_1 t + \varphi) + \cos(\omega_2 t + \varphi)\right) \tag{2}$$

where ω_1 and ω_2 are the frequencies, where two tones lie and φ compensates for phase delay in the lower branch. DA-APD setup composed of two channels. In channel-I, the input signal is simple two tone signal. At channel II, the input signal is 180° out of phase from the two tone input signal at channel I. Output of channel II i.e. $x_{inv.}(t)$ is given at the input of RRC. The inverted two tone test signal is provided at the input of RRC composed of equal power can be defined as:

$$x_{inv.}(t) = A\left[\cos(\omega_1 t + \pi) + \cos(\omega_2 t + \pi)\right] \tag{3}$$

$$x_{inv}(t) = -A\left(\cos\omega_1 t + \cos\omega_2 t\right) \tag{4}$$

As shown in Fig. 2, sigma port of RRC is mounted with anti-parallel diode which is HSMS 2822 varactor diode. Anti-parallel diode produces the odd order nonlinearities. The output of anti-parallel diode in RRC is given as:

$$V_{HSMS}(t) = a_1 x_{inv}(t) + a_3 x^3{}_{inv}(t) \tag{5}$$

$$V_{HSMS}(t) = -Aa_1\left(\cos\omega_1 t + \cos\omega_2 t\right) - A^3 a_3.(\cos^3\omega_1 t + \cos^3\omega_2 t)$$
$$-3A^3 a_3.\cos^2\omega_1 t\cos\omega_2 t - 3A^3 a_3.\cos\omega_1 t\cos^2\omega_2 t$$

Delta port of RRC is mounted with resistor and capacitor in order to cancel main tone that lies at frequencies ω_1 and ω_2. RRC is used to combine the anti-parallel diode circuit and RC circuit. The output of RRC is given as:

$$V_{RRC}(t) = \frac{a_3 A^3}{4}\left(\cos 3\omega_1 t + \cos 3\omega_2 t\right) - \frac{3a_3 A^3}{4}\left[\cos(2\omega_1 t + \omega_2 t)\right. \tag{6}$$
$$\left. + \cos(2\omega_1 t - \omega_2 t) + \cos(2\omega_2 t + \omega_1 t) + \cos(2\omega_2 t - \omega_1 t)\right]$$

First term in the above equation is the third order harmonics which lies at frequencies $3\omega_1$ and $3\omega_2$. Harmonics lies far away from the main tone so it can be easy filter out. Next four terms are 3rd order IMD's which lies at $2\omega_1 + \omega_2$, $2\omega_1 - \omega_2$, $2\omega_2 + \omega_1$, $2\omega_2 - \omega_1$. It is easy to remove 3rd order IMD components that lies at frequency $2\omega_2 + \omega_1$, $2\omega_1 + \omega_2$ using filters. However, if the input tones are of similar frequencies, the third-order IMD ($2\omega_2 - \omega_1, 2\omega_1 - \omega_2$) will be very close to the fundamental frequencies and cannot be easily filtered out. Third-order IMD is of most concern in narrow bandwidth applications. Second-order IMD is of greater concern in broad bandwidth applications. However, in order to remove the 3rd order IMD components that lies at frequency $2\omega_2 - \omega_1, 2\omega_1 - \omega_2$ the output of RRC is combined with original two tone input signal. Ignoring the harmonics and third order IMD that lies at $2\omega_2 + \omega_1$, $2\omega_1 + \omega_2$, combined output is given as input to RF-PA which is given as:

$$y_{PD}(t) = x(t) + V_{RRC}(t) \tag{7}$$

$$y_{PD}(t) = A\left(\cos\omega_1 t + \cos\omega_2 t\right)\cos\varphi - \delta_0\left[\cos(2\omega_1 t - \omega_2 t)\right. \tag{8}$$
$$\left. + \cos(2\omega_2 t - \omega_1 t)\right]$$

Here, the coefficient δ_0 affects the original signal and third order IMD, φ is used to compensate the phase delay that occurs in the lower branch, when inverse two tone input signal passes through RRC. Phase delay that arises in lower branch is compensated digitally by introducing delay in signal preprocessing step [8]. Moreover, phase of the signal can also be varied digitally for best IMD cancellation. The overall reduction in IMD is achieved by optimizing cubic predistorter linearizer parameters R, C and φ of DA-APD setup.

II. Measurement Setup

Fig. 3 shows the measurement setup used for characterization of PA. It consist of Altera Arria V GT Field Programmable Gate Array (FPGA), broad-band receiver (TSW1266), dual channel transmitter (TSW30SH84), local oscillator (TSW3065), RRC, attenuators, power combiners/ splitters and Class-AB PA. The transmitter contains two 16-bit digital to analog converters (DACs) and two RF modulators of frequency range 300MHz to 4GHz. FPGA is programmed using quartus software from altera. The data is guided from pre-programmed FPGA to transmitter at sampling rate of 307.2 MHz. The data is interpolated with interpolation factor of 4 and up-converted to a sampling frequency of 1228.8 MHz. The RF modulators up-

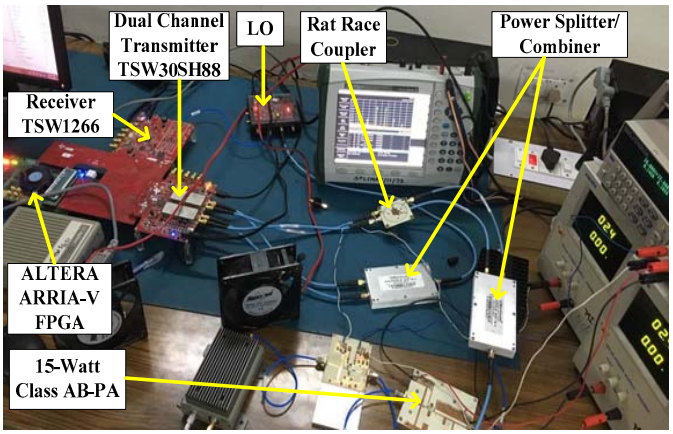

Fig. 3. Test bench for Proof-of-concept

convert the two-tone signal at frequencies centered at ω_1 = 2000 MHz and ω_2 =2020 MHz at the transmitter. Channel I contains two-tone signal and Channel II contains phase-shifted (180+phase change due to delay) two-tone signal, which is provided to the input of RRC. The output of RRC is combined with two tone signal of channel I using power combiner and then fed to input of PA which is followed by attenuator. For establishing the proof of concept, a 15-W Class-AB PA, which is driven by 10-W driver PA.

III. Experimental Results

The DA-APD is digitally optimized used for reducing the intermodulation distortion in PA. First simulation of RRC mounted with HSMS-2822 and RC circuit has been carried out in Agilent 2009 ADS. For best optimized values of R= 120 Ω and C= 1 pF, simulation results shows that RRC is able to cancel main tone signal and generate odd-order IMD. Resistor and Capacitor of above-mentioned values are mounted on delta port of RRC. Fig.4 shows the output power spectra of a 15-W Class-AB PA driven by two tone signal located at frequencies ω_1 and ω_2. The output contains odd order IMD's located at frequencies 1960 MHz (IM5), 1980 MHz (IM3), 2040 MHz (IM3), and 2060 MHz (IM5).

Fig. 5 shows the output power spectra of 15-W Class-AB PA cascaded with DA-APD setup. Experimental results shows that DA-APD setup linearizes 15-W class AB PA and reduces IMD_3 approximately by 11 dB. It has been validated experimentally that a 50dB ACLR improvement is achieved using the proposed DA-APD setup.

IV. Conclusion

A new digitally assisted predistortion method has been presented and validated. An analysis of DA-APD circuit design and experimental results has been presented. We have developed a DA-APD linearizer that can effectively control IM3 and IM5 and applied to the linearization of high power RF

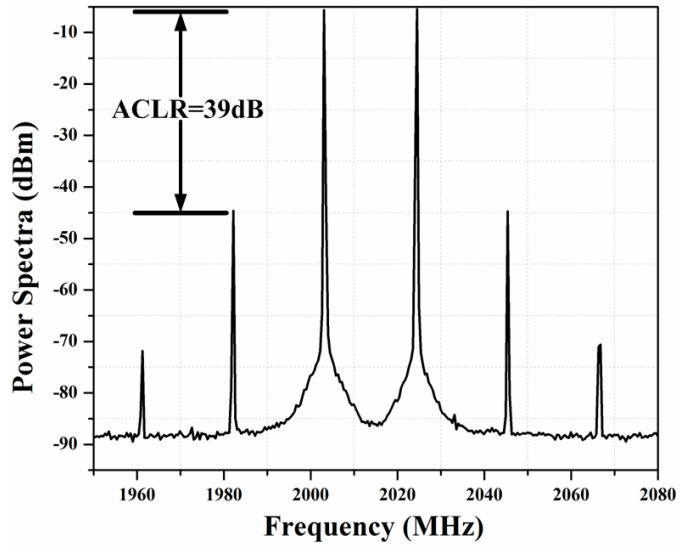

Fig. 4. Output of PA without DA-APD setup

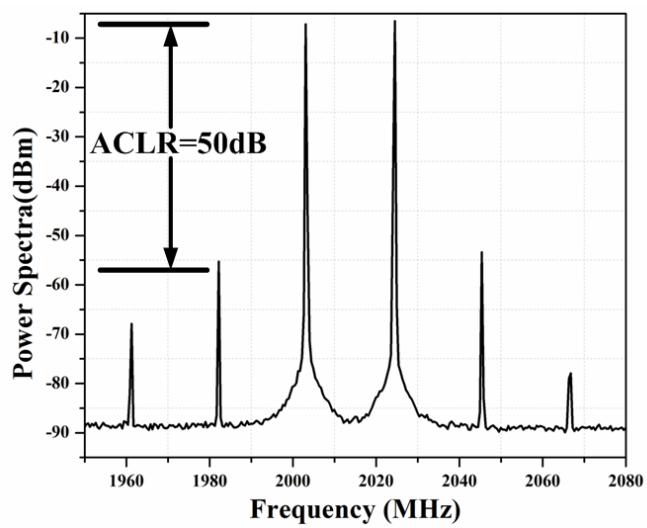

Fig. 5. Output of PA with DA-APD setup

amplifier. This setup compensates for nonlinearities and effectively reduces adjacent channel leakage ratio (ACLR). About 11-dB improvement of 3rd IMD was achieved from two tone signal, which is better than its complete analog counterpart. In the proposed setup, delay compensation is performed digitally by varying the phase angle of two tone input signal.

Acknowledgement

The authors would like to thank Dr. Karun Rawat and Girish Chandra Tripathi for their valuable suggestions. This work was supported in part by the Indian Institute of Technology, Roorkee, India under Institute Grant FIG/ECD/100676, and Defence Research and Development Organization (DRDO), India under Grant ERIP/ER/1400477/M/01.

REFERENCES

[1] J. Yi, Y. Yang, M. Park, W. Kang, and B. Kim, "Analog predistotion linearizer for high power RF amplifiers," *IEEE Trans. Microwave Theory & Tech.,* vol. 48, no. 12, December 2000.

[2] W Woo, M.D Miller, and J.S Kenney, "A hybrid digital/ RF envelope predistortion linearization system for power amplifier," *IEEE Trans. Microwave Theory & Tech.,* vol. 53, no. 1, December 2005.

[3] Y. Yang, Y. Y. Woo, and B. Kim, "New predistortion linearizer using low-frequency even-order intermodulation components," *IEEE Trans. Microwave Theory & Tech.,* vol. 50, no. 2, pp. 446-452, February 2002.

[4] P. B. Kenington, *RF and Baseband Techniques for Software Defined Radio*, Artech House, Inc., Norwood, MA, 2005.

[5] K. H. Kim, G. B. Kim, S. W. Hwang, S. H. Lee, and D. Ahn, "A wide dynamic range analog predistortion type linearizer using self cancellation scheme," *IEEE Microw. Wireless Compon. Lett.,* vol. 15, no. 10, October 2005.

[6] C, A. Cagri, and A. Tuncay, "Optimization of analog cubic predistorter for multicarrier communication system," *International Conf. On Electrical and Electronics Engineering (Eleco2007),* Session D4 Communication Theory and Systems, Bursa, 2007.

[7] K. Rawat, M. Rawat and F.M. Ghannouchi, "Compensating I-Q imperfections in hybrid RF/ digital predistortion with adapted look up table implemented in FPGA," *IEEE Trans. Circuits Syst. II: Express Briefs,* vol. 57, no. 5, pp. 389-393, May 2010.

[8] H. Yu, V. Ratnasamy, P. Roblin, M. Rawat and C. Xie, "Automatic feed-forward cancellation of modulated harmonic," *86th ARFTG. Microw. Meas. Conf.*, Dec. 2015.

Wideband Impedance-varying *N*-way Wilkinson Power Divider/Combiner for RF Power Amplifiers

Osama Hussein[1], Khair Al shamaileh[2], Vijay Devabhaktuni[1], and Peter Aaen[3]

[1]University of Toledo, OH, US, [2]Purdue University Northwest, IN, US, [3]University of Surrey, Guildford, UK

***Abstract* — We propose a compact wideband multi-way power divider/combiner with planar structure for applications to RF power amplifiers (PAs). Uniform transmission lines in the conventional divider are replaced with non-uniform transmission lines (NTLs), which are governed by a truncated Fourier series. An optimization-driven framework is employed in even-mode analysis to obtain the coefficients of the NTLs considering predefined operating bands, whereas three isolation resistors are optimized in the odd-mode analysis to achieve optimal isolation and output port matching over the design bandwidth. For verification purposes, a 4–10 GHz 3-way divider is simulated, and measured. Simulations and measurements are in close proximity and show input/output ports matching of better than –10 dB and transmission of –4.9 ±1 dB across the design bandwidth.**

***Index Terms* — multi-way power divider, non-uniform transmission lines (NTLs), power amplifiers (PAs), power combiner, wideband Wilkinson power divider (WPD).**

I. Introduction

Power dividers/combiners are widely used fundamental front-end components in a variety of microwave/millimeter wave systems, power amplifiers (PAs), mixers, and antenna feeding networks. PAs have applications that span wireless and radio communications equipment, phased array radar modules, unmanned aerial vehicles (UAVs), and electromagnetic compatibility (EMC) testing [1]-[5]. PAs can also be used in communication systems measurements such as tests of intermodulation, adjacent channel power, multi-tone, and high signal levels. However, PAs have limitations, especially for applications where a high RF amplification gain is required. To overcome this, a power combiner can be used to combine the individual powers from multiple lower power PAs. Such a network has the advantages of: 1) graceful degradation reliability characterized by the accommodation of the failure of a single PA without a total loss of the transceiver/transponder power [6], 2) it is less expensive and complex to manufacture moderate-power PAs than high-power PAs, and 3) lower power PAs can be biased to operate in the linear region, resulting in the reduction of the intermodulation distortion and undesired harmonics.

Many power dividers/combiners for large operating bandwidths, high efficiency, high isolation, and small size have been proposed in literature. The Wilkinson power divider (WPD) or combiner, proposed by E. Wilkinson in 1960 [7], is widely used in front-end microwave subsystems due to its ease of design and fabrication, high isolation between its ports, as well as perfect matching at all ports. Port isolation is widely regarded as an asset in RF power combining, as it can be used to suppress odd mode instability between the combined amplifiers [8]. This alone often explains the preference of Wilkinson type combiners over other dividers/combiners in microwave PA networks. Accordingly, broadening the operating bandwidth while maintaining the same desired electrical features are of utmost importance. A variety of designs have been proposed [9]-[13], however, the major drawbacks are the increased physical size, the use of reactive components, and the bulky 3D geometries.

In this paper, a general procedure to design and characterize a NTLs wideband multi-way planar Wilkinson power divider/ combiner is presented. The proposed device is modeled and simulated for equal-split division. Then, the input and output ports can be reversed to enable power combining rather than division. Thereafter, the phases of the transmission parameters are measured to verify in-phase functionality.

The article is organized as follows: Section II discusses the design procedure of the proposed wideband NTL multi-way WPD. Simulations and measurements of a wideband 3-way prototype is presented in Section III. Finally, conclusions are given in Section IV.

II. Multi-way WPD Design

A schematic diagram of the proposed wideband equal-split NTL divider is shown in Fig. 1. The *N*-way divider can be reduced to its equivalent 2-way model [14]. Hence, the even-odd mode analysis will be adopted.

To reduce the *N*-way divider to its equivalent 2-way model illustrated in Fig. 2, the first branch is assumed to be the *n-th* branch with 1/*N* fraction of total input power, whereas the other branch is in turn the sum of power ratios of the rest of the *N*–1 branches; or in other words, (*N*–1)/*N*.

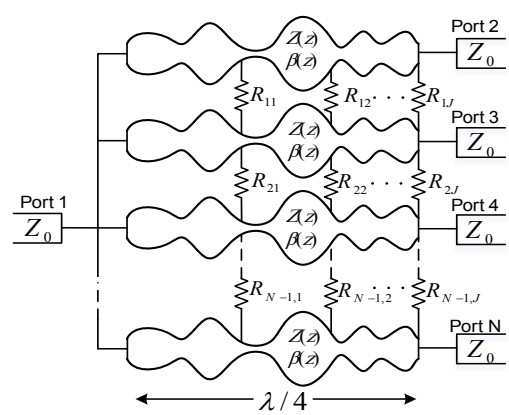

Fig. 1. A Schematic diagram of a wideband NTL *N*-way WPD.

978-1-5090-4514-3/16/$31.00 ©2016 IEEE

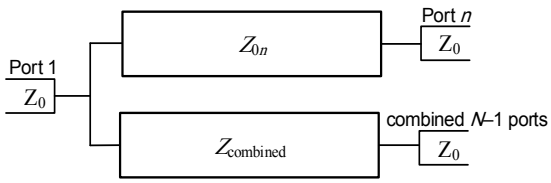

Fig. 2. A 2-way equivalent model of the N-way WPD.

Following the procedure presented in [14], Z_{0n} is found to be equal to 103 Ω. Once the characteristic impedance of the *n-th* branch is determined, the process is iterated until the characteristic impedances of all the N original branches are obtained. In this context, the equivalent 2-way model is developed only once as the power is split equally between the N output ports (i.e., same characteristic impedances Z_{0n} for all N branches).

A. Even Mode Analysis

The even mode equivalent circuit for the proposed N-way divider is shown in Fig. 3. The NTL has a length d with a varying characteristics impedance $Z(z)$ and propagation constant $\beta(z)$, and matches a source impedance Z_s to a load impedance Z_l. The isolation resistors $R_{1j}/2$ (j=1,2,3) are terminated with an open circuit as a result of the symmetric excitation at the two equivalent output ports. To design the NTL, the magnitude of the reflection coefficient, |Γ|, should be zero (or very small) over the frequency range of interest. |Γ| at the input port is expressed in terms of Z^e_{in} shown in Fig. 3, where Z^e_{in} is calculated after obtaining the *ABCD* parameters of the NTL.

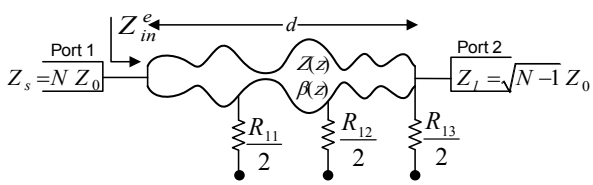

Fig. 3. 2-way equivalent even mode circuit of the proposed NTL N-way WPD.

The *ABCD* parameters of the wideband matching NTL are obtained by subdividing it into K=50 uniform short segments each of length Δz. The *ABCD* matrix of the whole NTL is obtained by multiplying the *ABCD* parameters of each section as follows [15]:

$$\begin{bmatrix} A & B \\ C & D \end{bmatrix}_{Z(z)} = \begin{bmatrix} A_1 & B_1 \\ C_1 & D_1 \end{bmatrix} \cdots \begin{bmatrix} A_i & B_i \\ C_i & D_i \end{bmatrix} \cdots \begin{bmatrix} A_K & B_K \\ C_K & D_K \end{bmatrix}. \quad (1)$$

where the *ABCD* parameters of the ith segment are [15] (assuming lossless transmission lines):

$$A_i = D_i = \cos(\Delta\theta)\,, \quad (2.a)$$

$$B_i = Z^2((i-0.5)\Delta z)\; C_i = jZ((i-0.5)\Delta z)\sin(\Delta\theta)\,, \quad i = 1, 2, \ldots, K\,, \quad (2.b)$$

$$\Delta\theta = \frac{2\pi}{\lambda}\Delta z = \frac{2\pi}{c} f\sqrt{\varepsilon_{eff}}\,\Delta z\,. \quad (2.c)$$

where c is the speed of light and f is the center frequency of the design bandwidth. The effective dielectric constant, ε_{eff}, of each section is calculated using the well-known microstrip line formulas [15]. Furthermore, the non-uniform impedance profile is governed by a truncated Fourier series that is expressed as [16]:

$$Z(z) = Z_{0n}\exp\left(c_0 + \sum_{p=1}^{P}\left[a_p\cos\left(\frac{2\pi pz}{d}\right) + b_p\sin\left(\frac{2\pi pz}{d}\right)\right]\right). \quad (3)$$

where $Z_{0n} = (Z_s Z_l)^{0.5}$, is the characteristic impedance of the WPD branch. Thus, an optimum designed NTL has its reflection coefficient magnitude over the frequency range of interest, with an increment of Δf as close as possible to zero. Therefore, the optimum values of the Fourier coefficients can be obtained through minimizing the following error function [17]:

$$\text{Error}_{\text{in}} = \max(E^{\text{in}}_{f_1}, \ldots, E^{\text{in}}_{f_m} \ldots, E^{\text{in}}_{f_M})\,. \quad (4)$$

where

$$E^{\text{in}}_{f_m} = |\Gamma_{in}(f_m)|^2\,. \quad (5.a)$$

$$\Gamma_{in}(f_m) = \frac{Z^e_{in}(f_m) - Z_s}{Z^e_{in}(f_m) + Z_s}\,. \quad (5.b)$$

$$Z^e_{in}(f_m) = \frac{A(f_m)Z_l + B(f_m)}{C(f_m)Z_l + D(f_m)}\,. \quad (5.c)$$

The resulting $Z(z)$ should be within reasonable fabrication tolerances to guarantee easy fabrication. As such, the following physical constraint is considered in the minimization of (4):

$$Z_{\min} \le Z(z) \le Z_{\max} \quad (6)$$

To find the values of the coefficients (c_0, a_p, b_p) that minimize the bound-constrained nonlinear error function in (4) across the desired bandwidth, MATLAB function "fmincon.m" is used.

B. Odd Mode Analysis

Figure 4 shows the equivalent odd-mode circuit of the proposed divider which is used to obtain the optimum values of the isolation resistors that achieve acceptable output ports isolation and matching conditions. Due to the asymmetric excitation of the output ports, each $R_{1j}/2$ resistor will be terminated with a short circuit.

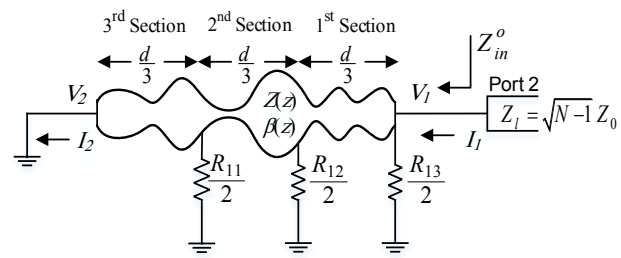

Fig. 4. 2-way equivalent odd mode circuit of the proposed NTL N-way WPD.

After determining the optimum values of the Fourier series coefficients by following the procedure described previously, the NTL transformer is subdivided into 3 sections, and the *ABCD* matrix for each section is calculated by employing (1) and (2). Then, the total *ABCD* matrix of the whole network shown in Fig. 4 can be calculated as follows [17]:

$$[ABCD]_{\text{Total}} = [ABCD]_{\frac{R_{13}}{2}} \cdot [ABCD]_{\text{1st Section}} \cdot [ABCD]_{\frac{R_{12}}{2}} \cdot [ABCD]_{\text{2nd Section}} \cdot [ABCD]_{\frac{R_{11}}{2}} \cdot [ABCD]_{\text{3rd Section}} \quad (7)$$

The locations of the resistors are distributed uniformly. Finally, as illustrated in Fig. 4, the following equation can be written:

$$\begin{bmatrix} V_1 \\ I_1 \end{bmatrix} = \begin{bmatrix} A & B \\ C & D \end{bmatrix}_{\text{Total}} \begin{bmatrix} V_2 \\ I_2 \end{bmatrix}. \quad (8)$$

Setting V_2 in (8) to zero, and solving for V_1/I_1, one obtains:

$$\frac{V_1}{I_1} = \frac{B}{D} = Z_{in}^{o}. \quad (9)$$

For perfect output port matching, the following condition should be satisfied:

$$\Gamma_{out}(f_m) = \frac{Z_{in}^{o}(f_m) - Z_0}{Z_{in}^{o}(f_m) + Z_0}. \quad (10)$$

where f_m (m = 1,2,…,M) denotes the frequencies at which (10) is calculated. In this context, Δf is chosen to be 0.2 GHz. So, for a perfect output ports matching over the desired range, the following error should be minimized [17]:

$$\text{Error}_{\text{out}} = \max(E_{f_1}^{\text{out}}, \ldots E_{f_m}^{\text{out}} \ldots E_{f_M}^{\text{out}}). \quad (11.a)$$

where

$$E_{f_m}^{\text{out}} = |\Gamma_{out}(f_m)|^2. \quad (11.b)$$

This optimization problem is solved keeping in mind that R_{11}, R_{12}, and R_{13} are the optimization variables to be determined.

III. Simulations and Measurements

In this section, based on the design procedure presented in II, a design example of a 3-way equal split WPD with fractional bandwidth of 86% is simulated, fabricated and measured. The design example is carried out using RO4003C substrate with a thickness of 0.813 mm, relative permittivity of 3.55, and loss tangent of 0.0027. The length of each NTL transformer of the proposed WPD is set to 10 mm. The characteristic impedance of the conventional 3-way WPD arm, Z_{0n}, is calculated in II and is found to be equal 103 Ω. Figure 5 shows a photograph of the fabricated power divider.

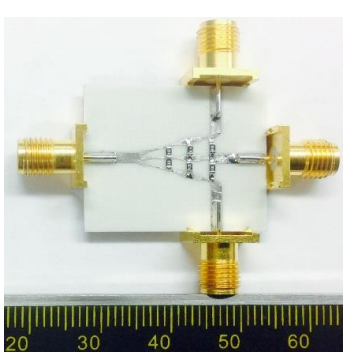

Fig. 5. Photograph of the fabricated 3-way WPD structure.

Simulations were obtained using HFSS, which is a full-wave EM simulator, whereas measurements were made with an HP 8720B vector network analyzer (VNA). Short-open-load-thru calibration was performed to the two ports of the VNA using a 3.5 mm HP/Agilent 85052A mechanical calibration kit. First, port 1 of the VNA was connected to an open-circuit standard and calibrated. Then, it was connected to a short-circuit standard and calibrated. Finally, it was connected to a broadband 50 Ω matched load for load calibration. The same process was repeated for port 2 of the VNA. Thru calibration was made by connecting the two VNA ports together to compensate for the losses due to cables and connectors.

After a two-port calibration was performed, input/output matching parameters of the proposed divider/combiner were measured by connecting VNA port 1 to the divider's port of interest, while terminating the remaining ports with a matched load. Transmission parameters were measured by connecting VNA port 1 to the input port of the proposed divider and VNA port 2 to one of the output ports; whereas the rest of the divider's ports were terminated with a matched load. Figures 6 and 7 illustrate the resulting simulated and measured scattering parameters.

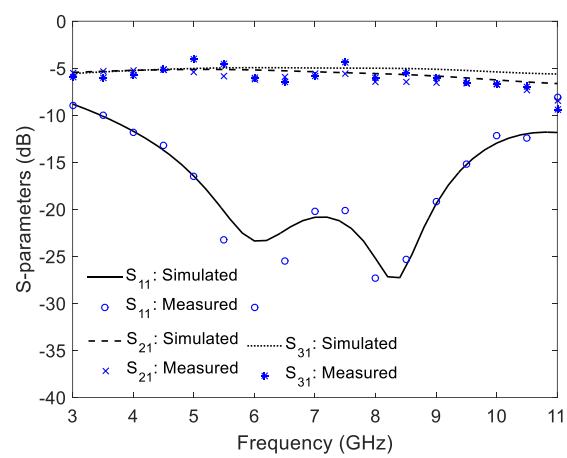

Fig. 6. Simulated and measured *S*-parameters of the proposed divider.

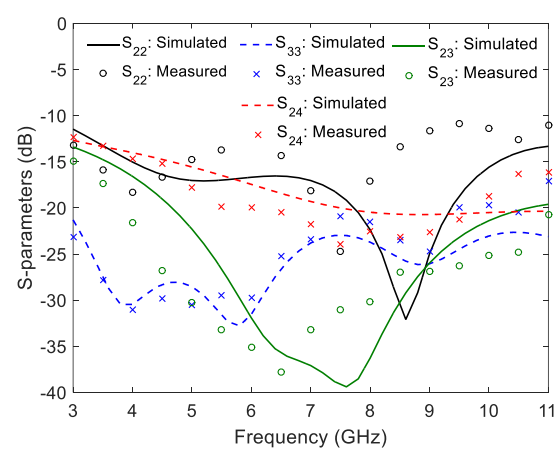

Fig. 7. Simulated and measured *S*-parameters of the proposed divider.

As shown in Fig. 6, simulation and measurement results of the input port matching are below –12 dB over the 4–10 GHz band,

whereas the transmission parameters are equal to –4.9±1 dB over the assigned band. Output ports matching and isolation parameters are in good agreement and are all below –11 dB over the assigned band as shown in Fig. 7. The small discrepancies between simulated and measured results are thought to be due to the fabrication process and measurement errors.

Measured group delays of the fabricated divider are depicted in Fig. 8. Measured results show almost a constant response of 0.18 ns for both S_{21} and S_{31} over the 4–10 GHz band (group delay of S_{41} = group delay of S_{21} due to structural symmetry).

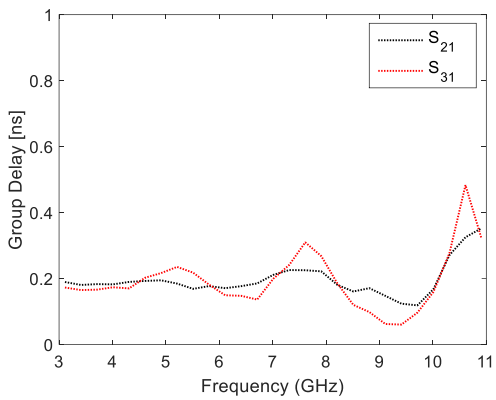

Fig. 8. Measured group delays of the proposed 3-way divider.

Figure 9 shows the measured magnitude and phase imbalances for the proposed equal-split in-phase divider. Measured magnitude imbalance equals to ±0.37 dB, whereas the phase imbalance is ±5.4° over the design bandwidth. Such results indicate an excellent symmetry of the fabricated layout and hence the proposed device can operate as a power combiner as desired.

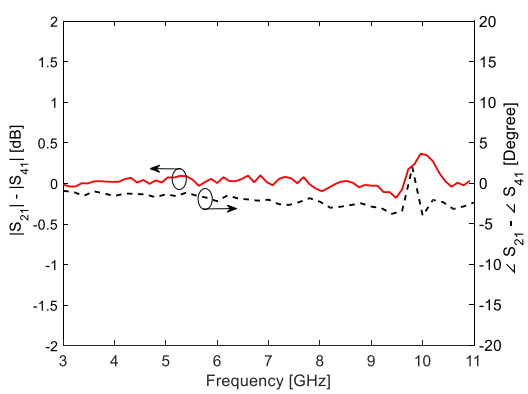

Fig. 9. Measured magnitude and phase imbalances of the proposed 3-way divider.

IV. Conclusion

This paper presented a general design of *N*-way wideband power divider/combiner that can be used in PAs which are a fundamental component in a variety of wireless communication systems. A combining technique was used to reduce the *N*-way divider to its equivalent 2-way model. Then, the even and odd mode analysis were used to obtain the NTLs and the optimized values of the isolation resistors, respectively. For verification purposes, 3-way power divider/combiner with fractional bandwidth of 86% was fabricated and measured. The good agreement between both simulation and measurement results over the assigned frequency band proves the validity of the design procedure.

References

[1] V. Bridier, D. Ducatteau, M. Olivier, H.-J. Simon, F. Graux, P. Eudeline, and G. Dambrine, "Nonlinear measurement dedicated to non periodic pulse train for radar power amplifier characterization," *2014 IEEE MTT-S Int. Microwave Symp.*, pp. 1-4, June 2014.

[2] S.J.C.H. Theeuwen, H. Mollee, "S-band radar LDMOS transistors," *EuMIC 2009 Europ. Microwave Integ. Cir. Conf.*, pp. 53-56, Sept. 2009.

[3] T. Munehiro, J. Kobayashi, J. Matsuoka, M. Yoshida, S. Kainuma, and Y. Ueda, "Development of an X-band 800W pulsed mini-TWT for active phased array radar modules," *IEEE Int. Vacuum Electro. Conf.*, pp. 99-100, April 2014.

[4] A. C. Paolella, "A new high efficiency, high power transmitter system for wireless communications," *MILCOM 2005 IEEE Military Comm. Conf.*, vol. 2, pp. 1309-1313, Oct. 2005.

[5] L. Lin, L. Zhou, Y. Zhu, Y. Hua, J.-F. Mao, W.-Y. Yin, "Improvement in cavity and model designs of LDMOS power amplifier for suppressing metallic shielding cover effects," *IEEE Trans. Electromag. Compatibil.*, vol. 58. no. 5, pp. 1617-1628, May 2016.

[6] R. N. Simons, E. G. Wintucky, and C. T. Chevalier, "High-efficiency Ka-band waveguide two-way asymmetric power combiner," *Int. J. High Speed Electron. and systems*, vol. 20, no. 03, pp. 405-415, September 2011.

[7] E. Wilkinson, "An N-way hybrid power divider," *IEEE Trans Microwave Theory Tech*, vol. 8, no. 1, pp. 116-118, January 1960.

[8] S. C. *Cripps, RF Power Amplifiers for Wireless Communications*, Artech House, 2006.

[9] A. A. M. Saleh, "Planar electrically symmetric n-way hybrid power dividers/combiners," *IEEE Trans Microwave Theory Tech*, vol. 28, no. 6, pp. 555-563, Jun 1980.

[10] D. Hawatmeh, K. Al Shamaileh, N. Dib, and A. Sheta, "Design and analysis of a 3-way unequal split ultra-wideband Wilkinson power divider," *Int. J. Electronics*, vol. 100, no. 8, pp. 1062-1071, Oct. 2012.

[11] J. Zhou, K. A. Morris, and M. J. Lancaster, "General design of multiway multisection power dividers by interconnecting two-way dividers," *IEEE Trans Microwave Theory Tech*, vol. 55, no. 10, pp. 2208-2215, Oct. 2007.

[12] A. Wentzel, V. Subramanian, A. Sayed, and G. Boeck, "Novel broadband Wilkinson power combiner," *2006 36th European Microwave Conf.*, pp. 212-215, Sept. 2006.

[13] C. Wang, W. Che, and P. Russer, "High-isolation multiway power dividing/combining network implemented by broadside-coupling SIW directional couplers," *Int. J. RF Microwave Computer-Aided Eng,*, vol. 19, no. 5, pp. 577-582, Sept 2009.

[14] A. M. Qaroot, and N. I. Dib, "General design of N-way multi-frequency unequal split planar Wilkinson power divider," *Prog. Electromagnetic Res. C*, vol. 14, pp. 115-129, 2010.

[15] D. Pozar, *Microwave Engineering*, New York: J. Wiley & Sons, 2005.

[16] K. Alshamaileh, V. Devabhaktuni, and N. Dib, "Impedence-varying broadband 90° brach-line coupler with arbitrary coupling levels and higher order harmonic suppression," *IEEE Trans. Compon. Pack. Manuf. Technol.*, vol. 5, no. 10, pp. 1507-1515, Oct. 2015.

[17] K. Shamaileh, M. Almalkawi, V. Devabhaktuni, N. Dib, B. Henin, and A.Abbosh "Fourier-based transmission line ultra-wideband Wilkinson power divider for EARS applications," 2013 *IEEE 56th Int. Midwest Symp. Circuits Syst.*, pp. 872-875, Aug. 2013.

Cross-correlation method measurement of Error Vector Magnitude and application to power amplifier non-linearity performances

Jacques Sombrin[1,2], Pierre Medrel[3]

[1] Labex Sigma-Lim, University of Limoges, France, [2]TéSA Laboratory, Toulouse, France

[3]XLIM, University of Limoges, France

***Abstract* — Error Vector Magnitude (EVM) is used by communication systems designers as one way to express distortions in digital communications. These distortions may come from initial modulator amplitude and phase imbalances, from linear distortions or non-linear distortions in the transmission chain. It is a good indicator of power amplifiers non-linearity. We propose to use a closed form method based on cross-correlation between input and output signal of the power amplifier as a way to measure either EVM or Noise Power Ratio (NPR). We show the small differences that exist between both measurements. We show also that it can be applied to the measurement of signal EVM at the output of a signal generator or transmission chain.**

***Index Terms* — Error Vector Magnitude, EVM, Measurement, Non-linearity, Noise Power Ratio, NPR, power amplifiers.**

I. Introduction

Error Vector Magnitude (EVM) is has been used by communications systems designers as one of the way to express distortions in digital communications. When a digitally modulated signal is generated it is no perfect and it has some differences with the reference signal that should be generated. These differences are measured by the EVM, the ratio of rms error to the reference signal average amplitude. The transmission chain will add linear and non-linear distortions to this signal and the EVM will increase. Finally, the receiver may add its own distortions.

One of the main contributors to the EVM degradation is the non-linear power amplifier in the transmitter. EVM is a good indicator of amplifier non-linearity and it can be used to assess the effect of pre-distortion or linearization on the linearity of the amplifier.

EVM is generally defined in telecommunications standards [1]-[3] together with possible methods of measurements.

These measurement methods are generally based on optimization of a complex ratio between the measured signal and a reference signal or constellation [4, 5]. These algorithms are non-convex and may lead to local minima [5]. We propose a closed form method based on cross-correlation of signals. Its closed form permits to derive mathematical properties that are difficult to get from optimization methods.

We compare EVM with other figures of merit used to measure amplifier non-linearity such as Noise Power Ratio (NPR) and Adjacent Channel Power Ratio (ACPR or ACLR).

We conclude by giving some examples of input and output signals and spectra

II. EVM measurement points in a transmission chain

The schematics next page (fig. 1) shows a transmission chain and the main points where EVM can be measured.

Classically EVM is measured by comparing the received IQ symbols (after matched filtering and optimum sampling) with the transmitted IQ symbols or the nearest IQ constellation point. The filtering, optimum time alignment, sampling and determination of the nearest constellation point is done by the receiver in the chain. The classical method defined in standards and articles [1]-[5] is based on the optimization of a complex coefficient (or gain) by which the reference signal is multiplied to obtain the minimum difference with the received signal.

EVM can also be measured by comparing the reference modulated signal and the received signal before time alignment and optimum sampling. In that case both signals must be filtered by a matched filter. Generally, this filter also respects one of Nyquist conditions to give as small as possible inter-symbol interference (ISI). For the received filter this maybe already done in the receiver.

EVM can be measured by comparing RF signals at the input and output of the amplifier (or the pre-distorted amplifier). In that case the sampling is generally done at frequency higher than the symbol rate frequency and both signals must be filtered by the matched filter.

III. EVM measurement of a signal

The second schematic (fig. 2), is used to measure signal EVM at the output of a generator. No reference signal exists generally. Classical measurement methods are called data-aided and non-data-aided depending if they know the sequence of symbols that has been sent. In all cases it is necessary to know the constellation and symbol rate. In addition, APSK constellations may have different radii depending on the error correction ratio.

If the transmitted data is not known, the receiver must regenerate this data before computing the differences with the received signal. This is done by choosing the nearest point in the constellation. A classical receiver would do the same.

In that case, some errors exist in the regenerated signal and the EVM measurement is optimistic for high values of EVM or low values of signal to noise ratio.

978-1-5090-4514-3/16/$31.00 ©2016 IEEE

We can go a step further in the receiver and correct errors before generating an ideal reference signal. In that case the EVM is practically identical to the data-aided EVM when in quasi-error free mode, bit error rate < 10^{-12}.

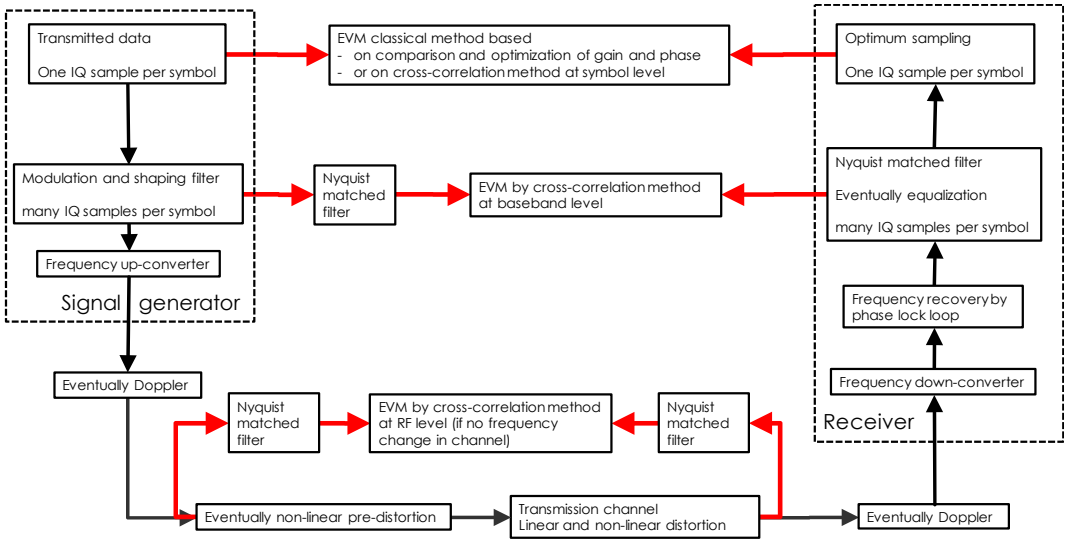

Fig. 1. Transmission chain and main points where the EVM can be measured

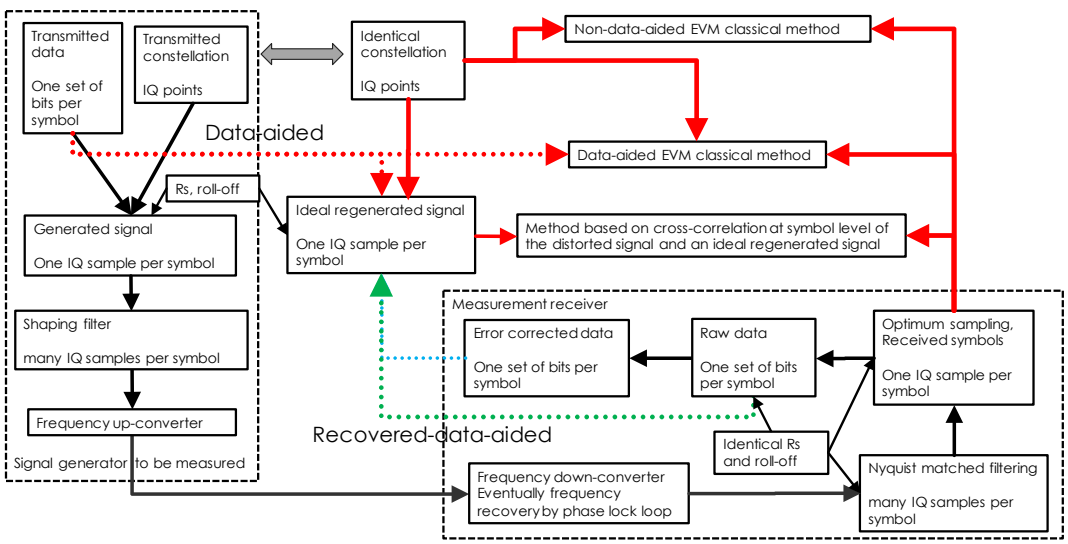

Fig. 2. Measurement of signal EVM at the output of a signal generator

IV. CROSS-CORRELATION METHOD

When the reference signal is known or regenerated it is possible to compute the EVM from a cross-correlation from reference and received signals. This has been shown in [6] and is similar to cross-correlation measurement of NPR in [7] and uses the concept of equivalent gain proposed in [8] after theoretical work [9]-[11].

In summary, we compute an equivalent gain (a complex number) as:

$$g = \frac{\max E\{x_{meas} \cdot x_{ref}^*\}}{\max E\{x_{ref} \cdot x_{ref}^*\}} \quad (1)$$

where x_{meas} is the measured signal and x_{ref} is the reference signal. The expectations in this equation can be computed as the maximum of the cross-correlation of two signals.

$$E(y.x^*)(\tau) = (x \star y)(\tau) = \int y(t+\tau).x^*(t)dt \quad (2)$$

The maximum of the reference (denominator) is always obtained at time t=0. When the measured signal is time

aligned with the reference signal, the maximum of the cross-correlation occurs also at time t=0.

The cross-correlation can also be obtained from the inverse Fourier transforms of the signals $X(f)$ and $Y(f)$ as:

$$E(y.x^*)(\tau) = \mathcal{F}^{-1}\{Y(f).X^*(f)\} \quad (3)$$

In that case, the inverse Fourier transform in equation 3, at time t=0, resolves to the integral of the product of spectra:

$$E(y.x^*)(0) = \int y(t).x^*(t)dt = \int Y(f).X^*(f)df \quad (4)$$

The equivalent gain can then be expressed as:

$$g = \frac{\int Y(f).X^*(f)df}{\int X(f).X^*(f)df} \quad (5)$$

From the equivalent gain, it is easy to compute the noise or root mean square (rms) error in the measured signal compared to the reference signal as:

$$n(t) = x_{meas}(t) - g.x_{ref}(t) \quad (6)$$

The definition of gain g ensures that the noise is un-correlated to the reference signal, that is:

$$E(n.x^*) = E\{x_{meas} \cdot x_{ref}^*\} - g.E\{x_{ref} \cdot x_{ref}^*\} = 0 \quad (7)$$

It can also be shown that the power of the measured signal is the sum of the power of the part proportional to the reference signal and the power of the noise:

$$E\{x_{meas} \cdot x_{meas}^*\} = E\{n.n^*\} + g.g^*.E\{x_{ref} \cdot x_{ref}^*\} \quad (8)$$

From this equation, we can deduce that the gain obtained is optimum in that it will give the minimum value for the noise power as any other value that would not have null correlation with the reference signal would have higher power.

The EVM is computed from the ratio of noise power and signal power in equation 7 as:

$$EVM = \frac{E\{n.n^*\}}{g.g^*.E\{x_{ref} \cdot x_{ref}^*\}} \quad (9)$$

From the equations used, it is the minimum value that can be obtained from the measured and reference signals.

This replaces the gain and phase optimization that are generally given as methods to compute the EVM in standards and articles [1-5] by a closed form result.

V. Application to sampled signals

When using sampled signals, the expectation can be computed as:

$$E(y.x^*)(k) = \sum_{m=0}^{N-1} y(m+k).x^*(m) \quad (10)$$

Then:

$$g = \frac{\max_k \sum_{m=0}^{N-1} x_{meas}(m+k).x_{ref}^*(m)}{\max_k \sum_{m=0}^{N-1} x_{ref}(m+k).x_{ref}^*(m)} \quad (11)$$

When both signals have been time aligned so that the maximum of each sum occurs at k=0, we have:

$$g = \frac{\sum_{m=0}^{N-1} x_{meas}(m).x_{ref}^*(m)}{\sum_{m=0}^{N-1} x_{ref}(m).x_{ref}^*(m)} \quad (12)$$

As in the case of continuous signals, we can use Fourier transform, in this case discrete Fourier transform (DFT) and the fast Fourier transform (FFT) algorithm to obtain the spectra of signals. The gain can be expressed as:

$$g = \frac{\sum_{m=0}^{N-1} X_{meas}(m).X_{ref}^*(m)}{\sum_{m=0}^{N-1} X_{ref}(m).X_{ref}^*(m)} \quad (13)$$

VI. Time alignment, coarse and fine

As presented in the preceding sections, the measured signal must be time aligned with the reference signal. It has been found that the simplest method is to use the cross-correlation itself to get the value of time shift that must be applied to the measured signal (generally negative) so that the maximum of the cross-correlation occurs at time t=0.

For sampled signal, a precision finer than one sample period may be needed in some cases.

A simple method consists in extending the spectra of signals with null samples. This increases the sampling frequency and reduces the sampling period. Intermediate samples are inserted in the signals. They could also be obtained through the Whittaker–Shannon interpolation formula or sinc interpolation to construct a continuous signal from its discrete samples provided it is bandlimited.

It is not necessary to interpolate both signals, this is necessary only on the cross-correlation itself.

Thus the cross-correlation method replaces also the time alignment methods that are based on optimization in classical method of EVM measurement.

VII. Shaping and matched filters

As is shown on the figures, some signals need to be filtered through a shaping or a matched filter before comparison.

A matched filter has an impulse response inverted in time with respect to that of the shaping filter used in transmission. This ensures an optimum reception and best signal to noise ratio in a linear channel with additive white Gaussian noise (AWGN). The frequency response of the matched filter is then the complex conjugate of the frequency response of the shaping filter.

The frequency response of the cascaded filters is the product of the two frequency responses and is then real.

The impulse response of the cascade filters is the inverse Fourier transform of this product and is equal to the self-correlation of the impulse response of the shaping filter. It is symmetrical in time.

In addition, it is necessary for these two filters to respect the Nyquist criterion to minimize inter-symbol interference (ISI). The criterion states that the impulse response of the cascaded filters is equal to 1 at time t=0 and equal to 0 at all times that are multiples of the symbol period.

In the frequency domain, it states that a sum of frequency responses of the cascaded filters, shifted in frequency by multiples of the symbol rate, is constant.

One of the well-known shaping and matched filter in digital communication is the square root raised cosine filter. The frequency response of the cascaded shaping and matched filters is a raised cosine filter. Its frequency response is symmetric with respect to point of amplitude 1/2 at frequencies +/- half the symbol rate, so that it respects the Nyquist criterion.

Shaping and matched filters can be applied easily to a signal in the frequency domain by multiplying the spectrum of the signal by the frequency response of the filter.

VIII. Equalization

In some cases, the transmission channel is frequency selective and it may distort the signal too much for correct reception. New standards [3] take this problem into account and ask that the EVM be measured after equalization of the transmission channel by the receiver.

Equalization will increase the value of the maximum of the cross-correlation and decrease the rms error. Both effects tend to decrease the EVM. It can be optimized by maximizing the cross-correlation maximum.

Equalization must be normalized to keep constant the receiver noise bandwidth.

IX. Results

This method is used by CNES (French Space Agency), TéSA Laboratory and XLIM Laboratory at Université de Limoges for simulation and measurements.

An example of spectra of reference signal, measured signal and extracted noise for a 16 QAM modulation at the output of a power amplifier is given in figure 3.

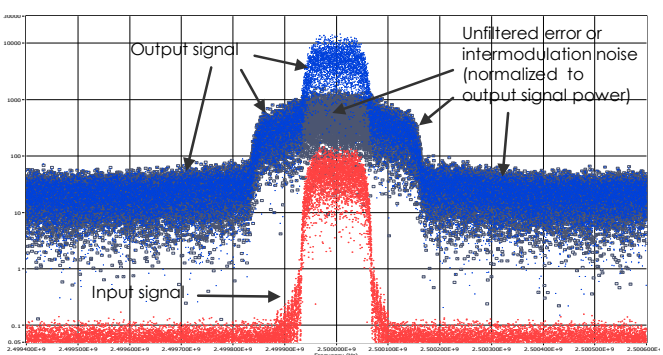

Fig. 3. Reference signal, measured signal and noise spectra

Other examples of measurements and simulations will be given at the conference. This method has been applied to DVB-S2 signals with non-linear amplifiers and linearized amplifiers and it gave errors less than 0.1 % compared to measurement results obtained with commercial equipment..

X. Conclusion

The cross-correlation method gives the EVM as a closed form result that replaces classical algorithms that are non-convex and may have local minima. It solves the time alignment problem and gives the amplitude and phase of the normalization between reference and measured signals. From this form, we can demonstrate that it gives the lowest possible value for EVM.

Acknowledgement

Work on this method was founded by CNES (French Space Agency) R and D program.

Formalization of the cross-correlation method has benefitted from discussions with the IEEE P1765 Working Group on Uncertainty in EVM and with the Glossary Subgroup.

References

[1] Wireless LAN MAC and PHY specifications, High-speed Physical layer in the 5 GHz Band, IEEE Std 802.11a−1999(R2003)

[2] Implementation guidelines for the second generation system for Broadcasting, Interactive Services, News Gathering and other broadband satellite applications, DVB A171-1, March 2015

[3] Wireless LAN MAC and PHY specifications, Amendment 4: Enhancements for Very High Throughput for Operation in Bands below 6 GHz IEEE Std 802.11ac−2013

[4] A. Mashhour and A. Borjak: "A method for computing error vector magnitude in GSM EDGE systems-simulation results", IEEE COM Letters, vol. 5, No 3, march 2001, pp. 88-91

[5] T. Jensen and T. Larsen, "Robust computation of Error Vector Magnitude for wireless standards", IEEE Trans. On Communications, Vol. 61, No. 2, February 2013, pp. 648-657

[6] J. Sombrin, "On the formal identity of EVM and NPR measurement methods: conditions for identity of EVM and NPR", Proc. Of the 41st European Microwave Conference, Manchester, 10-13 October 2011, pp. 337-340

[7] S. W. Chen, W. Panton, and R. Gilmore: "Effects of nonlinear distortion on CDMA communication systems", IEEE Trans. on Microwave Theory and Techniques, vol. 44, no 12, December 1996, pp 2743-2749

[8] D. S. Amstein, "Power division in spread spectrum systems with limiting," IEEE Trans. Communications, vol. COM-27, Mar. 1979, pp. 574-582.

[9] J. J. Bussgang, "Crosscorrelation Functions of Amplitude-Distorted Gaussian Signals," Technical Report 216 of the Research Laboratory of Electronics, M.I.T., March 26, 1952, Cambridge, Massachusetts.

[10] N. M. Blachman, "The Signal x Signal, Noise x Noise and Signal x Noise Output of a Nonlinearity," IEEE Trans. on IT, Vol. IT-14, No. 1, January 1968, pp. 21-27.

[11] R. C. Booton, Jr., "Analysis of Nonlinear Control Systems with Random Inputs," IRE Trans. on Circuit Theory, Vol. CT-1, pp. 9-18, March 1954.

A Simple Method for Transmission Lines Quality Control

Aleksandr A. Savin[1], Vladimir G. Guba[2], Olesia N. Bykova[2], Andrej Rumiantsev[3]

[1]Tomsk State University of Control Systems and Radioelectronics, Tomsk, Russia, [2]NPK TAIR, a subsidiary of Copper Mountain Technologies, Tomsk, Russia, [3]MPI Corporation, Advanced Semiconductor Test Division, Chu-Pei City, Taiwan

***Abstract* — Transmission lines take a crucial role in verifying measurement accuracy of a calibrated vector network analyzer (VNA) as well as in establishing traceability of measured *S*-parameters. Difficulties in manufacturing of long transmission lines demand verification of the test transmission line before use. This work presents a simple method for comparing characteristic impedance of a test line with the reference. Accuracy improvement over the conventional method is achieved by the differential approach and data processing in the time domain. The proposed method was verified for coaxial lines manufactured by two vendors as well as for coplanar waveguide lines from NIST reference material RM8130 up to 70 GHz.**

***Index Terms* — Vector network analyzer, transmission line, time domain gating, reflection, characteristic impedance, coplanar waveguide, coaxial waveguide.**

I. Introduction

S-parameter measurements of RF and mm-wave devices, circuits and components require accurate definition of the measurement reference plane. There is a great variety of vector network analyzer (VNA) calibration methods developed for this purpose. During the calibration procedure, a set of calibration standards with known electrical characteristics (a calibration kit) is measured, the system measurement reference impedance Z_{VNA} is defined and the measurement reference plane is located close to the device under test (DUT) terminals.

The calibrated reflection coefficient of a transmission line with the characteristic impedance Z_L=Z_{VNA} is equal to zero for negligible calibration residual errors and random measurement errors. This phenomenon is often used to identify residual errors of a calibrated VNA as well as to verify the accuracy of secondary calibration standards.

Calibration comparison method [1] calculates errors of a test (working) calibration vs. the reference calibration performed with the reference calibration kit. The alternative method from [2] processes the measurement data of the verification line in the time domain assuming Z_L=Z_{VNA}. Also, as reported in [2], it provides fast calculation of calibration residual errors.

This work presents a simple method of comparing electrical characteristics of the reference and test transmission lines. The method performs the time domain processing of the calibrated reflection coefficients of the reference and the test lines, yielding accurate estimate of difference of the line characteristic impedance.

II. Limitations of the Conventional Method

Often, characteristic impedance of a transmission line is calculated form its measured *S*-parameters with:

$$Z_L = Z_{VNA}\sqrt{\frac{(1+S_{11})(1+S_{22})-S_{21}S_{12}}{(1-S_{11})(1-S_{22})-S_{21}S_{12}}}\,, \qquad (1)$$

and, thus, the uncertainty of Z_L is defined by the measurement uncertainties of all four *S*-parameters. The dispersion σ_Z^2 of the measurement uncertainty of Z_L can be found applying the linearization method to (1):

$$\sigma_Z^2 = \sum_{i,j=1}^{2}\left(\frac{\partial Z_L}{\partial S_{ij}}\right)\left(\frac{\partial Z_L}{\partial S_{ij}}\right)^{*}\sigma_{ij}^2\,, \qquad (2)$$

where σ_{ij} – is the standard deviation of the measured S_{ij}; * – marks the complex conjugation. Here, we assumed that uncertainties of measured *S*-parameters are not correlated for simplicity reason.

We conducted an analytical experiment to evaluate the measurement uncertainty of Z_L calculated by (1) for the following conditions: the measurement uncertainties of *S*-parameters are not correlated and their standard deviation is -45 dB, the measurement reference impedance Z_{VNA}=50 Ω at both VNA ports, and the characteristic impedance of a test line is Z_L=55 Ω. The propagation constant γ of the test line was calculated for the frequency range from 50 MHz to 70 GHz with of 50 MHz steps from:

$$\gamma = j2\pi f / c \cdot \sqrt{\varepsilon_{eff}} \cdot (1 - j\tan\delta_\varepsilon)\,, \qquad (3)$$

where: f – the frequency; c – the speed of light in vacuum. We assume the following parameters for the test line: the effective dielectric constant is ε_{eff}=7, the lost tangent is tan(δ_ε)=0.01, and the line length is l=7 mm. These parameters are close to characteristics of the coplanar lines we used later in practical experiments.

The analytical experiment consisted of the following steps: simulation for *S*-parameters of the test line using defined Z_L, γ, l, (affected by measurement errors), calculation of Z_L using (1) and comparison with the initial parameter. Additionally, we calculated the standard deviation of the "measured" Z_L by the Monte Carlo method with 10^3 samples. The simulation results

978-1-5090-4514-3/16/$31.00 ©2016 IEEE

demonstrated that the measurement error of the Z_L calculated from (2) can reach 10 Ω (or 20%, Fig. 1).

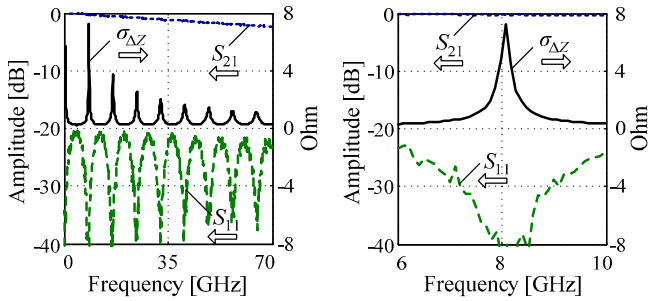

Fig. 1. Simulation results: S_{11} and S_{21} of the test line and the standard deviation of the calculated Z_L for the entire frequency range (left) and zoomed-in area (right).

Measurement uncertainties of *S*-parameters have more complex nature in practice and include systematic and random components. Calibration residual errors are frequency dependent; they impact all measured *S*-parameters and are correlated.

Also, we calculated Z_L from (1) using measured *S*-parameters data set of an experimental coplanar waveguide (CPW) line of l=7.115 mm from the reference material RM8130 [3]. Fig. 2 presents the difference ΔZ of the Z_L from the measurement reference impedance Z_{VNA} of the calibrated system. Fig. 2 gives the standard deviation $\sigma_{\Delta Z}$ of the measurement error of Z_L calculated from (2) assuming that the standard deviation of measured *S*-parameters σ_{ij} linearly increases with the frequency.

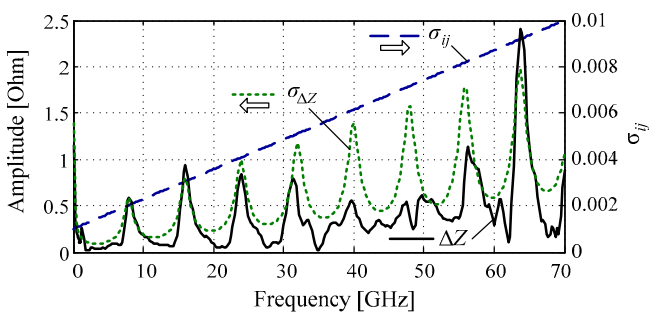

Fig. 2. Difference ΔZ of the measured characteristic impedance Z_L of the experimental CPW line from the measurement reference impedance Z_{VNA} of the calibrated system (black solid line), as well as the standard deviation $\sigma_{\Delta Z}$ of the measurement error of Z_L calculated from (2) (green dotted line) and the expected standard deviation σ_{ij} of measured *S*-parameters.

Obviously, using (1) is impractical for accurate measurement of the Z_L of an unknown line and it may lead to a significant error. The error increases with the length of the line, while it is inversely proportional to the line loss. Therefore, measurement results of the Z_L provided by the conventional method for a long coaxial line can be subject by significant errors.

III. The New Comparison Algorithm

Fig. 3 shows the measurement model of a calibrated VNA when the test or reference line is connected between its ports.

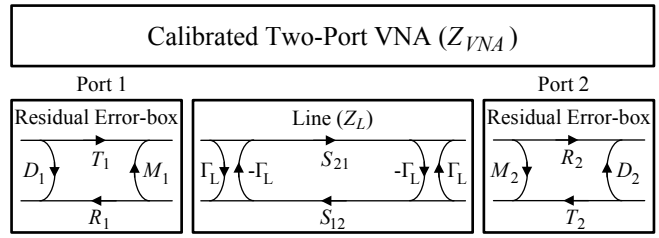

Fig. 3. The model of a two-port calibrated measurement system with a test line connected to the both VNA ports. Calibration residual error are: *D* – directivity, *M* – match, *T* – transmission tracking, *R* – reflection tracking.

The reflection coefficient Γ_L of the test line with the characteristic impedance Z_L is given by:

$$\Gamma_L = (Z_L - Z_{VNA})/(Z_L + Z_{VNA}), \quad (4)$$

where Z_{VNA} is the measurement reference impedance of the VNA.

Processing measurement results in the time domain can split reflections caused by the impedance mismatch [4, 5]. In [6], the advantages of simulations analysis of all signals were discussed. Application of this algorithm can evaluate Γ_L from measured S_{11} and S_{22}. Taking into account, that magnitude of the processing signals is relatively small, including impact of the calibration residual errors, and applying the time domain gating, we can arrive to the following estimate:

$$\hat{\Gamma}_L^{11} \approx D_1 + \Gamma_L \cdot T_1 R_1 \quad (5)$$

from measured S_{11}; or:

$$\hat{\Gamma}_L^{22} \approx D_2 + \Gamma_L \cdot T_2 R_2 \quad (6)$$

from measured S_{22}.

For two lines with Z_{L1} and Z_{L2} measured by the same VNA, we have:

$$\Delta\hat{\Gamma}_L^{11} = \hat{\Gamma}_{L1}^{11} - \hat{\Gamma}_{L2}^{11} = (\Gamma_{L1} - \Gamma_{L2}) \cdot T_1 R_1; \quad (7)$$

$$\Delta\hat{\Gamma}_L^{22} = \hat{\Gamma}_{L1}^{22} - \hat{\Gamma}_{L2}^{22} = (\Gamma_{L1} - \Gamma_{L2}) \cdot T_2 R_2. \quad (8)$$

Introducing the relative estimate $\Delta\Gamma_L$ we canceled out impact of the residual directivity *D*. Thus, the measurement error of (7) and (8) only depends on the VNA residual tracking *T* and *R*, contact repeatability and drift. It is important to note, that the impact of *T* and *R* is relatively small for most cases.

From $\Delta\Gamma_L$ given by (7) or (8) and (4), we defined the estimate of the characteristic impedance of the test lines ΔZ_L:

$$\Delta\Gamma_L = \frac{(Z_{L1}-Z_{VNA})}{(Z_{L1}+Z_{VNA})} - \frac{(Z_{L2}-Z_{VNA})}{(Z_{L2}+Z_{VNA})} \approx \frac{Z_{L1}-Z_{L2}}{2Z_{VNA}}\ ; \quad (9)$$

$$\Delta\hat{Z}_L = Z_{L1} - Z_{L2} \approx 2Z_{VNA}\cdot\Delta\hat{\Gamma}_L\ . \quad (10)$$

Usually, $Z_{L1}\approx Z_{L2}\approx Z_{VNA}$. The last was taken into account when simplifying the denominator of (9).

IV. Experimental Results

Two experiments were conducted to verify the proposed method: on-wafer and in the coaxial environment. We also expected that the accuracy of the estimate ΔZ_L should not be affected by the accuracy of the VNA calibration.

The reference material RM8130 from National Institute of Standards and Technology (NIST, USA [3]) was used in the first experiment. Measurement data of the calibration and verification elements were collected up to 70 GHz. We executed three multiline TRL[1] calibrations [7]: 1) including all calibration lines; 2) excluding the 6.565 mm long line from the calibration set (w/o L6); and 3) excluding the 19.695 mm long line from the calibration set (w/o L19). The line length is given with respect to the 550 micrometer long thru standard. Next, we analyzed two lines, L6 and L19. The time domain diagrams of S_{11} и S_{22} are shown on the Fig. 4. The local reflections are attributed to the calibration residual errors and to the change of the characteristic impedance along the measurement setup (see Fig. 3).

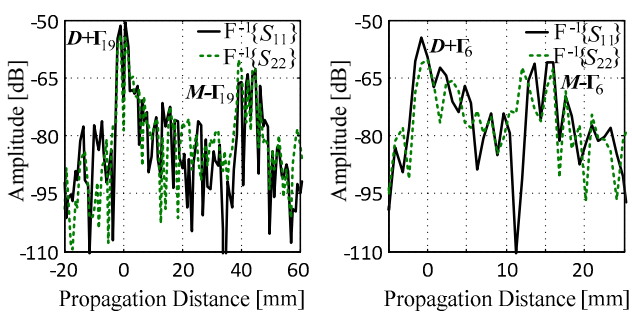

Fig. 4. The time domain diagram of S_{11} and S_{22} of the coplanar waveguide lines L19 (left) and L6 (right).

Results obtained from (7) are shown in Fig. 5. Moreover, it shows the difference in estimates for $\Delta\Gamma_L$ calculated for the three calibration schemes mentioned above (parameter "difference"). Estimates of difference of $\Delta\Gamma_L$ are less than -45 dB for all three calibrations.

Comparison for the reflection coefficients estimates and the characteristic impedance estimates of the lines L6 and L19 for one calibration scheme are given in Fig. 6. The maximum value of the magnitude of ΔZ_L is about 2 Ω for the port 1 measurements and it is about 1 Ω for port 2 measurements. It is important to note, that the reference impedance of the multiline TRL was set to the characteristic impedance of the calibration lines: $Z_{VNA}=Z_0$; i.e. it is equal to an average value Z_0 across the all lines from the calibration kit. If required, a similar analysis can be conducted at any arbitrary value of Z_{VNA} (for instance for Z_{VNA}=50 Ω) by applying the impedance transformation algorithm to the results. In this case, results will be equivalent.

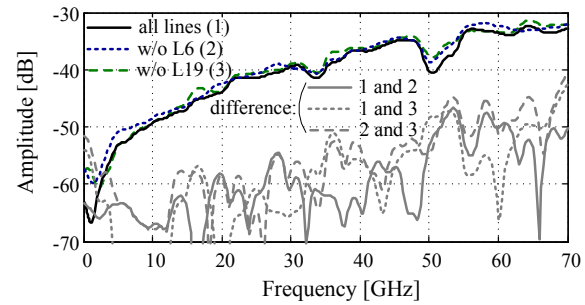

Fig. 5. Magnitude of the estimate $\Delta\Gamma_L$ of the lines L19 and L6 for three calibration schemes as well as the magnitude of the difference of $\Delta\Gamma_L$ after the time domain processing of S_{11}.

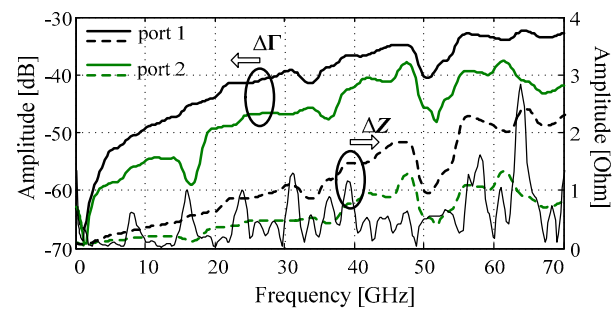

Fig. 6. The magnitude of the estimates $\Delta\Gamma_L$ (solid lines) and ΔZ_L (dash lines) of L19 and L6 for port 1 (calculated from S_{11}) and port 2 (calculated from S_{22}). The magnitude of ΔZ_L (thin black solid line) was calculated by (1).

The second experiment was performed up to 34 GHz frequency range using the coaxial 3.5 mm set of standards from Keysight Technologies. The VNA was calibrated by the SOLT[2] and the TRL calibration methods. The calibration reference impedance Z_{VNA} was set to Z_{VNA}=50 Ω in both cases.

The load standard set the SOLT calibration reference impedance. The same standard was used to define the reference impedance of the combined TRM[3]-TRL calibration at frequencies below 2 GHz. Two air lines of 16 mm long and 5 mm long were used for the TRL calibration at frequency bands from 2 GHz to 7 GHz and from 7 GHz to 34 GHz, respectively.

Two coaxial air lines from the same kit were measured afterwards: the calibration line L16 (16 mm long) and the verification line L75 (75 mm long). Additionally, we measured two test air lines made in-house: L24 (24 mm long) and L30 (30 mm long). Fig. 7 shows the $\Delta\Gamma_L$ estimate for L16 and L75 as well as the difference of this estimate for SOLT

[1] Thru-Reflect-Line

[2] Short-Open-Load-Thru

[3] Thru-Reflect-Match

and TRL (trace "difference"). The impact of the residual tracking errors on the SOLT results is well present. However, the overall difference of estimates is less than -50 dB up to 25 GHz. It is important to note, that Keysight calibration standards are specified up to 26.5 GHz only.

Similar results were observed for the in-house made lines L24 and L30 (Fig. 8). Again, residual tracking errors of the SOLT calibration reduced accuracy of the estimation. However, the difference between the SOLT and the TRL results is less than -50 dB up to 28 GHz.

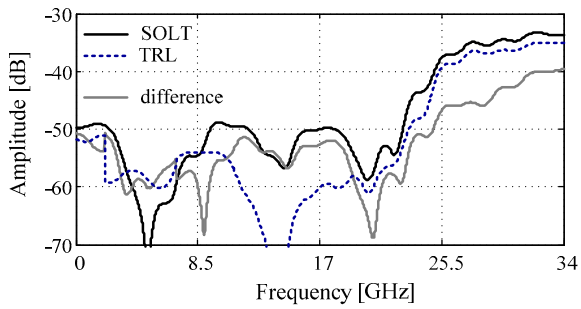

Fig. 7. The magnitude of the estimate $\Delta\Gamma_L$ for L16 and L75 for SOLT (back solid line) and TRL (dash line) calibration as well as the difference of these estimates (gray solid line).

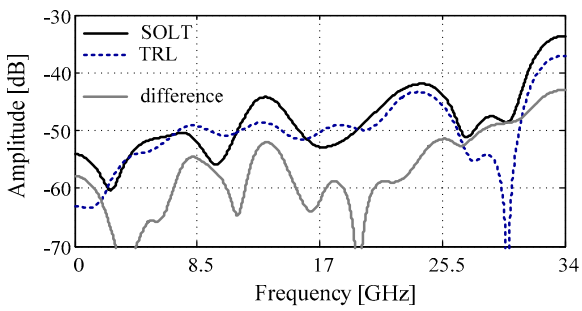

Fig. 8. The magnitude of the estimate $\Delta\Gamma_L$ for L24 and L30 for SOLT (back solid line) and TRL (dash line) calibration as well as the difference of these estimates (gray solid line).

Also, we compared estimates for L75 (the reference line) and L30 (the test line), see Fig. 9. We found that ΔZ_L was almost constant over the entire frequency range and was around 1 Ω up to 25 GHz. Note, that both lines L24 and L30 were originally specified up to 20 GHz.

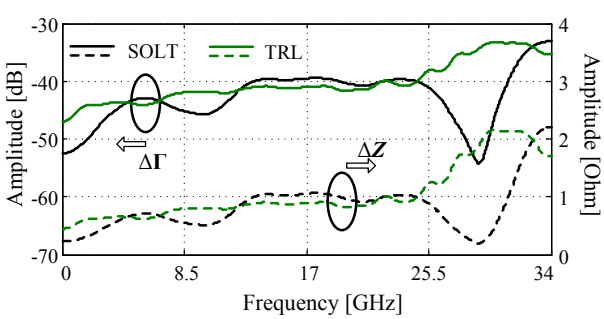

Fig. 9. The magnitude of the estimates $\Delta\Gamma_L$ (solid lines) and ΔZ_L (dash lines) of L30 and L75.

Typically, VNA random noise errors are between -80 dB and -60 dB in the frequency range of these experiments. Therefore, their impact on $\Delta\Gamma_L$ and ΔZ_L estimates is negligible. The contact repeatability error is less than -50 dB and less than -40 dB for coaxial connectors and for wafer probes, respectively. We attributed observed uncertainties in estimates to the contact repeatability errors.

V. Conclusion

This article presented a new method of verification of the characteristic impedance of transmission lines. The method uses the time domain processing of the measured line reflection coefficient and therefore provides fast and accurate results in a wide frequency range. The proposed method can be successfully applied for verification of the test calibration sets vs. references and for various designs of transmission lines (e.g. coaxial and planar).

Additionally, accurate VNA calibration is not required for quantitative (comparative) analysis of the test transmission lines. Therefore, implementation of the proposed method is simple and easy in conventional engineering laboratory environment.

Acknowledgement

The work was supported by Russian President Grant No. MK-3107.2015.8. Authors also acknowledge Dr. Uwe Arz from PTB (Germany) for his great support with the measurement data of the RM8130.

References

[1] D. F. Williams, R. B. Marks, and A. Devidson, "Comparison of on-wafer calibration," *38th ARFTG Conf. Dig.*, pp. 68-81, Dec. 1991.

[2] A. A. Savin, V. G. Guba, A. Rumiantsev, and B. D. Maxson, "Estimation of Complex Residual Errors of Calibrated Two-Port Vector Network Analyzer," *83rd ARFTG Microwave Measurement Conference*, 2014, Tampa, Florida, USA, pp. 1-4.

[3] "Reference Material 8130. Coplanar waveguide calibration set," NIST, Gaithersburg, MD 20899, USA, 1998.

[4] G. Wübbeler, C. Elster, T. Reichel, and R. Judaschke, "Determination of the Complex Residual Error Parameters of a Calibrated One-Port Vector Network Analyzer," *IEEE Trans. on Instrumentation and Measurement*, vol. 58, no. 9. September 2009, pp. 3238-3244.

[5] A. A. Savin, "A Novel Factor Verification Technique for One-Port Vector Network Analyzer," *Proceedings of the 43rd European Microwave Conference*, 7-10 Oct 2013, Nuremberg, Germany, pp. 60-63.

[6] A. A. Savin, V. G. Guba, and O. N. Bykova, "Comparison Analysis of VNA Residual Errors Estimation Algorithms with Time Domain Separation," *86th ARFTG Microwave Measurement Conference*, 2015, Atlanta, Georgia, USA, pp. 1-4.

[7] R. B. Marks, "A multi-line method of network analyzer calibration," *IEEE Trans. Microwave Theory Tech.*, vol. 39, no. 7, pp. 1205-1215, Jan. 1991.

Uncertainty of Parameter Estimation in Equivalent Circuit Model of Gallium Nitride Diode for Rectifier Design at 5.8 GHz

Ryoko Kishikawa[1, 2], Masahiro Horibe[1], Shigeo Kawasaki[2, 3]

[1]Research Institute for Physical Measurement, National Institute of Advanced Industrial Science and Technology (AIST),

[2]School of Physical Science, The graduate University for Advanced Studies,

[3]Institute of Space and Astronautical Science (ISAS), Japan Aerospace Exploration Agency (JAXA)

***Abstract* — This paper reports our precise measurement of a gallium nitride (GaN) schottky diode and our diode model for designing a rectifier at 5.8 GHz. The originality in this study is the estimation of the measurement uncertainty of the GaN diode and its propagation to the diode model, and the calculation of the uncertainty of the parameters in this model. The relative expanded uncertainty (95 % confidence level) of the measured impedance is 61 % for the real part and 17 % for the imaginary part. Applying a circuit with a resistor and a capacitor in parallel as the diode model, the expanded uncertainties of the resistor and capacitor are approximately 70 % and 17 %, respectively. This result implies that the sensitivity coefficients of the resistor are larger than those of the capacitor.**

***Index Terms* — Measurement, calibration techniques, measurement uncertainty, equivalent circuit modeling, GaN schottky diode.**

I. Introduction

These days, applications using gallium nitride (GaN) based on the stable crystal growth method are drawing significant attention [1]-[3]. GaN is a semiconductor with a wide band gap; hence, its resistivity to cosmic rays is considered excellent. We have developed a wireless power transmission and a wireless communication system for space use, based on the hybrid semiconductor integrated circuit (HySIC) technology. HySIC is an integrated circuit that utilizes silicon (Si) and compound semiconductors such as GaN and gallium arsenide (GaAs). Circuit miniaturization and energy saving can enable the successful utilization of this technique. The GaN diode is the core device for the rectifier in our power transmission system. Thus, a precise measurement and the uncertainty estimation of a GaN schottky diode, followed by the construction of a diode model based on the results at 5.8 GHz, are reported in this paper.

A rectifier converts the RF input signal into a DC signal. The nonlinear characteristics of the diode enable the conversion. The basic process for developing a rectifier involves four steps: the measurement of the diode, the construction of the diode model using the measurement result, design of a matching circuit, and fabrication based on the simulation data. Currently, rectifiers are being designed considering the harmonic wave matching and the best RF to DC conversion efficiency is over 80 % at 5.8 GHz [4].

However, measurement uncertainty is an issue. Thus, a diode model that is developed based on measurements always includes an uncertainty. This affects the precision of the rectifier design. The characteristics simulated using the best estimated measurement values are not necessary realized: the realized characteristics are within the sum of the measurement and fabrication uncertainties.

The originality of our study is that we introduce an uncertainty analysis technique for diode measurements and rectifier designs. We will effectively develop a high-efficiency rectifier using this technique.

Section II summarizes our measurement of a GaN diode at 5.8 GHz. In section III, we analyze a diode model and calculate its uncertainty based on the measurement results. The last section will conclude the paper.

II. Measurement of GaN Diode

We measured the reflection coefficients of GaN diodes using a vector network analyzer (VNA) at 5.8 GHz. Because our in-house GaN diode could not be connected directly to a coaxial connector, we fabricated a new measurement jig (Figs. 1 and 2). Coplanar lines with characteristic impedances of 50 Ω each were etched on a printed circuit board. The GaN diodes were mounted with bonding wires at one end of the lines and end-launch connectors were mounted on the other end. Next to the diode lines, open, short, and load lines were fabricated. These three lines are used for calibrating the effects of the end-launch connectors and coplanar lines.

Fig. 3 shows our measurement configuration. The measurement instrument was a VNA. The port power was -17 dBm. A bias T and a DC power supply were used for applying the bias voltage. The calibration for the VNA was performed at the reference plane of the cable shown in Fig. 3.

The measurement at the calibration plane was calibrated using the thru-reflect-line (TRL) method and the measured reflection coefficient was defined as Γc [5]. It was performed with respect to the national metrology standard of impedance in Japan [6]. Hence, the reliability is traceable to the SI unit. The effect from the calibration plane to the ends of the lines was corrected using the open-short-load (OSL) method. The reflection coefficient at the ends of the lines, Γ', was obtained using the two calibration methods.

978-1-5090-4514-3/16/$31.00 ©2016 IEEE

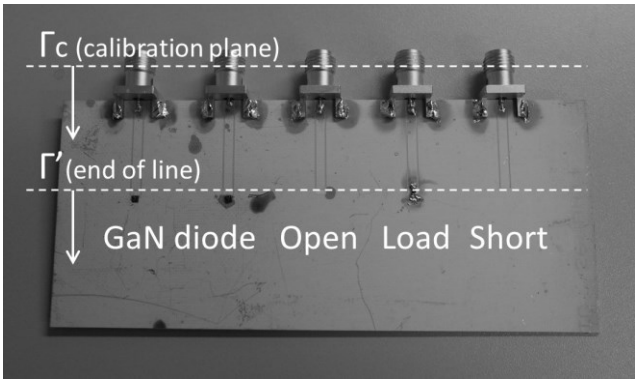

Fig. 1. Photograph of the GaN diode, calibration devices (open / short / load), and measurement jigs.

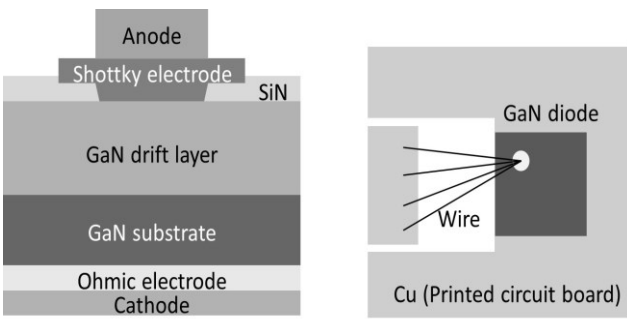

Fig. 2. Cross section drawing of the in-house GaN diode (left) and schematic drawing of the GaN diode measurement jig (right).

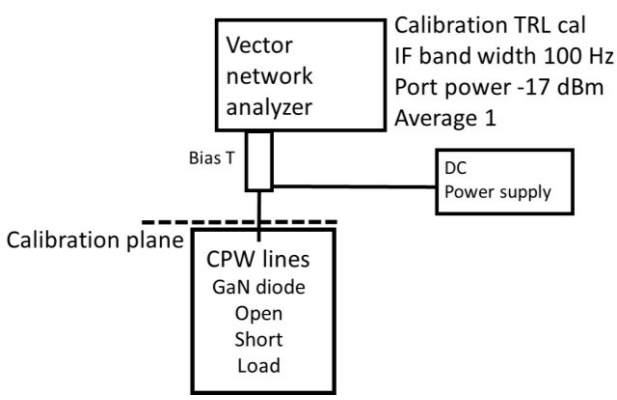

Fig. 3. Measurement configuration

We estimated the uncertainty of the reflection coefficient measurement. The analysis included three steps. The first step was the estimation of the uncertainty of Γc at 5.8 GHz. This measurement has already been developed in Japan using the national metrology standard [6]. The uncertainty budget is shown in Table I.

Table I

The uncertainty budget for measurement of reflection coefficient at the end-launce connector reference plane, Γc, at 5.8 GHz.

Uncertainty contribution	Standard uncertainty of |Γc|
Residual directivity	0.001345
Residual matching	0.000328
Residual tracking	0.0000746
Effective load match	0.00000000000000236
Linearity of receiver	0.000385
Resolution	0.000000289
Noise	0.000160
Cable flexure	0.001082
Repeatability	0.002754
Combined standard uncertainty (68 % confidence level)	0.003294
Expanded uncertainty (95 % confidence level)	0.0066

Table II

The standard uncertainty (68 % confidence level) caused from the technique of fabricating circuits at 5.8 GHz.

Uncertainty contribution	Magnitude of reflection coefficient	Phase of reflection coefficient
End-launch connector	0.0025	1.6 °
Resistor	0.0079	13 °
OSL connection repeatability	0.00030	0.0045 °
Wire bonding	0.00084	0.052 °

Next, the uncertainty of Γ' was calculated. In addition to the uncertainty in Table I, the techniques for mounting the end-launch connectors, etching the coplanar lines, and the measurement repeatability of the OSL lines also contribute to the uncertainty. They were estimated by fabricating or measuring them repeatedly and calculating their uncertainty distributions. The result is summarized in Table II.

The final step was the correction of the bonding wire effect from the coplanar line to the diode and the calculation of the uncertainty of the reflection coefficient of the GaN diode, Γ. We fabricated a coplanar line with the same wire structure as that of the diode line without the diode and characterized the loss and phase shift of the electromagnetic waves caused by the bonding wires. By subtracting the two effects from Γ', the best estimated value of Γ was obtained. The uncertainty of Γ was analyzed by fabricating the wire lines several times and calculating the uncertainty distribution. Table II shows the uncertainty result at 5.8 GHz.

The best estimated reflection coefficient, Γ, without a bias voltage supply was -0.90-*j*0.36 at 5.8 GHz. By performing a Monte Carlo simulation, the conversion from the reflection coefficient, Γ, to the impedance was accomplished. The best

estimated impedance of the GaN diode was 0.79-*j*9.64 Ω at 5.8 GHz. The expanded uncertainties (95 % confidence level) were 0.48 Ω for the real part of the impedance and 1.64 Ω for the imaginary part of the impedance. The relative expanded uncertainties were 61 % for the real part and 17 % for the imaginary part. The distribution is shown in Fig. 4.

III. GaN Diode Model

A. The Best Estimated Parameters

We analyzed a diode model using the impedance measurement results shown in Fig. 4. In this study, we applied the data to a circuit with a resistor, R, and a capacitor, C, in parallel (Fig 5). The resistor, R, is a parameter that represents the nonlinear characteristics of the diode. The electric current that flows generally depends upon the voltage, V, and is proportional to exp(qV/NkT)-1. Here, q, N, k, and T indicate the elementary charge, the ideality factor, the Boltzmann constant, and the temperature, respectively. The capacitor, C, is a parameter that shows the depletion layer capacity. It is also dependent on the voltage, V, in general and is proportional to $(1-V/V_j)^{-m}$. V_j and m indicate the built-in potential and a constant, respectively. Analysis at a zero-volt bias only is performed in this report.

The impedance, Z, of the diode circuit model shown in Fig. 5 can be described as:

$$Z = \frac{R}{1+\omega^2 R^2 C^2} - j\frac{\omega R^2 C}{1+\omega^2 R^2 C^2}. \quad (1)$$

Here ω indicates the angular frequency. From the equation, R and C are derived using the following equations:

$$R = \frac{|Z|^2}{\mathrm{Re}\,Z} \quad (2)$$

$$C = -\frac{1}{\omega}\frac{\mathrm{Im}\,Z}{|Z|^2}. \quad (3)$$

From eqs. (2) and (3), and the impedance results in section II, R and C are equal to 118 Ω and 2.83 pF, respectively, at 5.8 GHz without a bias voltage.

B. Uncertainty of Parameters

We estimated the uncertainties of R and C that are propagated from the impedance measurement and the uncertainty reported in section II. If we assume that ReZ and ImZ are independent, the uncertainty propagation from Z to R and C is calculated as follows:

$$u(X) = \sqrt{\left(\frac{\partial X}{\partial \mathrm{Re}\,Z}\right)^2 u(\mathrm{Re}\,Z)^2 + \left(\frac{\partial X}{\partial \mathrm{Im}\,Z}\right)^2 u(\mathrm{Im}\,Z)^2}. \quad (4)$$

Here, X=R or C. u(R), u(C), u(ReZ), and u(ImZ) are the standard uncertainties (68 % confidence level) of R, C, ReZ, and ImZ, respectively.

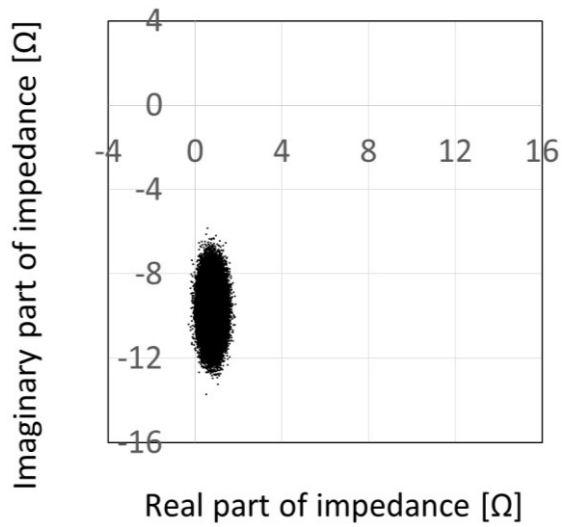

Fig. 4. The impedance distribution for the GaN diode at 5.8 GHz. Each dot indicates the result of the Monte Carlo trials.

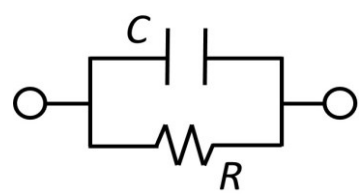

Fig. 5. Circuit diagram of the diode model.

Based on eq. (4) and the impedance measurement results in section II, the expanded uncertainty (95 % confidence level) of R and C are 82 Ω and 0.47 pF, respectively. The relative uncertainties of R and C are approximately 70 % and 17 %, respectively. The relative uncertainty of R is worse than that of C because the sensitivity coefficients of R are larger than those of C.

IV. Conclusion

In this paper, we have presented our study on precise measurements for GaN diodes, the diode model, and the analysis of the uncertainty at 5.8 GHz. The originality in this study is the determination of the parameters in the diode model with the uncertainty propagated from the GaN diode measurement data. In the model with the resistor, R, and capacitor, C, in parallel, the expanded uncertainties (95 % confidence level) were approximately 70 % and 17 %, respectively. This result implies that we have to determine R more carefully from the measurement results.

In future studies, we propose to construct a perfect nonlinear diode model with an uncertainty estimation using GaN diode

measurements with a bias voltage supply. We intend to assess the efficiency of the model considering the uncertainty. Additionally, the design of a rectifier based on the diode model will be performed. The simulated RF to DC conversion efficiency and its uncertainty that is propagated from the measurement using the diode model will be obtained.

ACKNOWLEDGEMENT

This work is supported by Japan Space Systems (JSS), Ministry of Economy, Trade and Industry (METI). We would like to thank Dr. Miyachi from JAXA, Dr. Kaho from NTT, Prof. Nishikawa and Prof. Yoshida from Kagoshima University, Mr. Anma from Mitsubishi Heavy Industries., and Mr. Okada and Mr. Ueno from Sumitomo Electric Industries, Ltd.

REFERENCES

[1] H. Amano, N. Sawaki, I. Akasaki, and Y. Toyoda, "Metalorganic vapor phase epitaxial growth of a high quality GaN film using an AIN buffer layer," Appl. Phys. Lett., vol. 48, no. 353, 1986.

[2] H. Amano, I. Akasaki, T. Kozawa, and K. Hiramatsu, "Electron beam effects on blue luminescence of zinc-doped GaN," J. Lumin., vol. 40-41, pp. 121-122, 1988.

[3] R. Quary, "Gallium Nitride Electronics," Springer series in materials science, 2008.

[4] Y. H. Sug and K. Chang, "A novel dual frequency rectenna for high efficiency wireless power transmission at 2.45 and 5.8 GHz," Microwave Symposium dig., vol.2, 00.1297-1300, 2002.

[5] R. Kishikawa, M. Horibe, A. Miyachi, M. Matsunoshita, and S. Kawasaki, "Uncertainty Estimation for Gallium Nitride Diode Model based on VNA Measurement at 5.8 GHz," Conf. on Precision Electromagnetic Measurements dig., 2016. 02.

[6] BIPM, Calibration and Measurement Capabilities, http://kcdb.bipm.org/appendixc/country_list_search.asp?CountSelected=JP&type=EM

Linearity Characterization of RF Circuits through an Unequally Spaced Multi-Tone Signal

Sylvain Laurent*, Jean Pierre Teyssier ‡, Raymond Quéré* Jacques Sombrin† and Michel Prigent *
*Xlim
Université de Limoges, 16 rue Jules Valles, 19100 Brive, France
Email: sylvain.laurent@xlim.fr, raymond.quere@xlim.fr, michel.prigent@xlim.fr
†Xlim
Université de Limoges
123 Avenue Albert Thomas, 87000 Limoges, France
Email: jacques.sombrin@unilim.fr
‡Keysight
Santa Rosa, USA
Email: jean-pierre_teyssier@keysight.com

***Abstract*—An Unequally Spaced Multi-Tone signal (USMT) is used for the assessment of nonlinear devices and circuits. The statistical properties of the signal are described. The setup measurements for such a signal are given either by using a Large Signal Network Analyzer (LSNA) or a Nonlinear Vector Network Analyzer (Keysight PNA NVNA with SA option). A USMT Load Pull (USMT-LP)set-up has been developed using a LSNA and it is shown how to extend this set-up to a NVNA receiver. The set-up is fully on-wafer calibrated at all the frequencies of interest. The USMT-LP set-up is configured to make measurements with USMT signals up to eight frequencies and allows measuring simultaneously the MT output power, gain, Power Added Efficiency (PAE), Carrier to Intermodulation (C/I) ratio or Noise Power Ratio (NPR) in order to derive the Error Vector Magnitude (EVM) induced by the device.**

***Index Terms*—Unequally Spaced Multi-Tone signals, Device Linearity, NVNA, LSNA, Load Pull, NPR, EVM**

I. Introduction

Linearity is a key requirement for the design of any telecommunications systems. This performance criterion is directly related to the Bit Error Rate (BER) of a communication chain and must be assessed not only for the global system but also for the different components taking part of the system. Power Amplifiers (PA) are the main nonlinear part of the link and their linearity performances must be known at the design stage. A number of criteria have been used for a long time such as Noise Power Ratio (NPR) or Error Vector Magnitude (EVM) for the in band noise or Adjacent Channel Power Ratio (ACPR) for the out of band noise. The formal equivalence between the two criteria have been demonstrated in [1] under certain assumptions while the EVM remains a universally accepted measure of the quality of the communication link. This equivalence has been used to determine the NPR of a PA using EVM measurements [2]. Specialized test signals based on multisine signals have been proposed in [3] and [4] that allow to separate the frequencies at the intermodulation products from the signal frequencies. Moreover in [6] a multitone Load Pull set up based on a LSNA has been proposed and used in [7] to assess the linearity of GaN technology. In this work a more indepth description of the signal used is proposed as well as the implementation of the method using an NVNA. Some comparisons between sampler based and mixer based acquisition methods will be given.

II. USMT signal properties and generation

A. Signal properties

As already mentioned, the method proposed relies on the generation of a test signal specifically taylored to allow the separation of the intermodulation noise from the signal of interest. Here the input theoretical signal is constituted of Unequally Spaced Multi Tones (USMT) i.e a number (eight here) of sines which frequencies are determined analytically from 1

$$f_k = f_1 + (k-1)\cdot \Delta f + \epsilon_k \; 1 \leq k \leq n \tag{1}$$

Where, $f_1 = l \cdot f_\epsilon$ is the lowest frequency, k is the rank of the frequency, $\Delta f = m \cdot f_\epsilon$ is the frequency spacing between the tones and $\epsilon_k = p_k \cdot f_\epsilon$ is the frequency shift of the kth frequency respectively to the position of the equally spaced frequency. In order to accurately measure the response of the device at the input frequencies and at IM frequencies, all the input frequencies are chosen on a frequency grid, which resolution is f_ϵ . Where l , k, m, p_k are integers. The total number of points in the grid is chosen in order to cover the period $T_\epsilon = \frac{1}{f_\epsilon}$ exactly. Therefore the Digital Fourier Transform DFT behaves as a bank of N filters of the type $\dfrac{\sin(\pi N x)}{\sin(\pi x)}$ where $x = (\frac{f}{N f_\epsilon} - \frac{k}{N})_{k=0..N-1}$. The frame duration is T_ϵ and the frequency bandwidth is $BW = N \cdot f_\epsilon$. This signal is generated by an Arbitrary Waveform Generator (AWG) to feed the Device under Test (DUT). Here 8 frequencies are chosen to generate the signal and the shifting vector $p = [0, 1, 3^{i_1}, 3^{i_2}, 3^{i_3}, 3^{i_4}, 3^{i_5}, 3^{i_6}]$ guarantees that all the IM3 products are distinct from the input frequencies and from

978-1-5090-4514-3/16/$31.00 ©2016 IEEE

each other. The integers i_1, i_2, i_3, i_4, i_5, i_6 can be chosen in order to cover different spacings between frequencies in order to excite the various low frequency time constants of the device parasitics. A possible signal is shown in Fig. 1. It exhibits eight input frequencies and intermodulation products frequencies. It must be noted that using the set of frequencies given in Fig. 1 the calculation of the position of all the IM3 and IM5 frequencies gives exactly 2472 different frequencies, all of them being distinct. Table-1 gives all the intermodulation products generated by the nonlinearity orders 3 and 5 respectively. Note that it can be proved that only the frequencies of type $n_i.f_i + n_j.f_j + ... + n_m.f_m$ where $n_i + n_j + ... + n_m = 1$ will serve compute intermodulation product in the IF band. Particularly the products of type $2f_i - f_j$ are exactly 6dB below the $f_i + f_j - f_k$ type.

order	# of frequencies involved	frequency combination	# of IM products
3	2	$2f_i - f_j$	56
3	3	$f_i + f_j - f_k$	168
5	2	$3f_i - 2f_j$	56
5	3	$3f_i - f_j - f_k$	168
5	3	$2f_i + f_j - 2f_k$	336
5	4	$f_i + f_j + f_k - 2f_l$	280
5	4	$2f_i + f_j - f_k - f_l$	840
5	5	$f_i + f_j + f_k - f_l - f_m$	560

TABLE I
INTERMODULATION PRODUCTS

The signal has been to feed of a memoryless nonlinearity which reads $f(x) = 4 \cdot \left(\frac{1}{1+\exp(-x)} - 0.5 \right)$. The probability density function (PDF) of the $I(t)$ and $Q(t)$ components of the envelope is plotted in Fig.2 and is Gaussian. Those statistics do not depend on the phases of the different tones, therefore only one frame measurement is required to characterize the device, thus reducing the measurement time to T_ϵ. The Peak to Average Power Ratio (PAPR) of the input signal is 8.4 dB.

B. Signal generation

The USMT signal is generated using a Keysight MXG-N5182B waveform generator. The set of N IQ data is determined through the determination of the MXG RF frequency f_G which value is chosen as an integer multiple of the base frequency f_ϵ, so the complex USMT reads

$$\hat{x}(t) = e^{j2\pi f_G t} \cdot \sum_{k=1}^{K} (I_k + jQ_k) e^{j2\pi(f_k - f_G)t} \qquad (2)$$

where f_k are the frequencies of the test frequency set. However, as the IQ modulator of the generator is not perfect, the output signal of the MXG consists of the test signal and parasitics signals which are due to the local oscillator leak and the image frequencies of the frequency set. Those signals have been found to be 50dB below the test signal. While

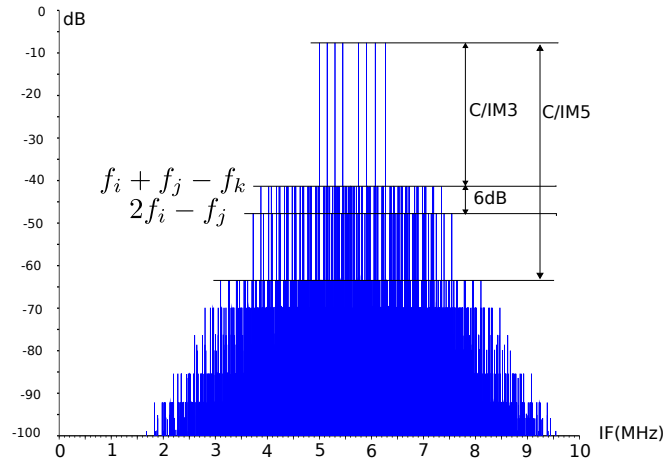

Fig. 1. Spectrum of the output signal obtained for the shifting vector $p = [0, 1, 3, 9, 27, 81, 243, 729]$ and $f_\epsilon = 100\,Hz$ and $B = 21$

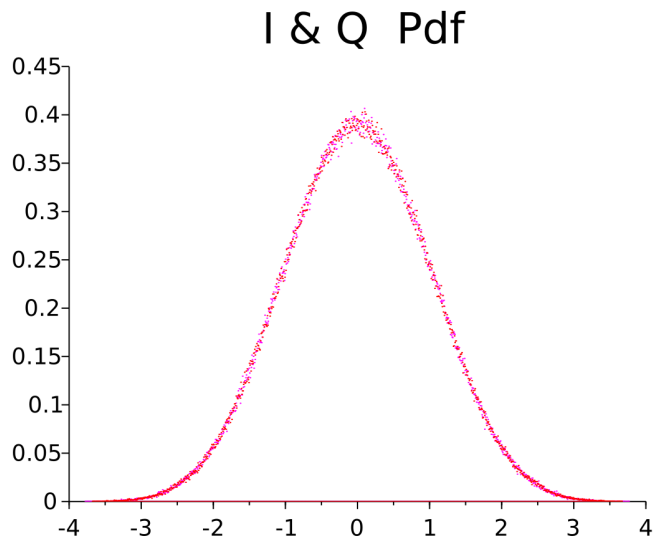

Fig. 2. Normalized characteristics of the signal obtained for the shifting vector $p = [0, 1, 3, 9, 27, 81, 243, 729]$ and $f_\epsilon = 100\,Hz$ and $B = 21$ PDF of the I and Q signals

their impact on the nonlinear behavior of the device can be neglected, still they can produce some unwanted noise at the measurement end. In order to eliminate this undesired noise, the MXG RF frequency f_G is chosen in such a way that the image frequencies $f_{im_k} = 2f_G - f_k$ fall in the zeros of the DFT filter bank. It is still possible to improve the test signal quality with predistorsion at the IQ dats side.

III. UNEQUALLY SPACED MULTI-TONE LOAD-PULL SET-UP DESCRIPTION

A. Sampler based receiver

The description of the USMT-LP using a LSNA has been given in [6] and some comments on the structure of the frequency interleaving are given here. In the case of a sampler based receiver, the frequencies located around the harmonics

at frequencies $2f_0$, $3f_0, \cdots$ are converted in the IF band, so the choice of the LO frequency must be carefully adjusted in order to not interfere with the frequencies of interest. Indeed the signal of interest at the output of the device is constituted of clusters of frequencies located around DC, fundamental of the RF and the harmonics. In order to separate the useful frequencies from the unwanted ones, the local oscillator frequency as well as the MXG RF frequency have to be carefully selected. At first the image frequencies of the generator can be cancelled by choosing the RF frequency f_G different of the local oscillator frequency in order to shift the Intermediate Frequency $f_{im_k} - f_{OL}$. In the same way the local oscillator frequency f_{OL} has to be selected so that the frequencies falling in the IF band of the measurement filter are distinct from the wanted tones. If f_{im} is the set of the inband intermodulation frequencies and f_i , f_j are the input frequencies, the following conditions have to be ensured.

- $f_{im} - f_{OL} \neq f_i - f_j \; \forall i, j$ for the LF set of frequencies
- $f_{im} - f_{OL} \neq f_i + f_j 2f_{OL} \; \forall i, j$ for the harmonic 2 set
- $f_{im} - f_{OL} \neq f_i + f_j + f_k - 3f_{OL} \; \forall i, j, k$ for the harmonic 3 set

In the mixer based receiver those conditions are by far much less severe as the power of the OL at harmonic frequencies is much lower and the f_{OL} of the Keysight PNA is automatically chosen to ensure the above conditions.

B. Mixer based receiver

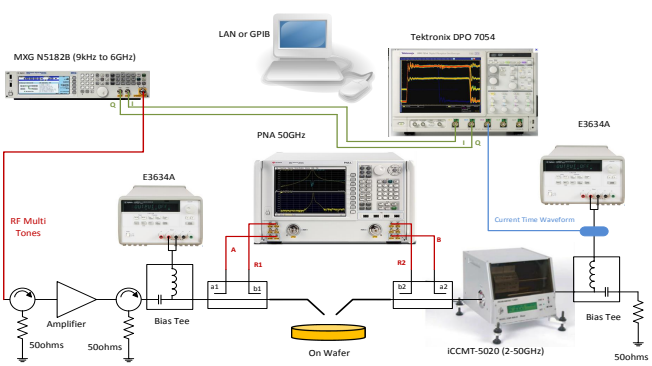

Fig. 3. Setup for time domain load-pull on-wafer characterization.

The description of the complete measurement setup is given in Fig.3. Note that this kind of measurement configuration can handle high power on-wafer measurements [5]. It consists in an Arbitrary Waveform Generator (AWG - Keysight MXG-N5182B), an oscilloscope (Tektronix DPO7054), a tuner (Focus iCCMT-5020) and a VNA (PNA 50GHz with SA option). The AWG generates the digital baseband waveforms and a direct in-phase/quadrature (I/Q waves) with 160 MHz bandwith. The frequency range is 9 KHz to 6 GHz. A digital sampling scope Tektronix DPO 7054 (500 MHz bandwidth, 20 GS/s, 8 bit) is used to measure the I/Q waves and the LF drain bias current with a large bandwidth current sensor (120 MHz 5 A AC/DC Current Probe). The load impedance is fixed using

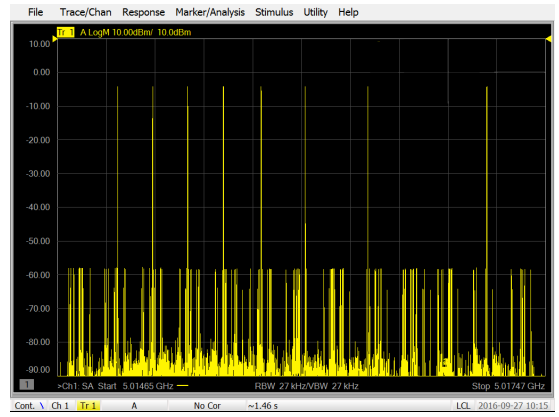

Fig. 4. USMT signal generated by MXG which is measured with PNA, the input power on each frequencies is equal to -4dBm

a iCCMT-5020 tuner. In this paper, the optimization is not performed because the measurement test will be realized on an amplifier. The PNA is a mixer-based network analyzer which has a typical dynamic range close to 90dB in this application (Fig. 4). The IF bandwidth is approximately 38MHz.

This specific NVNA is used because of its capability to acquire the modulated signals in a single measurement record. Moreover, the acquisition time is very fast.

All the instruments are controlled using the open source software (Scilab). The cut-off frequency of the DC bias tee used is close to 10MHz. Thus, it ensures the measurement of all parasitic effects up to this frequency range.

In the next section, the amplifier measurement results obtained using a power calibration are explained.

IV. Bench validation

This section shows the connectorized amplifier measurement. The amplifier is AML 26P2401, RF bandwidth 2GHz to 6GHz. The gain is 24 dB and the output power at 1 dB compression is 23 dBm. The measured bias current is approximately 190mA under 15V. For the RF measurements, the power calibration consists in taking into account the access paths losses of the device under test. The load impedance is 50 ohms. The measurement process performs power sweep between -34dBm to -20dBm with 1 dB step for each tones. The input signal is obtained for shifting vector p= [0, 1, 3, 9, 27, 81, 243, 729] and the frequency resolution (f_ϵ) is equal to 1kHz with 100000 points.

Fig. 5 shows a spectrum results obtained for 2 input powers level at input and output access of the amplifier. On the extremities of measurement band, the image reject are present.

For linearity measurement, in band Carrier to order Inter Modulation ratio (C/IM), is measured according to the following expression: $C/IM\,(dB) = 10 \cdot \log\left(\frac{P_u}{P_{IM}}\right)$. P_u is the total fundamental power and P_{IM} is the total third-order and fifth-order inter modulation power at frequencies between the first and last fundamental frequencies . In addition, the Error

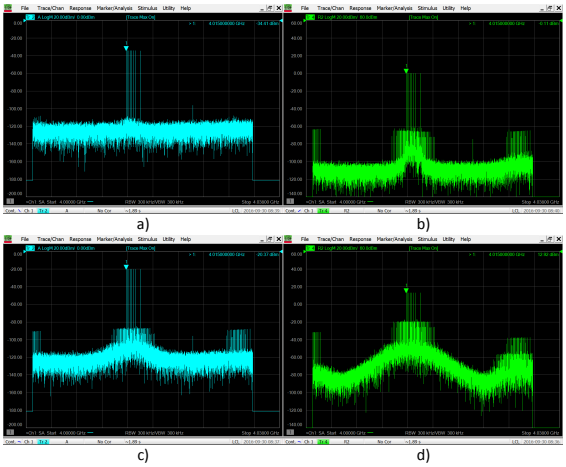

Fig. 5. a) is amplifier input signal at -34dBm on each tones generated by MXG and b) is the result of a) after the amplifier. c) is the amplifier input signal at -20dBm on each tones and d) is the amplifier output signal

Fig. 6. Linearity measurements for AML26P2401 amplifier

Vector Magnitude (EVM) [1], is defined as $20 \cdot \log(EVM) = 40 - C/IM$.

These two criterias obtained both at the input and output are shown in Fig. 6

Fig. 7 shows the output power and gain versus input power. To calculate the output power, the sum of each tones divided by the number of tones is used. The input power is also calculated in the same way.

V. Conclusion

An USMT-LP system has been developed to characterize microwave power amplifiers. This fully calibrated setup allows measuring all the power characteristics as well as time domain waveforms under modulated signals in a couple of seconds, thus providing the designers with an invaluable tool to assess the linearity performances of the devices as well as to verify the nonlinear models which take into account the low frequency parasitics of the device.

Matching the USMT advanced test signal design and the measurement equipment brings to optimized DUT measurements in terms of speed and dynamical range.

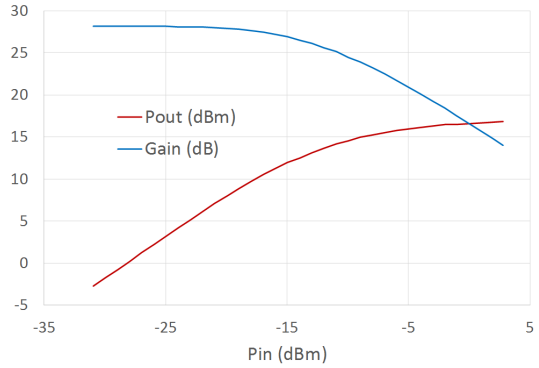

Fig. 7. Output power and gain versus input power for AML26P2401 amplifier

Acknowledgment

This work has been partially support by the French ANR under grant "DEFIS-RF", Chair "Systèmes Intégrés et sécurisés" of the LABEX ΣLIM and the Keysight Technologies University Research Grant #5775.

References

[1] J. Sombrin, *"On the formal identity of EVM and NPR measurement methods: Conditions for identity of error vector magnitude and noise power ratio,"* Microwave Conference (EuMC), 2011 41st European , vol., no., pp.337,340, 10-13 Oct. 2011

[2] P. Medrel & Al. *"Time domain envelope characterization of power amplifiers for linear and high efficiency design solutions,"* Wireless and Microwave Technology Conference (WAMICON), 2013 IEEE 14th Annual , vol., no., pp.1,6, 7-9 April 2013

[3] S. Farsi & Al., *"Characterization of Intermodulation and Memory Effects Using Offset Multisine Excitation,"* Microwave Theory and Techniques, IEEE Trans. on , vol.62, no.3, pp.645,657, March 2014

[4] J.P. Teyssier & Al., *A test set-up for the analysis of multi-tone intermodulation in microwave devices*, Microwave Measurement Conference (ARFTG), 84th ARFTG, dec 2014

[5] F. De Groote & Al., *"High power on-wafer capabilities of a time domain load-pull setup"*, Proc. IEEE MTT-S Int. Microwave Symp. Digest 2008

[6] S. Laurent, K. Kahil, R. Quéré, J. Sombrin, *"A Multi-Tone Load Pull Measurement System for On-Wafer Characterization of Microwave Power Transistors"*, 46th European Microwave Conference (EuMC), London October 4-6 2016

[7] S. Kahil, S. Laurent, R. Quéré, J. Sombrin, D. Floriot, V. Brunel, C. Teyssandier, *"Linearity Characterization of GaN HEMT Technologies Through Innovative Multi-Tone Load-Pull Measurements,"* 11th European Microwave Integrated circuits Conference (EuMIC), London October 3-4 2016